Rapid Solidification of an Aluminum-Lithium Alloy for Solid Freeform Fabrication Applications

David W. Heard

Department of Mining and Materials Engineering

McGill University, Montreal, QC

March 2013

A thesis submitted to McGill University in partial fulfillment of the requirements of the degree of Doctorate of Philosophy.

Abstract

The solidification behavior of an Aluminum-Lithium-Copper (Al-Li-Cu) alloy, AA2199, and the microstructural morphology and solute distributions resulting from three rapid solidification processing techniques were investigated. Controlled-Short-Circuiting Metal-Inert-Gas (CSC-MIG) welding, Laser Re-melting (LRM), and Electrospark Deposition (ESD) were investigated. The microstructural morphology of the rapidly solidified material was then compared with the Kurz-Giovanola-Trivedi (KGT) model for microstructural development during rapid solidification, to allow for the estimation of the solidification front velocity (SFV) realized during processing. This SFV was then compared with that required for non-equilibrium solute partitioning as predicted by the Continuous Growth Model (CGM) of Aziz. The solute distributions where then measured and compared with that expected for equilibrium and non-equilibrium partitioning, to determine if the solute trapping phenomenon had been induced during solidification.

The CSC-MIG deposited material displayed a fine (4.3 ±1 μm) cellular structure, comparable to that previously reported for electron beam welding. The SFV was estimated to be ~2-4.5x10^{-4}m/s, a value below that required to impart any deviation from equilibrium partitioning, as predicted by the CGM. Chemical analysis via Energy Dispersive Spectroscopy (EDS) and Time-Of-Flight Secondary-Ion-Mass-Spectroscopy (TOF-SIMS) revealed lateral segregation of copper to the cell walls, and a similar segregation profile to that predicted by the Clyne-Kurz model. TOF-SIMS also revealed a homogeneous lateral lithium distribution, however depth profiling displayed some extent of lithium enrichment at the surface of the deposited material.

Within the LRM material it was determined that laser pulse energies on the order of 0.25 – 0.5 Joules resulted in a fine cellular solidification structure. It was then estimated that SFV values between 3 and 25cm/s were realized during solidification. Furthermore, a pulse energy of 0.125J resulted in featureless solidification structure, indicative of a planar liquid-solid interface being formed during solidification. The SFV for the samples produced with a pulse energy of 0.125J was estimated to be >1m/s. The CGM for solute

trapping predicted a deviation from equilibrium partitioning during solidification for all pulse energy levels employed. This was supported by the chemical profiling of lithium within the re-melted samples measured via X-ray photoelectron spectroscopy (XPS). Measurement of the lattice parameter via X-ray diffraction (XRD) revealed that the solute trapping phenomenon resulted in the formation of a super saturated solid solution, as evident through a reduction of the lattice parameter from 4.0485 Å for the starting material to 4.0399 Å in the material re-melted with a pulse energy of 0.125 Joules.

The analysis of the ESD solidified material revealed the breakdown of a planar solid-liquid interface into a cellular morphology, resulting in the presence of fine copper rich cells within the microstructure (~30-60nm in width). The KGT model predicted this occurred at a SFV of ~1m/s. The CGM predicted significant trapping of lithium at a SFV of 1m/s, which was supported by the TOF-SIMS data, which revealed a homogeneous distribution of lithium within the solidified material. Finally Atom-Probe-Tomography revealed the presence of the Al_3Li phase upon the copper rich cell walls. It was then determined that the Al_3Li was not formed during the solidification process, as predicted by a time dependent nucleation model for phase suppression during rapid solidification, and therefore is believed to be the result of subsequent aging.

Subsequent aging of the rapidly solidified material revealed that the CSC-MIG deposited material did not respond to aging, while the ESD and LRM deposited material did. The ESD deposited material displayed a small amount of lithium burn-out, and therefore the T1 hardness suffered slightly. The T5 hardness of the ESD material however obtained a hardness of ~99HV, which is significantly less than the ~150HV of the T8' Base-Metal (BM). It was determined that this was due to the lack of a cold-working process prior to aging. It was also revealed that the T1 hardness of the LRM material is similar to that of the T3 BM. It was therefore concluded that the LRM process is capable of producing SFF components of AA2199, which can achieve adequate hardness via a natural aging process, without requiring cold-working prior to aging. Finally the LRM solidified material in the T5 condition was determined to be capable of aging to 81% of the hardness (~122HV) of the BM in the T8' condition, without the application of a cold working process prior to aging.

Résumé

Le comportement de solidification d'un alliage aluminium-lithium (Al-Li), AA2199, et la morphologie microstructurale des distributions de soluté de trois techniques rapides de traitement de solidification ont été étudiés. Contrôle de court-circuit métallique de gaz inerte (CSC-MIG), Re-fondrement au Laser (LRM), et dépôt d'électro-érosion (ESD), ont été étudiés. La morphologie microstructurale du matériel solidifié rapidement a ensuite été comparée au modèle Kurz-Giovanola-Trivedi (KGT) qui décrit le développement microstructurale lors de la solidification rapide afin de permettre l'estimation de la vitesse du front de solidification (SFV) apparaissant au cours du traitement. Cet SFV a ensuite été comparé à celui des partitions de soluté non-équilibrés prédit par le modèle de croissance continue d'Aziz. Les distributions de soluté ont ensuite été mesurées et comparées à celles prédites pour l'éffet de partage à l'équilibre et hors d'équilibre afin de déterminer si le phénomène de piégeage de soluté a été incité au cours du solidification.

Le matériel déposé par CSC-MIG affiche une structure cellulaire très fine(4,3 ± 1 micron) et comparable à celle rapportée antérieurement pour le soudage par faisceau d'électrons. L'estimation de l'SFD est d'environ 2-4.5x10-4m / s. Ceci est inférieure à celle requise pour causer une déviation de partition à l'équilibre comme prévu par le CGM. L'analyse chimique par EDS et TOF-SIMS a révélé une ségrégation latérale de cuivre sur les parois cellulaires et un profil de ségrégation semblable à celui prédit par le modèle Clyne-Kurz. Time-Of-Flight-secondary-Ion Mass Spectroscopy-(TOF-SIMS) a révélé une distribution latérale homogène de lithium. Cependant, le profile en profondeur affiche une certaine quantité d'enrichissement de lithium à la surface du matériel déposé.

Au sein du matériel LRM, il a été déterminé que les énergies de pulsation au laser à l'ordre de 0,125 à 0,5 Joules causent une structure cellulaire de solidification fine. Il a ensuite été estimé que des vitesses de front de solidification (SFV) entre 3 et 25 cm / s ont été atteints au cours de la solidification. Le CGM pour le piégeage des solutés a prédit une déviation des partitions à l'équilibre lors de la solidification pour tous niveaux d'énergie de pulsation employés. Ce phénomène a été appuyé par le profile chimique de lithium dans les échantillons refondus et mesurés à l'aide du spectroscopie de photoélectrons au rayons X (XPS). Les mesures du paramètre du réseau crystalline par diffraction de rayons X (XRD) ont révélé que le phénomène de piégeage de soluté donne lieu à la formation d'une solution saturée super-solide, ce qui est démontré par une réduction du paramètre du réseau de 4,0485 Å pour le matériel de départ comparé à 4,0399 Å pour le matériel refondu avec une énergie de pulsation de 0,125 joule.

L'analyse de la matière solidifiée par ESD a révélé la désintégration de l'interface planaire solide-liquide en une morphologie cellulaire qui entraîne la présence de cellules fines riches en cuivre à l'intérieure de la microstructure (~ 30-60nm de largeur). Le modèle déduit par KGT prédit que ceci se produit à un SFV d'environ 1m / s. Le CGM prédit une piégeage significatif de lithium à une SFV de 1 m / s, ce qui a été soutenu par les données TOF-SIMS qui ont révélé une distribution homogène de lithium dans le matériel solidifié. Ensuite, la tomographie par sonde d'atoms a révélé la présence de la phase Al3Li sur les parois des cellules riches en cuivre. De plus, il a été déterminé que le Al3Li n'a pas été formé lors de la solidification. Ceci est prédit par un modèle temporel de nucléation qui sert à la prédiction de la suppression de phases au cours de la solidification rapide, et donc le résultat est un processus de vieillissement antérieur.

Table of Contents

List of Figures

Acknowledgments

I would like to thank my fiancé Kristen, for her incredible support over the years. Also to my parents, who have always been there to encourage me and offer their support. A big thanks to my brother, Bryan, who was always available when I needed him. I would also like to thank all the members of the Novel Advances in Nanomaterials Lab (NAIN Lab), past and present, including; Jason, Dave W., David L., Cory, Pat, Dom, Nesli, Marie-Pier, Rabab, Bamidele, Gil, Sam, Beto, Phil, Ramona, and especially Rosen (my AA2199 partner), for everything they have done to help me along the way. I would like to thank my friends Nate, Pantcho, Musti, Cecilé, Kristian for all of the great times we shared. I would also like to acknowledge Manas, for all of the helpful solidification discussions during this project. To Dong-Guen and Deniz, thanks for putting up with me in our office. I would also like to acknowledge the assistance of the wonderful technical and administrative staff within the Materials Engineering department at McGill University including; Barbara, Terry, Monique, Ray, Robert, and Helen.

I would also like to thank Alcoa for the technical support and raw material supplied throughout this project, most specifically Dr. Julien Boselli and Dr. Roberto Rioja. I extend my gratitude to the Natural Science and Engineering Research Council (NSERC) PGS-D award, the McGill Engineering Doctoral Award (MEDA), Rio-Tinto Alcan scholarship, and the Regroupement Aluminum Research Centre (REGAL) for the financial assistance.

To the Blades of Wood (hockey team) and Balls of Steel (softball team), thank you for all the great times on the ice and the field.

Finally I am indebted to my supervisor, Prof. Mathieu Brochu, who was always available to encourage me, keep me on track, and help me with anything that I needed, be it scientific, career, or even (sometimes unsolicited) fashion advice. I promise I will never wear white socks outside of the gym again. I hope to be able to continue exchanging ideas with you in the future.

Preface & Contribution of Authors

As the first author on the four manuscripts included within this thesis, I produced all of the samples, performed the analysis, and wrote the manuscripts.

The Atom-Probe-Tomography experiments were performed at the University of Michigan by Prof. Emmanuel Marquis and Christian Banner. Prof. Marquis is an author on the manuscript included in Chapter 6

Prof. Raynald Gauvin supplied technical expertise as well as assistance with some of the scanning electron microscopy analysis.

Dr. Julien Boselli and Dr. Roberto Rioja of Alcoa provided the AA2199 material used throughout this study, and supplied technical expertise throughout the project.

Prof. Mathieu Brochu supervised the entire project as well as supplied technical and scientific advice throughout.

1 Introduction

1.1 Aluminum-Lithium Alloys

Aluminum-Lithium (Al-Li) alloys have been long studied for use within aerospace and aeronautical applications, due to their high-strength and low density. Lithium is the lightest known metallic element (density = 0.534g/cc), and the only metal (other than beryllium, which poses serious health risks during processing) that when alloyed with aluminum, increases the elastic modulus of the resulting alloy (see Figure 1-1), while reducing the density (see Figure 1-2) [1]. When alloying aluminum with lithium, the density is reduced by ~3% while the Young's Modulus is increased by approximately 6%, for each weight percent of lithium added [2].

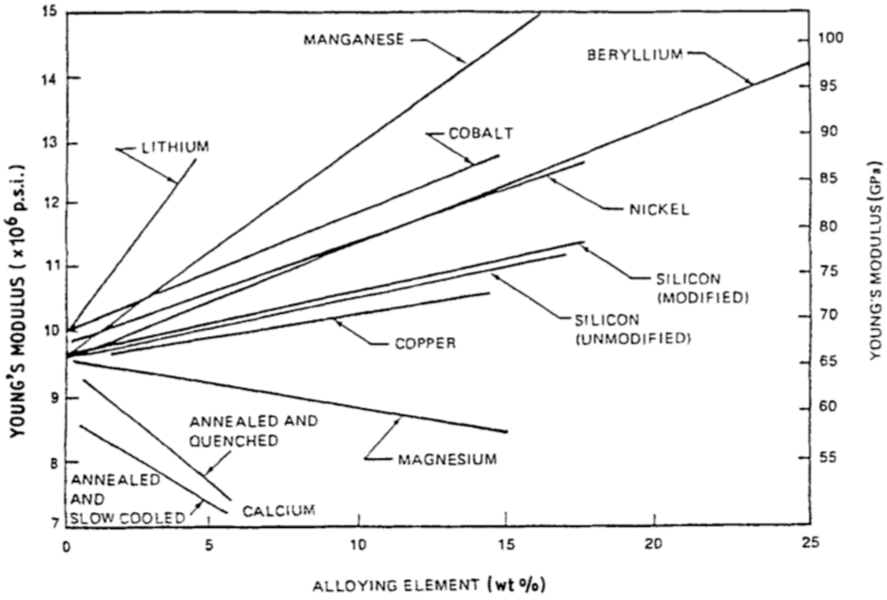

Figure 1-1 - Influence of various alloying additions on the Young's Modulus of aluminum [2].

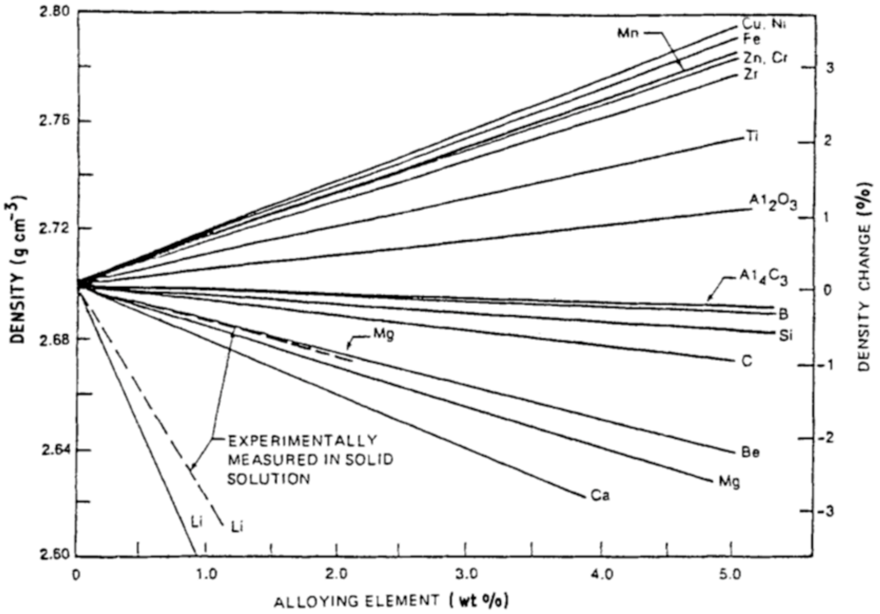

Figure 1-2 - Influence of various alloying additions on the density of aluminum [2].

Research in the field of Al-Li alloys began with an intensive investigation of binary, ternary, and quaternary lithium alloys performed by Assman in 1926 [3]. However, due to the limited understanding of the thermo-mechanical processing (TMP) routes that are ultimately required to produce Al-Li alloys with desirable properties, Assman concluded that the lithium bearing alloys offered no major benefit. This work did, however inspire other research, ultimately resulting in the first patent regarding Al-Li alloys being granted to Czochralski and Welter in 1927 [4, 5]. A summary of the key Al-Li alloys developed and their respective compositions is shown in Table 1-1 [6].

The first 2XXX series Al-Li alloy, X2020 (Al-1.1Li-4.5Cu-0.5Mn-0.2Cd), was developed by Alcoa in 1958, based on the research and resulting patent of an Al-Cu-Li-X alloy granted to Le Baron in 1945 [7, 8]. The X2020 alloy displayed high stiffness and resilience to compression, and was developed for use within the RA-5C Vigilante aircraft. Although the alloy also displayed low ductility and fracture toughness with respect to other high-strength aluminum alloys, and was ultimately withdrawn from service in 1974,

Table 1-1 - Key Al-Li alloys developed to date [6].

	Li	Cu	Mg	Ag	Zr	Sc	Mn	Zn	Approximate Date
1st Generation									
2020	1.2	4.5					0.5		Alcoa 1958
01420	2.1		5.2		0.11				Soviet 1965
01421	2.1		5.2		0.11	0.17			Soviet 1965
2nd Generation (Li ≥ 2pct)									
2090	2.1	2.7			0.11				Alcoa 1985
2091	2.0	2.0	1.3		0.11				Pechiney 1985
8090	2.4	1.2	0.8		0.11	0.17			EAA 1984
01430	1.7	1.6	2.7		0.11				Soviet 1980's
01440	2.4	1.5	0.8		0.11				Soviet 1980's
01450	2.1	2.9			0.11				Soviet 1980's
01460	2.25	2.9			0.11	0.09			Soviet 1980's
3rd Generation (Li<2 pct)									
2195	1.0	4.0	0.4	0.4	0.11				LM/Reynolds 1992
2196	1.75	2.9	0.5	0.4	0.11		0.35max	0.35max	LM/Reynolds 2000
2297	1.4	2.0	0.25max		0.11		0.3	0.5max	LM/Reynolds 1997
2397	1.4	2.8	0.25max		0.11		0.3	0.10	Alcoa 1993
2198	1.0	3.2	0.5	0.4	0.11		0.5max	0.35max	Reynolds/McCook 2005
2099	1.8	2.7	0.3		0.09		0.3	0.7	Alcoa 2003
2199	1.6	2.6	0.2		0.09		0.3	0.6	Alcoa 2005
2050	1.0	3.6	0.4	0.4	0.11		0.35	0.25max	Pechiney 2004
2060	0.75	3.95	0.85	0.25	0.11		0.3	0.4	Alcoa 2011
2055	1.15	3.7	0.4	0.4	0.11		0.3	0.5	Alcoa 2012

it served as a starting point for new ternary and quaternary alloy development. This increase in interest in the development of Al-Li alloys, coupled with the gas crisis of 1973, resulted in the formation of an international conference series dedicated to the study Al-Li alloys and fabrication techniques [9-12].

The 1980's brought about the second generation Al-Li alloys. These alloys featured a higher lithium content (>2 weight percent) and a reduced copper content (<3 weight percent). The main focus when developing these alloys was a reduction of density to allow for direct alloy replacement of current aerospace standard materials such as 7075-T6 and 2024-T3 [6]. While the 2nd generation alloys offered the advantages of a lower density, higher Young's modulus, and lower fatigue crack growth rates, the alloys also displayed lower short-transverse fracture toughness, lower plane stress fracture toughness, and an increased anisotropy of tensile properties with respect to the traditional aerospace materials [6].

The third generation alloys entered the market in the 1990's and offered a reduced lithium content (<2 weight percent) in response to the shortcomings of the 2nd generation alloys [6]. The 3rd generation Al-Li alloys included the AA2199 alloy, the alloy investigated throughout this study.

AA2199 is a new (3rd) generation Aluminum-Lithium-Copper alloy developed by Alcoa in 2005 [13]. The nominal composition of the alloy is displayed in Table 1-2. AA2199 was developed to be competitive with composite materials used within the aerospace industry. Lithium strengthens the alloy through the formation of the δ′ (Al_3Li) coherent precipitate. Copper additions promote the formation of the θ′-type (Al_2Cu), T_1(Al_2CuLi), and T_2(Al_6CuLi_3) strengthening precipitates. Magnesium is included as it is believed that magnesium may substitute for the lithium within the T_1 phase to form S' (Al_2CuMg) which also strengthens the alloy [14]. Manganese is added to induce the formation of incoherent dispersoids ($Al_{20}Cu_2Mn_3$), which help homogenize slip within the lattice, resulting in increased damage tolerance and toughness. Zirconium is added to break up intergranular precipitates and ultimately inhibit the recrystallization process, resulting in a finer and more homogenous microstructure during TMP, through the formation of the coherent β′ (Al_3Zr) dispersoid. Finally zinc is added to improve the corrosion resistance of the alloy, and is most likely present within solid solution, however recent studies have shown that Zn may be incorporated in the precipitate formation [15]. A schematic representation of the precipitates formed within the AA2199 system is shown in Figure 1-3.

Table 1-2 - Composition of Al-Li alloy 2199

Alloy	Cu	Li	Zn	Mg	Mn	Zr	Fe	Si	Al
(wt%)	2.3-2.9	1.4-1.8	0.2-0.9	0.05-0.4	0.1-0.5	0.05-0.12	0.07 max	0.05 max	Bal.

(at%)	1.0-1.2	5.3-6.8	0.1-0.4	0.05-0.4	0.1-0.5	0.1-0.4	0.03max	0.05 max	Bal.

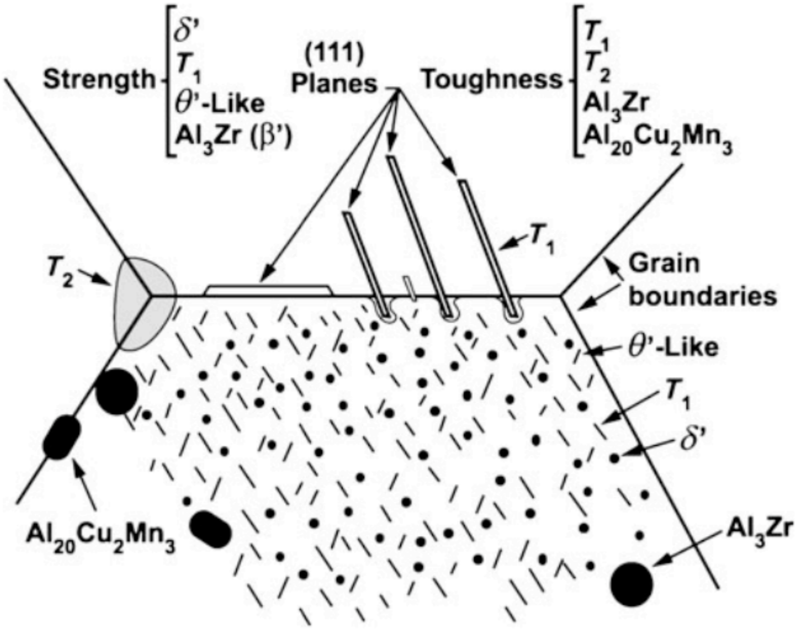

Figure 1-3- Schematic representation of the precipitates present within the AA2199 alloy [13].

TMP of Al-Li alloys has been shown to be of great importance, as both texture, and dislocation density play important roles in the mechanical behavior of the alloy. The introduction of a deformation process prior to aging (such as rolling or stretching) increases the dislocation density and promotes the nucleation of precipitates away from grain boundaries [16]. Also, an increase in dislocation density due to cold-working has been shown to result in an increase in the concentration of the strengthening T_1 (Al_2CuLi) precipitate [16]. Furthermore, Al-Li alloys have a tendency to form strong textures, which are known to significantly affect their mechanical behavior [17]. It has been shown that a high Brass [(110)/<112>] texture results in high levels of anisotropy within Al-Li alloys [18]. It is therefore important to control the texture through proper alloying processing. A schematic representation of the typical Al-Li alloy processing route, designed to minimize the Brass texture is shown in Figure 1-4.

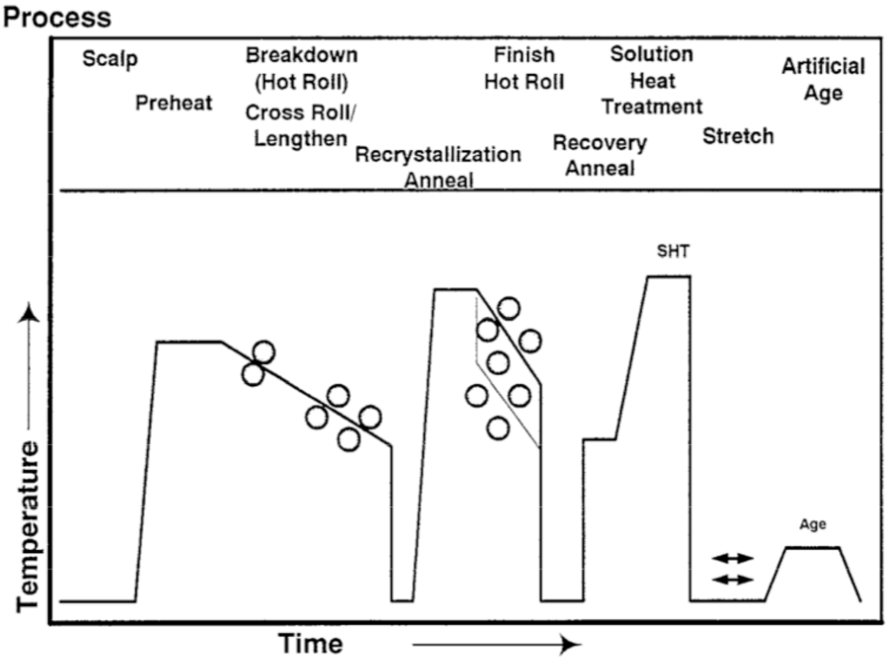

Figure 1-4- A typical processing flow sheet for Al-Li alloys [18].

Aside from issues of anisotropy related to texture developments during processing, Al-Li alloys also face other challenges such as lithium segregation and depletion, due to the high reactivity and diffusivity of the lithium atoms within the alloys.

One concern associated with Al-Li alloys is oxidation at high temperatures [19]. It has been determined that near-surface lithium is depleted during oxidation at high temperature due to a selective oxidation process. Papazian *et al.* showed that during oxidation of Al-Li alloy 8090 (~2.58 wt.% Li) in dry air at 500ºC, the lithium diffusion out of the sample occurred at a rate equivalent to what would be expected in a sample with a near zero surface concentration of lithium [19]. Therefore, the limiting factor concerning the lithium depletion was that of lithium diffusivity through the alloy to the surface. As the diffusivity of lithium within aluminum is high ($2.5x10^{-9}$ cm^2/s [20, 21]), this creates a significant issue. The authors also determined that while lithium depletion was decreased when the samples were heated within an argon atmosphere the lithium diffusion out of the sample still occurred at a rate to be expected with a surface lithium concentration of approximately one percent. Therefore, it was determined that in an argon atmosphere, the rate of lithium loss is governed by surface conditions (such as gas purity).

Espoto *et al.* [22] later studied the segregation of lithium in a single crystal Al-Li alloy containing approximately 6.5 at.% (~1.76wt.%) lithium, during annealing under high-vacuum. The authors reported that rapid segregation of lithium to the first atomic layer at temperatures greater than 500 K occurred. The authors determined that lithium diffusion was not the rate-limiting step, although it is believed that the diffusivity of lithium determined within this study may be erroneous due to the formation of a diffusion barrier during surface cleaning of the samples with ion bombardment. Regardless, it was still concluded that lithium rapidly segregated to the surface and was depleted during high temperature processing under high vacuum.

Furthermore, the high reactivity of lithium has also been known to result in the formation of detrimental hydrides or oxides, as well as the burn-out (or depletion) of lithium during solidification [23].

Another major difficulty concerning the study of Al-Li alloys, is the challenges associated with the detection of lithium in common microanalysis techniques [19]. Low atomic number elements, such as lithium suffer from a low fluorescence yield of ~0.005, therefore few X-rays are generated from within the sample, resulting in difficulties achieving the detector counts required to perform quantitative analysis [24]. Lithium distribution studies have previously been performed using (n,α)-radiography [23, 25], however these techniques require complex equipment, are difficult to perform, and contain low spatial resolution. Auger electron spectroscopy (AES) has been used to determine lithium distribution, such as the work previously mentioned by Esposto *et al.*, however AES is a surface phenomenon and therefore not a reliable tool for mapping the lithium distribution within the bulk of a sample. While Electron Energy Loss Spectroscopy (EELS) process offers an alternative method to study the lithium distribution, there are concerns regarding the associated with the preparation of aluminum-lithium transmission electron microscopy (TEM) foils [26].

One can then infer, from the high lithium diffusivity and reactivity, that it is therefore paramount to ensure a high-quality shielding atmosphere, and operate under conditions of minimum heat-input to minimize lithium depletion during lithium processing at elevated temperatures and during lithium solidification.

1.2 Solidification

Solidification describes the transformation of matter from a liquid phase to a solid phase. This process may occur within pure materials, or mixtures of substances such as alloys. When a crystal is formed within an alloy, a local change in composition occurs [27]. This local change in composition then results in local changes in the physical properties of the melt, and the crystal-melt (solid-liquid) interface, such as the equilibrium melting temperature. Therefore as a solid grows within a liquid, composition gradients are developed. When these compositional gradients are formed on the microstructural scale, this phenomenon is referred to as microsegregation.

1.2.1 Segregation and solute profiles

The phases present and the distribution of solute throughout the microstructure of a component after solidification can be predicted through the analysis of the corresponding equilibrium phase diagram. Figure 1-5 displays a hypothetical phase diagram. The phase diagram can used to predict the equilibrium concentration of solute within the solid (C_s) and liquid (C_L) at any given temperature (T). The ratio of the concentration of solute in the solid to that in the liquid is known as the equilibrium partition coefficient (*k*) (see Equation 1).

$$k = \frac{C_s}{C_L} \qquad \text{(Equation 1)}$$

As an alloy of composition C_0 is cooled from the melting temperature (T_m) to a temperature below the liquidus temperature (T_L), a solid phase will begin to nucleate. The initial composition of this solid phase, according to the equilibrium phase diagram, will be $C_{s0}=kC_0$. As the temperature of the system is further decreased, and solidification progresses, the composition of solid and liquid will be dictated by the solidus and liquidus lines, respectively. It is then possible to calculate the composition of the solid formed during equilibrium solidification through the application of the lever rule formula (see Equation 2).

$$C_s' = \frac{kC_0}{f_s(k-1)+1} \qquad \text{(Equation 2)}$$

Where f_s is the solid fraction of the alloy at a given temperature. The solid fraction can then be calculated as a function of temperature using Equation 3.

$$f_s = \left(\frac{1}{1-k}\right)\left(\frac{T_L - T}{T_m - T}\right) \qquad \text{(Equation 3)}$$

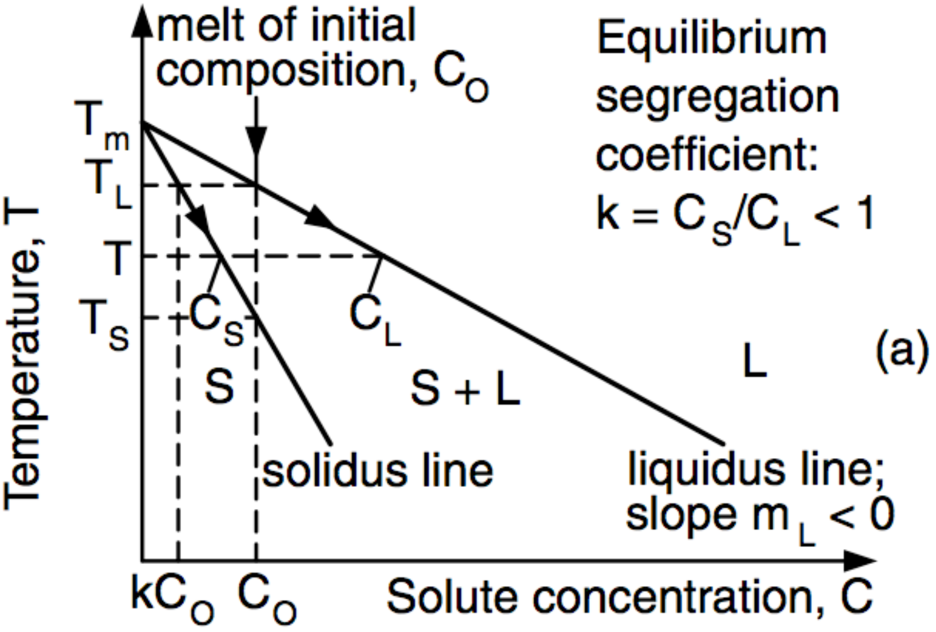

Figure 1-5- A portion of a hypothetical binary phase diagram [28].

It can be seen from the lever rule formula, that the solid formed throughout the solidification process does not contain a constant concentration of solute. In fact the last solid to form will contain the highest solute concentration. However, during equilibrium solidification, the long time durations involved promote complete diffusion of the solute within both the solid and liquid phases. This diffusion is significant enough to produce a final homogeneous solute distribution throughout the solidified material with an average composition equal to C_0 [29].

However, enormous periods of time and extremely low growth rates are necessary to allow for solidification to proceed under equilibrium conditions ensuring complete diffusion of the solute within the solid phase [30, 31]. As industrial solidification processes tend to occur at higher growth rates than what are required to induce equilibrium solidification, it is more practical to discuss solidification in which there is limited, or negligible diffusion in the solid (or back diffusion). When solidification progresses without diffusion in the solid, there is no opportunity for the non-uniform distribution of solute, as dictated by the equilibrium partitioning of elements, to homogenize, and therefore results in microsegregation. This segregation may occur on the microscopic (dendrite arms) or macroscopic (entire components) scale. In 1913, Gulliver, and then 20 years later, Scheil, independently developed a model to describe solute partitioning during solidification where no diffusion of the solute within the solid occurs. The Gulliver-Scheil model therefore estimates the concentration of solute within the solid and liquid phases as a function of solid fraction or temperature (see Equations 4 and 5).

$$C_L = C_0(f_L)^{(k-1)} \qquad \text{(Equation 4)}$$

$$C_s = kC_0(1 - f_s)^{(k-1)} \qquad \text{(Equation 5)}$$

As the lever-rule calculations may not reflect true actual solidification processes due to the assumption of equilibrium conditions and therefore a high extent of solute diffusion within the solid, the Gulliver-Scheil model, which assumes no back diffusion of solute from the solid phase, may also not accurately reflect reality. In actuality, many solidification processes will tend to fall between these two bookend equations, in a realm where some extent of back-diffusion is occurring. To assess this Brody and Flemings [32] modified the Gulliver-Scheil model, as shown in Equations 6 and 7, to account for some extent of back diffusion in the solid by including an alpha (α) term which is dependent upon the solute diffusivity in the solid D_s, the solidification time (t_f), and the diffusion path length (L) (or appropriate dendrite arm spacing (λ=2L).

$$C_s = kC_0[1-(1-2\alpha k)f_s]^{(k-1)/(1-2\alpha k)} \quad \text{(Equation 6)}$$

$$\alpha = \frac{D_s t_f}{L^2} = \frac{4D_s t_f}{\lambda^2} \quad \text{(Equation 7)}$$

While the Brody-Flemings model has been applied with success, Flemings et al. have shown that the solute is in fact not conserved during the analysis [33]. An example of how this unbalance of solute creates problems is shown in Figure 1-6, in which the relationship between fraction solid and temperature is displayed for a 0.62%C steel sample as calculated using the Gulliver-Scheil model, lever rule, and the Brody-Flemings (with various α-values)[30].

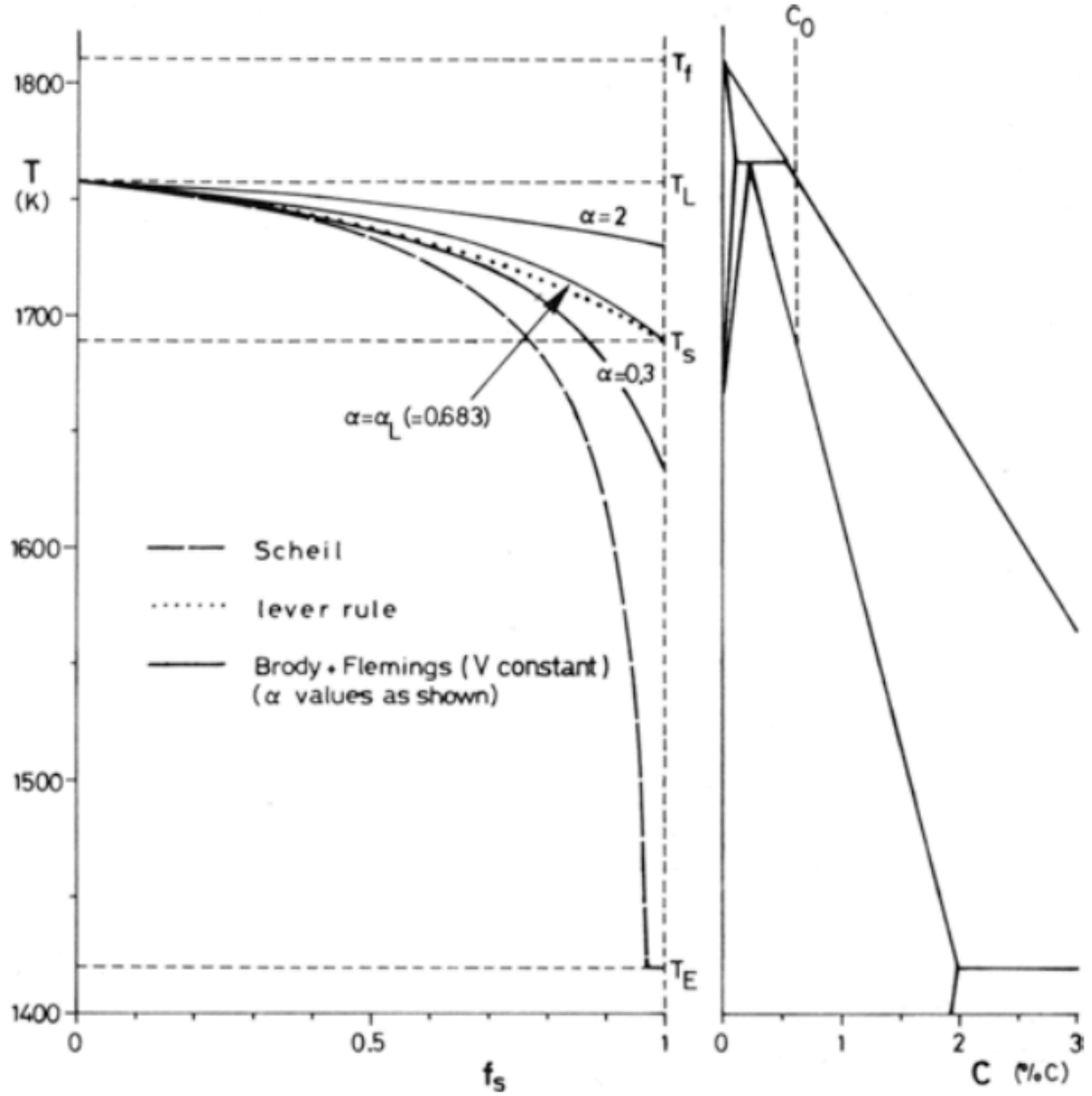

Figure 1-6- Theoretical fraction solid vs. temperature curves for 0.62%C steel as calculated using the Gulliver-Scheil model, Lever rule, and the Brody-Flemings model [30].

It can be seen that the Brody-Flemings model produces incorrect results at some values of α. The plot shows that with a α value of 2, the Brody-Flemings model predicts solidification to complete at a temperature greater than the solidus temperature of the alloy. To correct for this, Clyne and Kurz modified the Brody-Flemings model to prevent this overestimation through the inclusion of the Ω function, a mathematical spline between the correct boundary conditions [30]. The resulting Clyne-Kurz model is shown in Equations 8 and 9.

$$C_s = kC_0[1 - (1 - 2\Omega k)f_s]^{(k-1)/(1-2\Omega k)} \qquad \text{(Equation 8)}$$

$$\Omega = \alpha\left[1 - \exp\left(-\frac{1}{\alpha}\right)\right] - \frac{1}{2}\exp\left(-\frac{1}{2\alpha}\right) \qquad \text{(Equation 9)}$$

The resulting model is capable of accurately depicting the solute profiles, while remaining between the two classical limiting cases of Lever Rule and Scheil cooling, as shown in Figure 1-7 [30]. Furthermore, while the previous discussion focused on binary mixtures, these solidification theories can be extended to ternary systems with slight adjustments.

While the progression of a solidification front may result in the formation of compositional gradients within the solid, the morphology of the solid-liquid front itself may change as the solidification conditions change, resulting in a further complication of the solute profile.

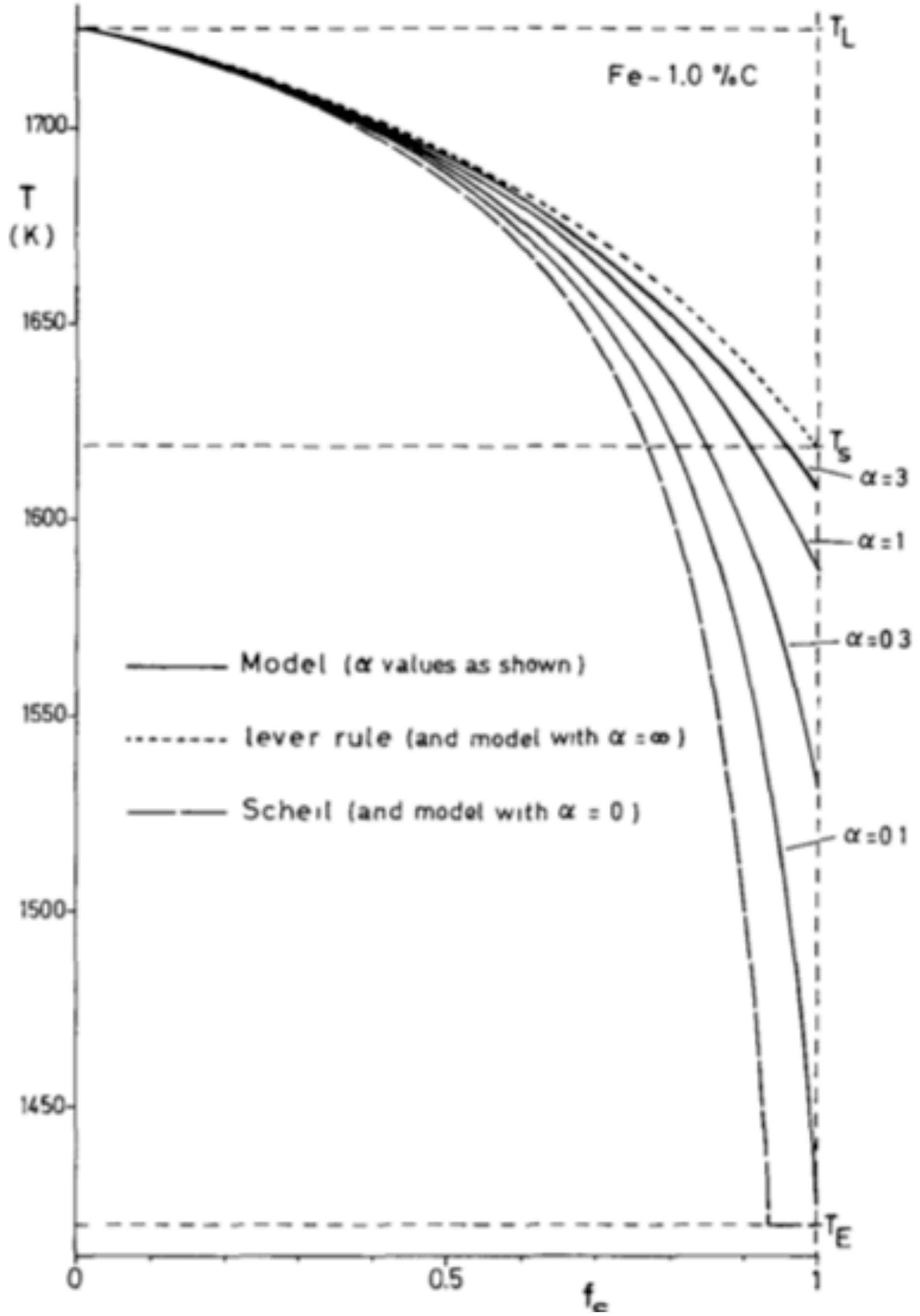

Figure 1-7- The application of the Clyne-Kurz model to predict the solute profile of a Fe-1.0pctC alloy, displaying the proper behavior falling between the limiting cases of Lever Rule and Scheil Cooling [30].

1.2.2 Morphological development and interface stability

The morphology of a solid-liquid interface, and therefore the resulting alloy microstructure, will vary according to the solidification conditions such as growth rate (R), and the thermal gradient (G) experienced, as well as the physical properties of the melt such as freezing range of the alloy (ΔT_f) and diffusivity of solute species (D_L). A simple theory proposed by Rutter and Chalmers known as constitutional supercooling theory (CST) was developed to describe the stability of the liquid/solid interface, or ultimately the morphology of the interface as a function of G and R. The theory states that a planar interface shall remain stable if,

$$\frac{G}{R} \geq \frac{\Delta T}{D_L} \qquad \text{(Equation 10)}$$

A further decrease in G/R, or an increase in the constitutional supercooling, would result in an unstable liquid/solid interface. This interface instability then manifests in the formation of a cellular morphology. Further decreasing G/R, or increasing the constitutional supercooling would then result in the formation of a dendritic and ultimately an equiaxed dendritic morphology.

This relationship between G, R, and microstructural morphology is displayed in Figure 1-8. The figure depicts how the G/R ratio controls both the morphology of the solidification structure, as well as the size of the structure [28]. It can be seen that a high temperature gradient and a low growth rate, such as that found in many crystal drawing or zone refining processes, will result in the stabilization of a planar interface. A high growth rate and a low thermal gradient results in an equiaxed dendritic morphology. This is the result of the liquid being cooled below the equilibrium melting temperature, and is known as supercooling. As the extent of supercooling is increased, the energy barrier for the nucleation of a solid phase is reduced, therefore resulting in a more heterogeneous nucleation event, and ultimately a change in morphology. Furthermore, while the G/R ratio controls the solidification morphology, G X R controls the size or scale of the structure formed.

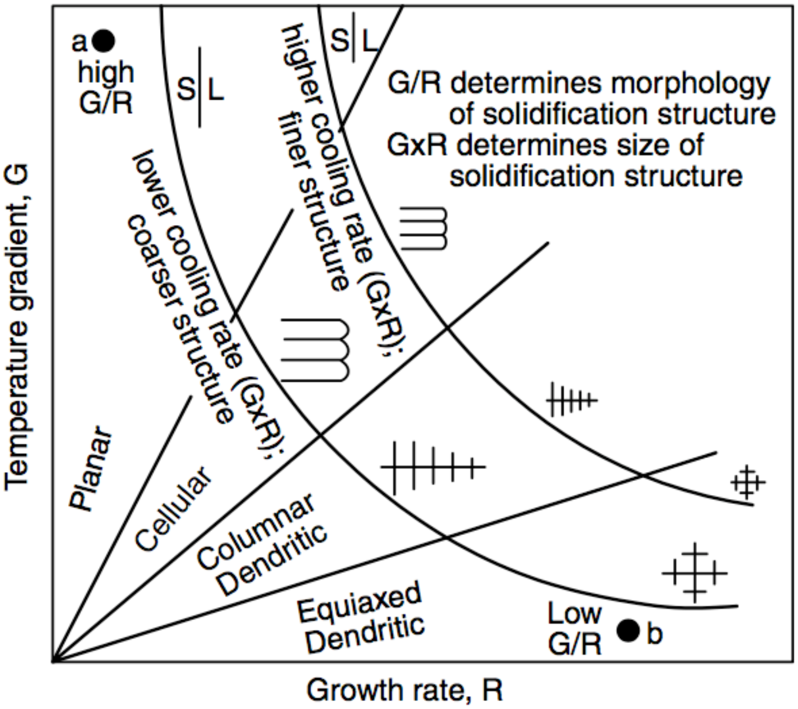

Figure 1-8- An example of a solidification map displaying the relationship between R, G, and morphology [28].

Therefore for a given G/R ratio, an increase and G and R will result in a refinement in the solidification structure. This can been noted by the refinement of microstructures produced by rapid solidification.

1.2.3 Rapid Solidification

While the CST has been used to accurately describe the solidification of many systems, the theory neglects the stabilization of a liquid-solid interface at high growth velocities, or solidification front velocities (SFV) due to surface tension effects. To address this concern Mullins and Sekerka developed another model for interface stability during solidification [34]. This new model was then used to describe rapid solidification processes by Coriell and Sekerka [35]. Another limitation of the application of CST to rapid solidification with high SFV values is the assumption of equilibrium partitioning during solidification.

Having the two main issues with CST addressed; the stabilization of an interface at high velocities by Mullins and Sekerka, and the non-equilibrium partitioning of solute by Aziz, Kurz, Giovanola, and Trivedi (KGT) then developed a model to describe the microstructural evolution of a sample during rapid solidification [36].

The KGT model allows one to numerically calculate the relationship between the Péclet number and the SFV using Equations 11-15:

$$V^2A + VB + C = 0 \qquad \text{(Equation 11)}$$

$$A = \frac{\pi^2\Gamma}{P^2D^2} \qquad \text{(Equation 12)}$$

$$B = \frac{mC_0(1-k)\xi_c}{D[1-(1-k)\mathrm{Iv}(P)]} \qquad \text{(Equation 13)}$$

$$C = G \qquad \text{(Equation 14)}$$

Where V is the SFV, Γ is the Gibbs-Thompson coefficient, m is the slope of the liquidus line of the phase-diagram, P is the Péclet number, k is the partition coefficient, D is the liquid interdiffusion coefficient, Iv(P) is the Ivanstov's solution, G is the mean temperature gradient at the interface, and:

$$\xi_c = 1 - \frac{2k}{\left[1+\left(\frac{2}{P}\right)^2\right] - 1 + 2k} \qquad \text{(Equation 15)}$$

The dendrite tip radius as a function of SFV can then be calculated through the application of Equation 16.

$$R = 2\pi\left[\frac{\Gamma}{mG_c\xi_c - G}\right]^{1/2} \qquad \text{(Equation 16)}$$

Where *R* is the dendrite tip radius, G_c is the concentration gradient of the solute at the liquid-solid interface. An example of the relationship between R and V is shown in Figure 1-9.

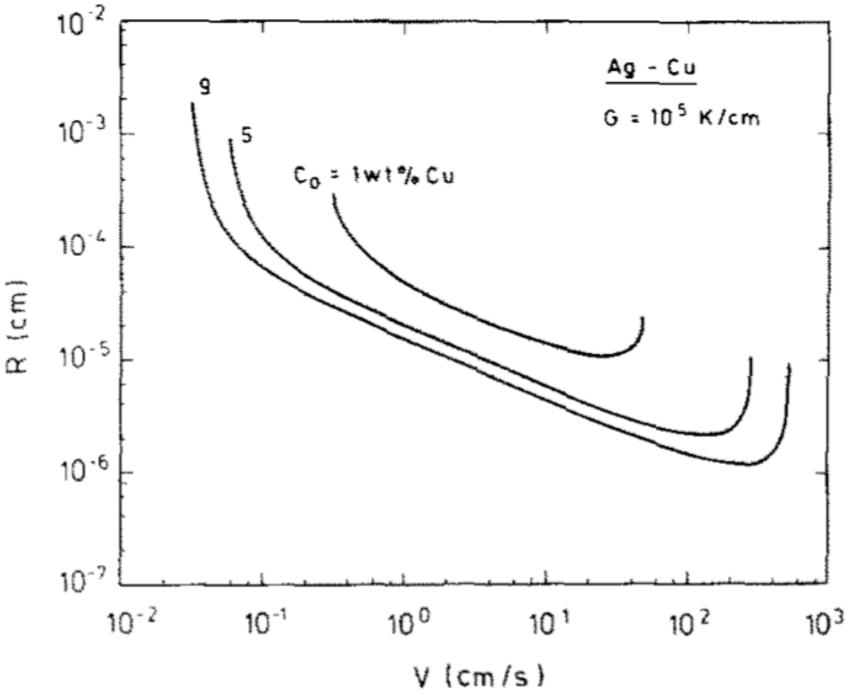

Figure 1-9- An example of the dendrite tip radius (R) as a function of solidification front velocity (V) as calculated by the KGT model for an Ag-Cu alloy [36].

It can be seen that the KGT model predicts a decrease in R with an increase in SFV, however further increasing the SFV results in an increase in the dendrite tip radius. This increase in dendrite tip radius is associated with the formation of a planar interface and is known as absolute stability. Studies investigating the distribution of solute during solidification at velocities in the range required for absolute interface stability have reported non-equilibrium partitioning.

Baker and Cahn first reported non-equilibrium segregation of solute during rapid solidification [37]. The authors studied splat-quenched samples in the zinc-cadmium system and determined that there was a departure from local equilibrium and the liquid-solid interface during solidification. This phenomenon was then coined "Solute

Trapping". Aziz then developed the Continuous Growth Model (CGM) for solute trapping to describe the solute trapping phenomenon [38]. The CGM predicted that when the liquid-solid interface advances at a rate that is greater than the diffusive speed of the solute within the solvent, then the solute will become engulfed by the growing solid phase, and be unable to partition in an equilibrium manner [38].

The CGM for solute trapping estimates the effective partition coefficient during solidification as a function of SFV, as shown in Equation 17.

$$k(v) = \frac{\frac{v}{v_D} + k_{eq}}{\frac{v}{v_D} + 1} \qquad \text{(Equation 17)}$$

Where v is the SFV, v_D is the diffusive speed, and k_{eq} is the equilibrium partition coefficient. As an example the CGM for solute trapping was used to calculate the effective partition coefficient of silicon in aluminum as a function of SFV (see Figure 1-10).

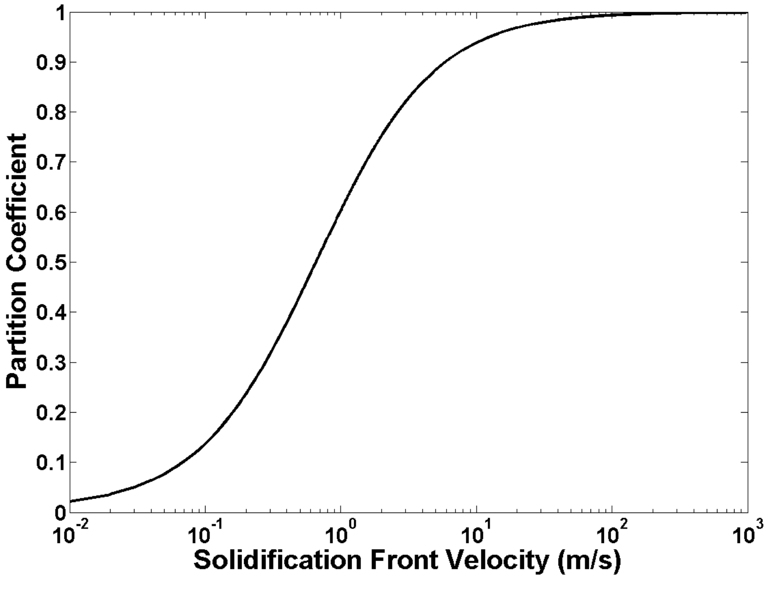

Figure 1-10- CGM for solute trapping displaying the effective partition coefficient as a function of solidification front velocity.

Aziz et al. validated the CGM for solute trapping through the analysis of rapidly solidified silicon-bismuth alloys [39], while Smith and Aziz found that the CGM accurately described the solute trapping behavior of several dilute binary aluminum alloys (Al-Sn, Al-Cu, Al-Ge, and Al-In) [40].

Meco and Napolitano then employed the melt spinning technique to an Al-Sm binary alloy [41]. The authors reported formation of a microstructure consisting of aluminum and the $Al_{11}Sm_3$ phase. The retention of this phase, metastable below temperatures of 1333K, at room temperature, and the extension of the degree of supersaturation of Sm in Al with respect to equilibrium conditions indicated that non-equilibrium partitioning occurred during the RSP.

The ability of RSP to induce non-equilibrium partitioning of solute makes it of extreme interest when attempting to solidify material without inducing microsegregation. As the goal of this study is to deposit an Al-Li-Cu alloy without inducing significant microsegregation, RSP techniques will be investigated. In particular three techniques that are capable of depositing material with high cooling-rates and high-thermal gradients will be discussed including; Controlled-Short-Circuiting Metal-Inert-Gas (CSC-MIG) welding, Laser Re-melting (LRM), and Electrospark Deposition (ESD).

1.3 Controlled-Short-Circuiting Metal-Inert-Gas (CSC-MIG)

Originally patented by Guismann et al. in 2005, the Controlled-Shirt-Circuiting Metal-Inert-Gas (CSC-MIG) process was developed to address the issues of splatter formation and the lack of material transfer during traditional Gas-Metal-Arc-Welding (GMAW). Previously Pulsed-Gas-Metal-Arc-Welding (GMAW-P) and Short-Circuit GMAW (GMAW-S) had been developed to improve the lack of material transfer during GMAW processing, however both processes are susceptible to instabilities and spatter formation [42, 43]. To compensate for these instabilities, the CSC-MIG process is essentially a GMAW-P/GMAW-S hybrid process. The key advancement of this process is the ability to detect and control the mechanical loop formed between the electrode wire and weld pool and therefore direct the heat input to the wire tip, and ultimately reduce the heat input to the workpiece [43]. Therefore the CSC-MIG process and similar processes such as the Cold-Metal-Transfer (CMT) process developed by Fronius, have found applications where a reduction in heat input is of utmost importance.

1.3.1 Processing Equipment

The CSC-MIG process offers the ability to take advantage of both short-circuiting and pulsed GMAW transfer modes. This is accomplished through the application of a real-time voltage and current monitoring system, in conjecture with a set of high frequency stepper-motors to supply fine wire position control. There are four distinct phases within the CSC-MIG process as shown in Figure 1-11; (a) the short-circuiting phase, (b) the disruption of the short-circuit (liquid bridge), (c) retraction of the wire to the desired arc length along and initiation of the arcing phase, (d) droplet formation and wire translation toward the weld pool [43].

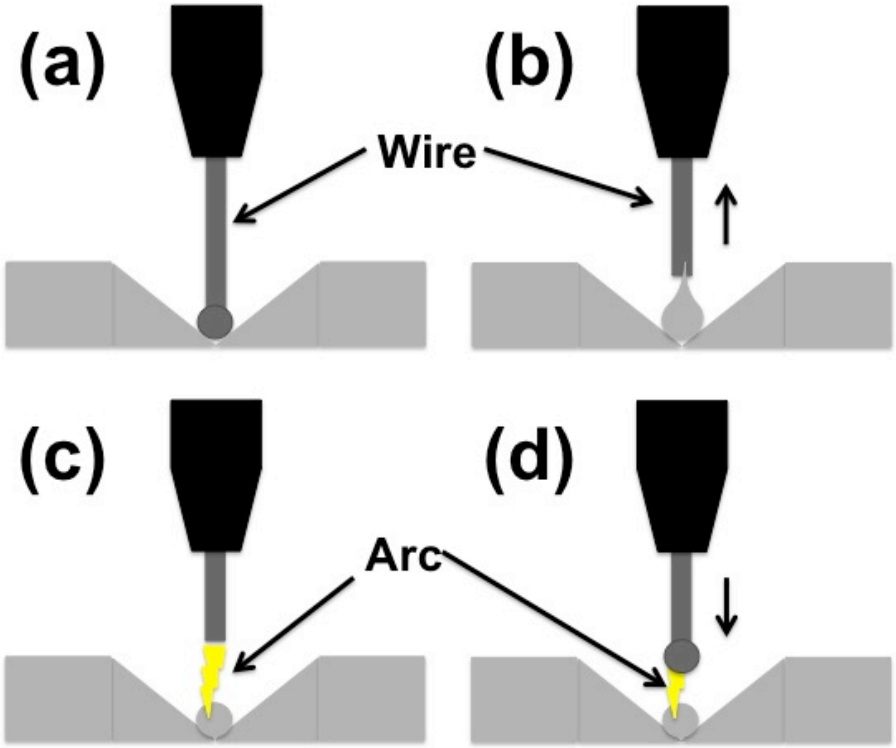

Figure 1-11- The four distinct phases of the CSC-MIG process.

The CSC-MIG apparatus also allows the user to input a short-duration high-intensity current pulse during both the arcing and short-circuiting phases. A typical current and voltage waveform for the CSC-MIG process is displayed in Figure 1-12.

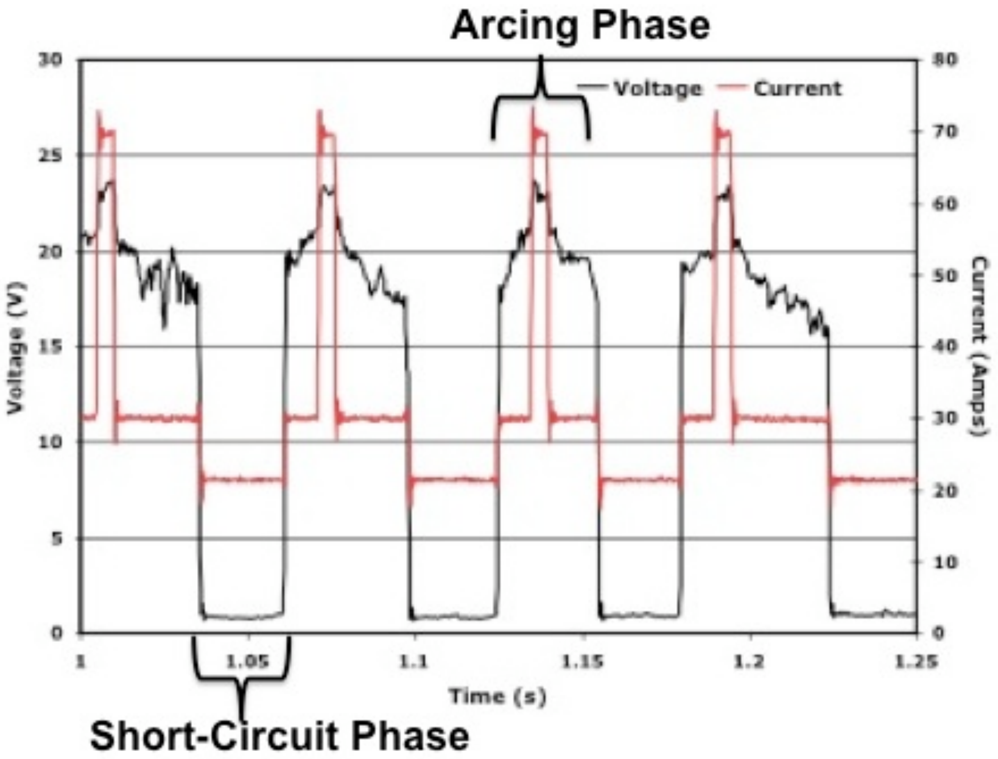

Figure 1-12 - Typical current and voltage waveforms for the CSC-MIG process.

As the heat-input of a CSC-MIG weldment can be calculated using Equation 18.

$$H_{net} = \int_{0}^{t} \frac{\eta E(t) I(t)}{v} \qquad \text{(Equation 18)}$$

Where η is the heat source efficiency, E is the welding voltage, I is the welding current, and v is the welding travel speed. Therefore by employing varying voltage and current waveforms during deposition, the CSC-MIG process allows the user to greatly reduce the heat-input to the workpiece. The short-circuiting phase results in a drop in baseline current as the mechanical loop offers little resistance, and the inclusion of short-duration high-intensity pulses reduces the mean current throughout the entirety of the process, and therefore significantly reduces the heat-input.

1.3.2 Previous studies involving CSC-MIG

As very little information regarding the CSC-MIG process is available in literature, the majority of the literature review will focus on the similar Cold-Metal-Transfer (CMT) process. As the CSC-MIG and CMT processes are both very low heat-input processes, the majority of studies have focused on exploiting the low heat-input to prevent the formation of undesirable microstructures.

A study by Pickin and Young investigated the ability of the CMT process to weld a difficult to join aluminum alloy (AA6111) [44]. The authors found that the reduced heat-input as a result of the combination of the short-circuiting and pulsed transfer mechanisms allowed for a high degree of control over the penetration depth during welding. Furthermore, it was determined that while the heat-input was decreased, a high wire melting coefficient was realized with respect to pulsed MIG processing, as a result of the directed heat-input towards the wire tip, thus reducing the thermal input to the base material. Similarly, Feng et al. reported that the low heat-input of the CMT process resulted in the ability to weld thin (1mm) pure aluminum sheets without inducing significant thermal distortions normally induced during GMAW processing [45].

Several studied have been performed to exploit the low heat-input and rapid solidification to prevent undesirable reactions from occurring, such as phase formation, during the CMT joining of dissimilar metals, and have reported mixed results. Wang et al. have shown that the very low heat-input of the CMT process was capable of preventing the formation of intermetallic compounds during the joining of aluminum and magnesium [46]. The authors reported that the rapid solidification occurring during CMT processing prevented significant diffusion of aluminum and magnesium and therefore inhibited the formation of the intermetallic compounds. However a more recent study by Cao et al. which focused on the joining of AZ31 and AA6061 found that the CMT process was unable to prevent detrimental intermetallic compounds from forming, and the resulting joints displayed low strength [47].

Pickin and et al. investigated the ability of the CMT process to deposit aluminum claddings [48]. The authors reported that the rapid solidification occurring during CMT processing prevented the solidification cracking associated with the ternary eutectic reactions, by inducing quasi-binary composition solidification.

Finally in an attempt to reduce the coarsening of the microstructure of previously deposited Ti-6Al-4V, during subsequent additive layered manufacturing (or solid freeform fabrication (SFF)) Almeida and Williams employed the CMT process [49]. The authors found that the CMT process was capable of producing spatter free deposits of Ti-6Al-4V, with a high deposition rate suitable to SFF. Furthermore, the CMT process offered a grain size reduction with respect to GTAW-P processes.

The rapid solidification of the CSC-MIG/CMT processes make them an interesting option to investigate for SFF of Al-Li alloys. Furthermore, as previously reported, the rapid solidification occurring during solidification may reduce the extent of microsegregation to occurring during solidification.

1.4 Laser Melting

Light amplification by stimulated emission of radiation (Laser) processing produces a high energy density source capable of welding, melting, or cutting many materials. Laser surface modification (LSM) or Laser re-melting (LRM) has been employed to induce structural or chemical changes to achieve improved mechanical properties or corrosion resistance. Non-equilibrium solidification has been shown to occur during LRM, as a small amount of material is melted while in contact with a large heat sink (substrate) [50, 51]. Furthermore, as the liquid pool is in contact with its own solid, the subsequent solidification does not involve nucleation and therefore simplifies the analysis [50].

1.4.1 Laser Melting Processing Equipment

Several different types of lasers may be employed to induce LRM including; carbon dioxide (CO_2) [50], diode [52], excimer, and neodymium doped yttrium aluminum garnet (Nd:YAG) lasers [53]. Nd:YAG lasers are the most common of the solid-state lasers employed today, and have found use within welding applications ranging from aerospace to dental surgery [54]. As an Nd:YAG laser was employed throughout this study, the following section will focus on the operating principles of this particular laser type.

An Nd:YAG laser is comprised of a YAG crystal ($Y_3Al_5O_{12}$) dope with a small amount (0.1-1%) Nd impurity. When an incident photon interacts with a dopant atom, the atom is excited to an increased energy state (E_x, where x=1, 2, 3..) above that of the initial ground state (E_0). The excited atom will retain this excited state for a period of time, before "relaxing" to the ground state by emitting a photon of the same wavelength and energy of the absorbed photon. If a second photon, with the same energy as the initial photon that excited the dopant atom, interacts (or stimulates) the excited atom, the excited atom will then immediately emit a photon with the same energy, phase, and polarizations as that of the stimulating photon [54]. This process is referred to as stimulated emission, and is the fundamental mechanism in which lasers operate. Therefore, to induce light amplification, the dopant atoms must be held in an excited state. This requires the formation of a non-equilibrium distribution of energy levels of the dopant atoms within the crystal. This non-equilibrium level is known as population inversion [54]. Once an inverted population is created, stimulation is performed by bombarding the crystal with photons either using lamps or a lower energy diode laser. This process is known as "pumping" the crystal and results in a coherent laser beam being emitted.

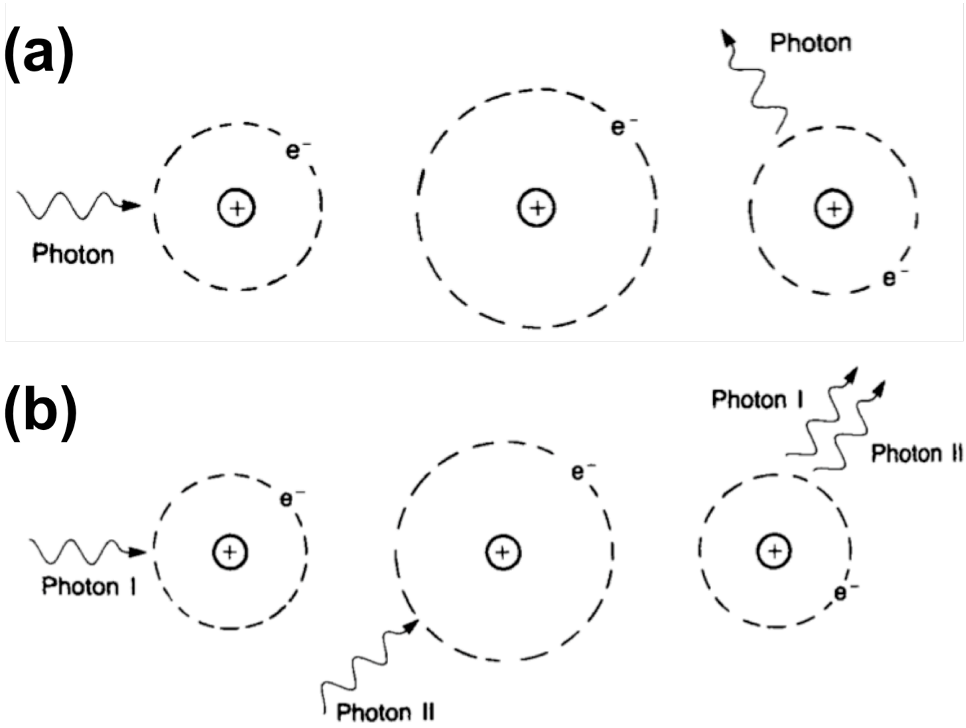

Figure 1-13- (a) Excitement of an atom due to interaction with a photon. (b) Stimulated emission of radiation due to the interaction of an energized electron with a secondary photon [54].

The laser beam may then be focused via a series of lenses or collimators to increase the power density (power per unit area) to facilitate processes such as laser re-melting or laser welding.

1.4.2 Previous Studies Involving LRM

The application of lasers to enhance the surface of a material through melting and re-solidification has been widespread. Zimmermann et al. employed a continuous CO_2 laser to re-melt an Al-Cu eutectic alloy and induce rapid solidification [50]. By varying the laser power and travel speed, the authors were able to control the SFV induced during solidification. It was determined that as the SFV was increased beyond ~50cm/s, the formation of the theta (Al_2Cu) phase was suppressed. This was believed to occur due to non-equilibrium partitioning resulting in the formation of a supersaturated solid solution (SSSS).

Aziz et al. and Smith and Aziz have employed LRM to study the solute trapping phenomenon within several different material systems, including silicon-bizmuth [39] and various dilute Al-X (X=Cu, Ge, In, Sn) alloys [40]. The authors ion implanted the desired solute into the host lattice, and then measured the solute depth profile before and after LRM. Through comparison of the change of solute profile with that expected for equilibrium and non-equilibrium partitioning, it was possible to determine the actual partition coefficient realized during solidification. The authors then concluded that LRM is capable of inducing SFV values in excess of 7.5m/s resulting in significant solute trapping.

Furthermore, LRM has been previously applied to additive manufacturing or SFF techniques. SFF processes such as selective laser sintering [55, 56], or solid wire melting have been employed to produce high quality SFF components [57]. Brandl et al. have reported the SFF of Ti-6Al-4V blocks using a solid-state laser and wire process [57]. The authors reported that it was possible to produce high strength components with low impurity levels using SFF via LRM of wire.

The combination of the high SFV's induced by LRM and the ability to produce components via an SFF LRM process, makes the LRM of great interest to for the application of SFF of Al-Li alloys.

1.5 ElectroSpark Deposition (ESD)

In 1924 Rawdon reported that the discharge of an electrical arc between an iron electrode and an iron plate resulted in the formation of martensite at the site where arcing occurred [58]. This result was later re-discovered by Welsh in 1957, while performing a study to determine the effect of frictional heating on the structure of steels [59], both Rawdon and Welsh noticed that the discharge of an electrical arc upon the steel resulted in the formation wear resistant skin upon the steel substrate [60]. Since this initial discovery, the ESD process has been known by several names including ElectroSpark Welding, High-Energy Micro-Arc Alloying (HEMAA), spark hardening, spark toughening, pulsed electrode surfacing (PES), or Electrospark alloying.

1.5.1 Processing equipment

ESD is a high energy-density, low heat-input micro-arc welding process [61], in which an arc is pulsed between an electrically conductive electrode (anode) of desired composition, and the work-piece (cathode). The process involves three distinct stages. Initial contact between the electrode and work-piece, induces resistive (joule) heating at the local contact site and results in the melting of both the electrode and substrate (Stage 1). The high current density at the contact sites then induces the formation of an electrical arc as the capacitor bank discharges (Stage 2). The arcing process produces a gap and prevents further discharge of a capacitor bank (Stage 3) [62]. A schematic representation of the transfer mechanism is shown in Figure 1-14.

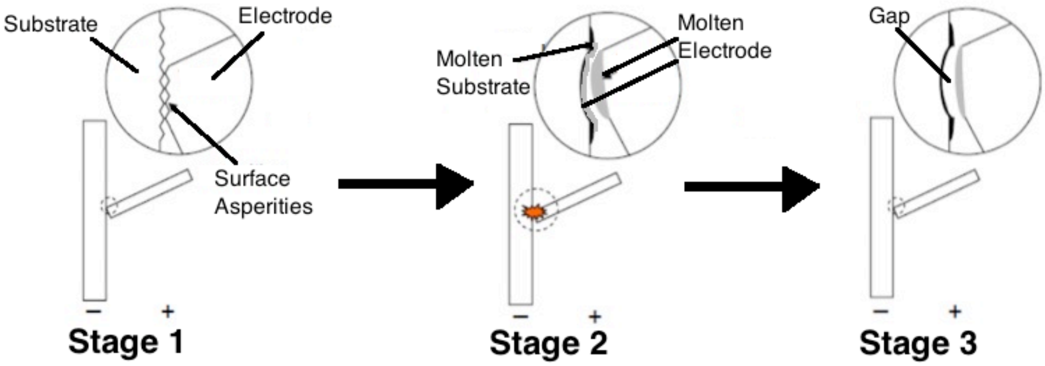

Figure 1-14- A schematic representation of the transfer mechanism of the ESD process [62].

Various methods have been applied to generate the spark required for ESD processing. Typically a bank of capacitors is charged then discharged through a handheld torch or applicator in which the electrode of desired composition is held, resulting in the formation of an arc between the substrate (workpiece) and the electrode (material to be deposited). The two most common methods of controlling this capacitor discharge are the application of a resistor-capacitor (RC) circuit or a microprocessor [63]. During the arc a fraction of the electrode material is then accelerated towards the substrate, and deposited in a splash pattern [64]. Throughout the process the relative movement of the electrode with respect to the work-piece via rotation, vibration, or oscillation [65] is used to prevent freezing of the electrode to the substrate. Throughout the process a shielding gas is normally employed, either by direct flow across the workpiece via the torch applicator, or by conducting the deposition within an enclosed atmospheric chamber. A schematic representation of the ESD process is displayed in Figure 1-15.

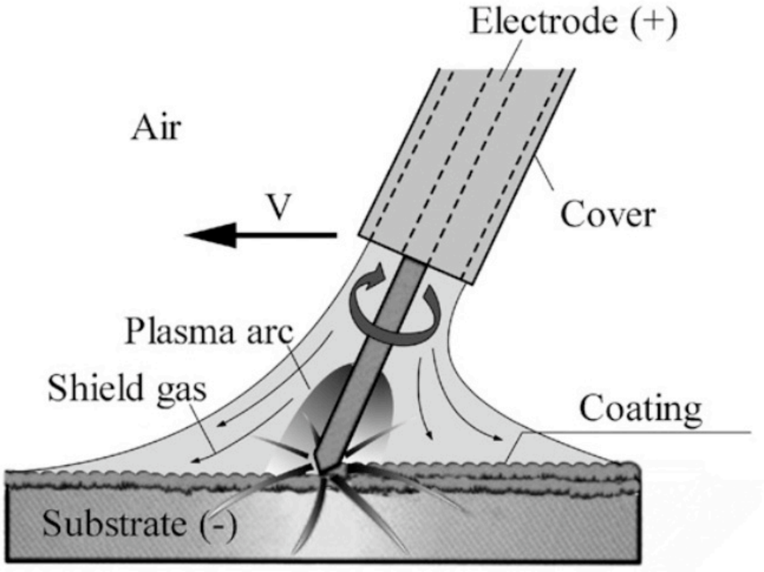

Figure 1-15 - Schematic representation of the ElectroSpark Deposition process [66].

The typical processing parameters of the ESD process include the properties of the electrode and substrate materials, such as composition, geometry, relative motion and velocity, contact pressure, and orientation [61]. As the atmosphere has also been shown to have a significant effect on the deposition mechanisms, the flow rate, flow geometry, gas temperature, and gas composition are of importance [61]. Finally the electrical properties of the process have a large influence in the deposition behavior, these properties include; power input, voltage, capacitance, as well as arc frequency and duration [61]. The pulse duration of the ESD process has been shown to be on the order of a few microseconds [61], and is strongly correlated with the capacitance [67]. An approximate pulse-energy can be calculated through the application of Equation 19.

$$E_{pulse} = \frac{1}{2} nCV^2 \qquad \text{(Equation 19)}$$

Where E_{pulse} is the pulse energy, C is the capacitance, and V is the voltage, and n is the fraction of capacitor discharge that occurs during arcing. Given that the capacitance values typically employed within ESD are on the order of micro-farads (μF) and the voltages employed are normally on the order of 50-200 volts, it can be seen that the energy of each pulse is typically on the order of 0.1-5 Joules. The low pulse energy, combined with the small amount of material deposited per pulse, and the short pulse duration induces high cooling-rates during ESD, on the order of 10^5-10^6 °C/s [68]. This high cooling-rate combined with the high thermal gradient inherent to the ESD process has been shown to result in the formation of metastable structures such as nanostructured metals [69, 70] or amorphous structures [71-73].

1.5.2 Previous Studies Involving ESD

As previously mentioned, initial investigations of the ESD process focused mainly on the production and study of wear resistant coatings [60, 74]. Resulting in one of the first industrial applications of the ESD process as a method of producing wear resistant coatings on cold-worked steel components within nuclear power plants [61]. However, more recent studies have capitalized on the low heat-input and high cooling-rates realized during ESD solidification to produce advanced microstructures.

Several research groups have deposited nanocrystalline metals using the ESD process. Heard and Brochu performed a study on the feasibility of applying the ESD process to refine the Al_3Ni intermetallic within the Al-Ni system [69]. The authors reported that the ESD process resulted in significant refinement of the microstructure. X-ray diffraction measurement of the grain size of the intermetallic phase revealed the grain size to be on the order of ~25nm, while electron microscopy reported a grain size closer to ~44nm.

Finally the authors showed that multiple layer deposition (up to 32 layers), did not result in any coarsening of the intermetallic phase present within the previously deposited material. A study by Wang et al. produced cavitation-erosion resistant Al-7%Si coatings via the ESD process [66]. It was determined that the improved erosion resistance stemmed from the formation of fine ~50nm silicon particles within the aluminum matrix. A similar study by Milligan et al. reported on the deposition of various eutectic and hypereutectic Al-Si binary alloys [70]. The authors reported significant reductions in the grain size of both aluminum and silicon within eutectic and hypereutectic binary aluminum-silicon alloys [70]. Xie and Wang investigated the ESD of several Ni-based superalloy systems [75-79]. The authors reported the formation of a fine cellular structure, and related this to the high level of constitutional supercooling occurring during solidification [75]. Cadney and Brochu, and Cadney et al. have also reported the deposition of zirconium [71] and aluminum based amorphous materials [71].

As CSC-MIG, LRM, and ESD are all rapid solidification techniques that may offer the ability to overcome issues plaguing Al-Li alloys such as solute segregation and lithium depletion, these techniques may be beneficial to producing new processing routes capable of improving the buy to fly ratio associated with the manufacturing of aerospace materials. A recently proposed manufacturing method that has shown promise to potentially further improve the buy to fly ratio is the Solid Freeform Fabrication technique.

1.6 Solid Freeform Fabrication

Solid Freeform Fabrication (SFF) is a near-net-shape fabrication technique originally developed to produce components for either prototype evaluation, or low volume finished production manufacturing [80]. SFF, also commonly referred to as rapid prototyping, layered manufacturing, or rapid tooling, is typically performed using wax, plastic, nylon, or polycarbonate materials through the application of procedures such as: stereolithography [81], laminated object manufacturing [82], fused deposition [83], selective laser sintering (SLS) [56] , and droplet deposition [84]. Recently, research has focused on adapting SFF processes to produce high quality functional metallic components through the application of GMAW [85-91], laser processing such as SLS [92] or selective laser melting (SLM) [93], or ESD [72].

1.6.1 SFF via Gas-Metal-Arc Welding

SFF via GMAW was first introduced by Ribeiro and Norrish in 1997 [94]. Ribeiro and Norrish equipped a programmable robot with a MIG welder, and used CAD/CNC package to control the layered manufacturing process. The authors produced several different objects such as a small vase (see Figure 1-16) and an automobile exhaust manifold.

Figure 1-16 – A small vase produced via GMAW-SFF by Ribeiro and Norish [94].

Beardsley and Kovacevic developed a novel welding parameter control system to fine-tune the heat-input and metal transfer during GMAW-SFF [95, 96]. The authors developed a modified pulsed-arc MIG process, resulting in precise control of weld bead droplet formation and detachment, thus enabling the direct control of bead height to width ratio. SFF tests were then performed, and it was determined that the control system was capable of producing multi-layer single weld deposits (thin wall welds), without slumping.

Wang et al. investigated SFF of AA4043 via a GTAW process [89]. The authors applied a variable polarity GTAW (VP-GTAW) process to produce components from AA4043.

It was reported that the cooling-rates realized in this study ranged from 10^2-10^3 K/s. The authors reported a variable microstructure throughout the component, ranging from a coarse cellular structure at the bottom (closest to the substrate) to a fine dendritic structure at the top. This microstructural variance correlated with a non-homogeneous hardness distribution throughout the component. This was believed to be due to the thermal effects of the subsequent deposition layers inducing a coarsening in the previously deposited material [89]. Finally, the precipitates were determined to be primarily located at interdendritic and grain boundary regions, indicative of equilibrium segregation occurring during solidification.

Almeida and Williams performed a study in which the CMT process was used as a method of SFF via GMAW to determine if the reduced heat-input resulted in more homogeneous microstructures [49]. The authors produced SFF components from Ti-6Al-4V using the CMT process. It was determined that the CMT process is capable producing consistent SFF components with high geometrical tolerance. It was also shown that the CMT process resulted in a significant reduction of grain size within the deposited material, with respect to the same material deposited via pulsed-GTAW.

Another study performed by Heard et al. applied the similar CSC-MIG process to SFF of AA4047 [97]. The authors found that the reduced heat-input of the CSC-MIG process resulted in minimal coarsening of the microstructure. It was determined that cooling-rates on the order 10^3 C/s were realized throughout the component. Finally the CSC-MIG SFF component was determined to display a similar flexural strength to that of a chill-cast equivalent alloy, however the SFF component revealed twice the ductility of the chill-cast samples. It was postulated that this increase in ductility was due to the refinement of the silicon phase as a result of the rapid cooling during deposition and solidification [97].

1.6.2 SFF via Laser Melting

SLS has been applied to perform SFF within metallic systems by Xie et al [92]. The authors applied a CO_2 laser to sinter a Ti-Mo alloy to produce a preform for processing via traditional sintering processes. It was determined that the SLS process was capable of producing a strong preform acceptable for subsequent sintering.

Zhang et al. investigated the SLM of tungsten to produce nanostructured components [98]. The authors found that as the scanning speed of the laser was increased, the density of the laser melted powders decreased. The laser re-melting of the tungsten powder then resulted in the formation of an ultrafine-grained (sub 500nm) microstructure. It was believed that this was due to the high degree of undercooling associated with the laser processing.

1.6.3 SFF via Electrospark Deposition

SFF via ESD has been performed by Wang et al. to facilitate the repair of a damaged turbine blade [99]. The authors deposited NiCoCrAlYTa alloy upon a DS DZ22 nickel-based superalloy. It was reported that the high cooling-rate and high thermal gradient of the ESD process resulted in a significant refinement of the deposited microstructure.

The current study focuses on the application of RSP to produce microsegregation free AA2199 deposits for SFF applications. The study will determine the processing parameters required to prevent solute segregation during solidification, while focusing on RSP techniques capable of depositing metallic material in a controllable manner. Ultimately SFF deposits of AA2199 will be metallurgically investigated to determine the aging response and microstructural evolution after RSP.

1.7 References

[1] Martin JW. Aluminum-Lithium Alloys. Annual Review of Materials Science 1988;18:101.
[2] Lavernia EJ, Grant NJ. Aluminium-lithium alloys. Journal of Materials Science 1987;22:1521.
[3] Assman P. MetallKd 1926;18:256.
[4] Czochralski J, Welter G. Alloy of Lithium and Aluminum. In: Office UP, editor, vol. 1,620,081. United States of America, 1927.
[5] Czochralski J. Aluminum Alloy Containing Lithium. In: Office UP, editor, vol. 1,620,082. United States of America, 1927.

[6] Rioja R, Liu J. The Evolution of Al-Li Base Products for Aerospace and Space Applications. Metallurgical and Materials Transactions A 2012:1.

[7] Le Baron IM. Aluminum Alloy. In: Patent U, editor, vol. No. 2,381,219, 1945.

[8] Kulkarni G, Banerjee D, Ramachandran T. Physical metallurgy of aluminum-lithium alloys. Bulletin of Materials Science 1989;12:325.

[9] T.H. Sanders J, E.A. Starke J, editors. Aluminum-Lithium Alloys. Proceedings 1st Int. Aluminum-Lithium Conf. Warrendale, Pa: TMS-AIME, 1981.

[10] Starke Jr EA, Sanders J, T.H., editors. Aluminum-Lithium Alloys II. Proc. 2nd Int. Aluminum-Lithium Conf. Warrendale, Penn: TMS-AIME, 1984.

[11] Baker C, Gregson PJ, Harris SJ, Peel CJ, editors. Aluminum-Lithium Alloys III. Proc. 3rd Int. Aluminum-Lithium Conf. London: Institute of Metals, 1986.

[12] Champier G, Dubost B, Miannay D, Sabetay L, editors. Proc. 4th Int. Aluminum-Lithium Conf. Les Ulis, France: Les Editions de Physique, 1987.

[13] Giummarra C, Thomas B, Rioja RJ. NEW ALUMINUM LITHIUM ALLOYS FOR AEROSPACE APPLICATIONS. Proceedings of the Light Metals Technology Conference 2007 2007.

[14] Kim H-J, Niinomi M. The role of microstructures on the strengthening mechanisms of a thermomechanically processed 2091 Al-Li alloy. Materials Science and Engineering A 2000;284:14.

[15] Ivanov R. The effects of friction stir welding on the mechanical properties and microstructure of a third generation Al-Li alloy. Mining and Materials Engineering, vol. Master of Applied Science (Thesis): McGill University, 2012.

[16] Cassada WA, Shiflet GJ, Starke EA. The effect of plastic deformation on Al2CuLi (T 1) precipitation. MTA 1991;22:299.

[17] Vasudévan AK, Fricke WG, Malcolm RC, Bucci RJ, Przystupa MA, Barlat F. On through thickness crystallographic texture gradient in Al-Li-Cu-Zr alloy. MTA 1988;19:731.

[18] Rioja RJ. Fabrication methods to manufacture isotropic Al-Li alloys and products for space and aerospace applications. Materials Science and Engineering: A 1998;257:100.

[19] Papazian J, Schulte R, Adler P. Lithium depletion during heat treatment of aluminum-lithium alloys. Metallurgical and Materials Transactions A 1986;17:635.

[20] Williams DB, Edington JW. Microanalysis of Al-Li alloys containing fine 6′ (Al3Li) precipitates. Philosophical Magazine 1974;30:1147.

[21] Papazian JM, Schulte RL. Lithium diffusion in aluminum-lithium alloy 2090 clad with 7072. MTA 1990;21:39.

[22] Esposto FJ, Zhang CS, Norton PR, Timsit RS. Segregation studies of an Al---Li alloy. Surface Science 1993;290:93.

[23] Berzina IG, Gusev EB, Ivanov VA, Lukin VI. Investigation of Li distribution in aluminium alloy welds by elemental radiographic analysis. International Journal of Radiation Applications and Instrumentation. Part D. Nuclear Tracks and Radiation Measurements 1992;20:261.

[24] Williams DB, Carter CB. Transmission Electron Microscopy: A Textbook for Materials Science New York: Springer 2009.

[25] Flerov G, Berzina I. Radiographic methods for elemental analysis of boron, lithium, radium, uranium and thorium in minerals and rocks. Journal of Radioanalytical and Nuclear Chemistry 1973;16:461.

[26] Kaufman MJ, Morrone AA, Lewis RE. Complications concerning TEM analysis of the [delta]-AlLi phase in aluminum-lithium alloys. Scripta Metallurgica et Materialia 1992;27:1265.
[27] Kurz W, Fisher DJ. Fundamentals of Solidification. Switzerland: Trans Tech Publications, 1998.
[28] Kou S. Welding Metallurgy. New Jersey: John Wiley & Sons Inc., 2003.
[29] Dantzig JA, Rappaz M. Solidification: EPFL Press, 2009.
[30] Clyne TW, Kurz W. Solute redistribution during solidification with rapid solid state diffusion. MTA 1981;12:965.
[31] Glicksman ME. Principles of Solidification: An introduction to modern casting and crystal growth concepts: Springer, 2010.
[32] Brody HD, Flemings MC. Trans. TMS-AIME 1966;236:615.
[33] Flemings MC, Poirier DR, Barone RV, Brody HD. J. Iron Steel Inst. 1970;208:371.
[34] Mullins WW, Sekerka RF. Stability of a Planar Interface During Solidification of a Dilute Binary Alloy. Journal of Applied Physics 1964;35:444.
[35] Coriell SR, Sekerka RF. In: Mehrabian R, Kear BH, Cohen M, editors. Rapid Solidification Processing Principles and Technologies. 1980. p.35.
[36] Kurz W, Giovanola B, Trivedi R. Theory of microstructural development during rapid solidification. Acta Metallurgica 1986;34:823.
[37] Baker JC, Cahn JW. Solute trapping by rapid solidification. Acta Metallurgica 1969;17:575.
[38] Aziz MJ. Model for solute redistribution during rapid solidification. Journal of Applied Physics 1982;53:1158.
[39] Aziz MJ, Tsao JY, Thompson MO, Peercy PS, White CW. Solute Trapping: Comparison of Theory with Experiment. Physical Review Letters 1986;56:2489.
[40] Smith PM, Aziz MJ. Solute trapping in aluminum alloys. Acta Metallurgica et Materialia 1994;42:3515.
[41] Meco H, Napolitano RE. Non-Equilbrium Solute Partitioning and Microstructure Formation in Rapidly Solidified Al-Sm Alloys. Material Science Forum 2007;539-543:2810.
[42] Huismann G, Hoffmeister H. Control of Short Circuiting in MIG-Process Under Hyperbaric Conditions. Offshore Mechanics and Artic Engineering. Libson, Portugal, 1998.
[43] Huismann G. Direct Control of the Material Transfer: The Controlled Short Circuiting (CSC)-MIG Process. ICAWT 2000: Gas Metal Arc Welding for the 21st Century. Orlando, Florida, 2000.
[44] Pickin CG, Young K. Evaluation of cold metal transfer (CMT) process for welding aluminium alloy. Science & Technology of Welding & Joining 2006;11:583.
[45] Feng J, Zhang H, He P. The CMT short-circuiting metal transfer process and its use in thin aluminium sheets welding. Materials & Design 2009;30:1850.
[46] Wang J, Feng JC, Wang YX. Microstructure of Al/Mg dissimilar weld made by cold metal transfer MIG welding. Materials Science and Technology 2008;24:827.
[47] Cao R, Wen BF, Chen JH, Wang P-C. Cold Metal Transfer joining of magnesium AZ31B-to-aluminum A6061-T6. Materials Science and Engineering: A 2013;560:256.

[48] Pickin CG, Williams SW, Lunt M. Characterisation of the cold metal transfer (CMT) process and its application for low dilution cladding. Journal of Materials Processing Technology 2011;211:496.
[49] Almeida PMS, Williams S. Innovative process model of Ti-6Al-4V additive later manufacturing using cold metal transfer (CMT). Solid freeform fabrication symposium, 2010.
[50] Zimmermann M, Carrard M, Kurz W. Rapid solidification of Al-Cu eutectic alloy by laser remelting. Acta Metallurgica 1989;37:3305.
[51] Watkins KG, McMahon MA, Steen WM. Microstructure and corrosion properties of laser surface processed aluminium alloys: a review. Materials Science and Engineering: A 1997;231:55.
[52] Lawrence J, Li L, Spencer JT. Diode laser modification of ceramic material surface properties for improved wettability and adhesion. Applied Surface Science 1999;138–139:388.
[53] Cui L, Li X, He D, Chen L, Gong S. Effect of Nd:YAG laser welding on microstructure and hardness of an Al–Li based alloy. Materials Characterization 2012;71:95.
[54] Hitz CB, Ewing J, Hecht J. Introduction to Laser Technology, 4th Edition: IEEE, 2012.
[55] Yu P, Schaffer GB. Microstructural evolution during pressureless infiltration of aluminium alloy parts fabricated by selective laser sintering. Acta Materialia 2009;57:163.
[56] Schmidt M, Pohle D, Rechtenwald T. Selective Laser Sintering of PEEK. CIRP Annals - Manufacturing Technology 2007;56:205.
[57] Brandl E, Palm F, Michailov V, Viehweger B, Leyens C. Mechanical properties of additive manufactured titanium (Ti–6Al–4V) blocks deposited by a solid-state laser and wire. Materials & Design 2011;32:4665.
[58] Rawdon HS. Trans. Am. Inst. Mech. Eng. 1924;79.
[59] Welsh NC. Frictional Heating and Its Influence on the Wear of Steel. Journal of Applied Physics 1957;28:960.
[60] Welsh NC. Surface Hardening of Non-ferrous Metals by Spark Discharge. Nature 1958;181:1005.
[61] Johnson RN, Sheldon GL. Advances in the electrospark deposition coating process. Journal of Vacuum Science & Technology A: Vacuum, Surfaces, and Films 1986;4:2740.
[62] Tang SK. The Process Fundamentals and Parameters of Electro-Spark Deposition. Mechanical Engineering, vol. Master of Applied Science. University of Waterloo: University of Waterloo, 2009.
[63] Wang P-Z, Pan G-S, Zhou J-X, Shao H-S. Accelerated Electrospark Deposition and the Wear Behavior of Coatings. Journal of Materials Engineering and Performance 1997;6:780.
[64] Liu J, Wang R, Qian Y. The formation of a single-pulse electrospark deposition spot. Surface and Coatings Technology 2005;200:2433.
[65] Lesnjak A, Tusek J. Processes and properties of deposits in electrospark deposition. Science and Technology of Welding and Joining 2002;7:391.
[66] Wang W-f, Wang M-c, Sun F-j, Zheng Y-g, Jiao J-m. Microstructure and cavitation erosion characteristics of Al-Si alloy coating prepared by electrospark deposition. Surface and Coatings Technology 2008;202:5116.

[67] Reynolds JL, Holdren RL, Brown LE. Electro-spark deposition. Advanced Materials & Processes 2003;161:35.

[68] Johnson RN. ElectroSpark Deposition: Principles and Applications. 45th Annual Technical Conference Proceedings 2002:87.

[69] Heard DW, Brochu M. Development of a nanostructure microstructure in the Al-Ni system using the electrospark deposition process. Journal of Materials Processing Technology 2010;210:892.

[70] Milligan J, Heard DW, Brochu M. Formation of nanostructured weldments in the Al-Si system using electrospark welding. Applied Surface Science 2010;256:4009.

[71] Cadney S, Brochu M. Formation of amorphous Zr41.2Ti13.8Ni10Cu12.5Be22.5 coatings via the ElectroSpark Deposition process. Intermetallics 2008;16:518.

[72] Brochu M, Heard DW, Milligan J, Cadney S. Bulk nanostructure and amorphous metallic components using the electrospark welding process. Assembly Automation 2010;30:248.

[73] Brochu M, Portillo JG, Milligan J, Heard DW. Development of Metastable Solidification Structures Using the Electrospark Deposition Process. The Open Surface Science Journal 2011;3:105.

[74] Welsh NC, Watts PE. The wear resistance of spark-hardened surfaces. Wear 1962;5:289.

[75] Xie Y-j, Wang M-c. Microstructural morphology of electrospark deposition layer of a high gamma prime superalloy. Surface and Coatings Technology 2006;201:691.

[76] Xie Y-j, Wang M-c. Epitaxial MCrAlY coating on a Ni-base superalloy produced by electrospark deposition. Surface and Coatings Technology 2006;201:3564.

[77] Xie Y-j, Wang M-c. A feasibility study of preparing MCrAlX/BN composite coatings by electrospark deposition process. Journal of Alloys and Compounds 2009;484:21.

[78] Xie Y-j, Wang M-c. Isothermal oxidation behavior of electrospark deposited MCrAlX-type coatings on a Ni-based superalloy. Journal of Alloys and Compounds 2009;480:454.

[79] Xie Y-j, Wang M-c, Huang D-w. Comparative study of microstructural characteristics of electrospark and Nd:YAG laser epitaxially growing coatings. Applied Surface Science 2007;253:6149.

[80] Siminski MR. Weld path optimisation for rapid prototyping and wear replacement by robotic gas metal arc welding. Mechanical Engineering, vol. Doctor of Philosophy. Wollongong: University of Wollongong, 2003.

[81] Seitz H, Tille C, Irsen S, Bermes Gn, Sader R, Zeilhofer H-F. Rapid Prototyping models for surgical planning with hard and soft tissue representation. International Congress Series 2004;1268:567.

[82] Tari MJ, Bals A, Park J, Lin MY, Thomas Hahn H. Rapid prototyping of composite parts using resin transfer molding and laminated object manufacturing. Composites Part A: Applied Science and Manufacturing 1998;29:651.

[83] Masood SH, Song WQ. Development of new metal/polymer materials for rapid tooling using Fused deposition modelling. Materials & Design 2004;25:587.

[84] Yingxue Y, Shengdong G, Chengsong C. Rapid prototyping based on uniform droplet spraying. Journal of Materials Processing Technology 2004;146:389.

[85] Siminski MR, De Boer FG. Build Strategies for Rapid Prototyping and Wear Replacement by Gas Metal Arc Welding. WTIA 49th Annual Conference. Adelaide, Australia: Welding Technology Institute of Australia, 2001.
[86] Siminski MR, De Boer FG. Weld Path Generation for Rapid Prototyping and Wear Replacement by Robotic Gas Metal Arc Welding. WTIA 50th Annual Conference. Sydney Australia, 2002.
[87] Siminski MR, De Boer FG. Effects of Weld Path Strategies on Stability of Rapid Prototyping by Robotic GMAW. IIW Asian Pacific International Congress. Singapore, 2002.
[88] Spencer J, Dickens P, Wykes C. Rapid prototyping of metal parts by three-dimensional welding. Proceedings of the Institution of Mechanical Engineers, Part B: Journal of Engineering Manufacture 1998;212:175.
[89] Wang H, Jiang W, Ouyang J, Kovacevic R. Rapid prototyping of 4043 Al-alloy parts by VP-GTAW. Journal of Materials Processing Technology 2004;148:93.
[90] Zhang Y, Chen Y, Li P, Male AT. Weld deposition-based rapid prototyping: a preliminary study. Journal of Materials Processing Technology 2003;135:347.
[91] Zhang YM, Li P, Chen Y, Male AT. Automated system for welding-based rapid prototyping. Mechatronics 2002;12:37.
[92] Xie F, He X, Lu X, Cao S, Qu X. Preparation and properties of porous Ti–10Mo alloy by selective laser sintering. Materials Science and Engineering: C 2012.
[93] Wang Z, Guan K, Gao M, Li X, Zeng X. Tensile properties of 304 stainless steel fabricated by selective laser melting. Optical Society of America, 2012. p.MF1B.4.
[94] Ribeiro F, Norrish J. Making components with controlled metal deposition. IEEE International Symposium on Industrial Electronics, vol. 3. Guimaraes, Portugal, 1997. p.831.
[95] Beardsley H, Kovacevic R. Controlling Heat Input and Metal Transfer for 3D Welding-Based Rapid Prototyping. The 5th International Conference on Trends in Welding Research. Pine Mountain, Georgia, 1998.
[96] Kovacevic R. Rapid Manufacturing of Functional Parts Based on Deposition by Welding and 3D Laser Cladding. Mold Making Conference. Rosemont, IL, USA: Mold Making Magazine, 2001. p.263.
[97] Heard DW, Brophy S, Brochu M. Solid freeform fabrication of Al-Si components via the CSC-MIG process. Canadian Metallurgical Quarterly 2012;51:302.
[98] Zhang D, Cai Q, Liu J. Formation of Nanocrystalline Tungsten by Selective Laser Melting of Tungsten Powder. Materials and Manufacturing Processes 2012;27:1267.
[99] Wang M-c, Wang W-f, Xie Y-j, Zhang J. Electro-spark epitaxial deposition of NiCoCrAlYTa alloy on directionally solidified nickel-based superalloy. Transactions of Nonferrous Metals Society of China 2010;20:795.

2 Objectives

As aerospace manufacturers strive to reduce the fuel consumption of their vehicles, weight reduction is a common and effective strategy. Aluminum-lithium (Al-Li) alloys have been gaining increasing attention, as they offer a reduction in density with respect to traditional aerospace aluminum alloys such as aluminum-copper (AA2024) and aluminum-zinc (AA7075). Furthermore, novel manufacturing techniques such as Solid Freeform Fabrication (SFF) have recently proven capable of producing high quality structural components, therefore allowing aerospace manufacturers the ability to further improve the buy to fly ratio. Improving the buy to fly ratio therefore increases the attractiveness of Al-Li alloys being implemented, as one limiting factor has been the high cost of Al-Li alloys relative to the Al-Cu or Al-Zn incumbent materials. As SFF typically involves the local melting, deposition, and solidification of the desired alloy, solidification phenomenon such as microsegregation can influence the integrity of the resulting components. As many aluminum alloys experience solute segregation during solidification, due to equilibrium partitioning of solute elements, thermo-mechanical homogenization processes (TMP) are typically employed in casting house operations. As the SFF process is a near-net-shape manufacturing technique, the application of a TMP would negate the benefits of the manufacturing process. It is therefore of interest to investigate the solidification conditions required to minimize or remove microsegregation effects during SFF deposition.

The objective of this research project is to investigate the ability of three rapid solidification processes (RSP) that are applicable to SFF processing, to reduce or remove microsegregation during the solidification of an Al-Li-Cu alloy (AA2199). Controlled-Short-Circuiting Metal-Inert-Gas (CSC-MIG), Laser Re-melting (LRM), and Electrospark Deposition, are three RSP techniques that will be employed to determine the solidification conditions required for microsegregation-free solidification, and ultimately perform featureless solidification of AA2199. Finally, the effect of the RSP on the aging response of the alloy will be investigated to determine if it is possible to circumnavigate the cold-working process typically applied to Al-Li alloys prior to aging.

3 Experimental Methodology and Apparatus

3.1 Controlled-Short-Circuiting-MIG

A Machitech XYZ automated table, controlled using DeskCNC software, equipped with a JetLine Engineering Controlled-Short-Circuit Metal-Inert-Gas (CSC-MIG) welding machine (see Figure 3-1) was employed to facilitate deposition of the Al-Li alloy 2199. The automated table is controlled by executing machine tool path programs created in G-code. Welding trials were performed upon rectangular coupons of aluminum alloy 6061 with the dimensions depicted in Figure 3-2. This coupon geometry and weld position was selected due to a desirable temperature distribution as predicted by two-dimensional heat-flow modeling results.

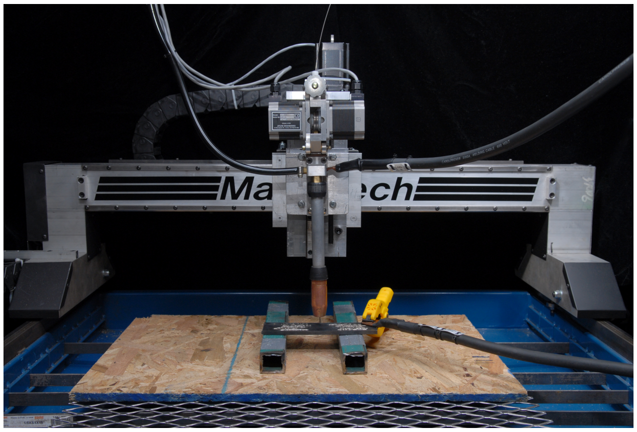

Figure 3-1 - JetLine Engineering CSC-MIG mounted on a Machitech XYZ table.

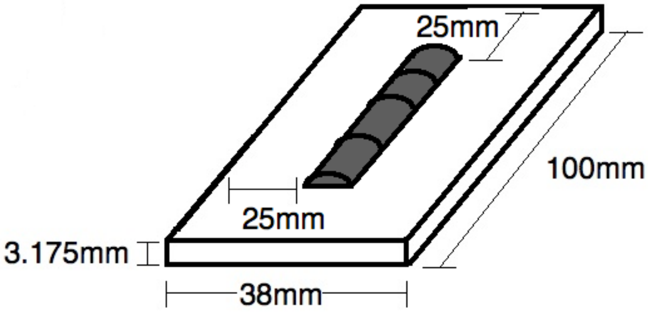

Figure 3-2 - Dimensions of AA6061 coupons used as a substrate for the welding trials.

The welding wire used throughout the study was produced from thin sheet of the AA2199 alloy in the T3 condition, by cutting ~1cm wide strips, followed by cold-rolling to a diameter of ~2mm. The heat-input of the CSC-MIG process was measured real-time through the application of an Impact Welding Arc Agent 3000P welding oscilloscope. The Arc Agent software then calculated and logged the average instantaneous heat-input through analysis of the instantaneous applied voltage and current. Prior to deposition the substrates were ground using 600grit SiC paper and de-greased with acetone to ensure consistency.

3.2 Electrospark Deposition (ESD)

ESD experiments were performed using a TechnoCoat MicroDepo model 150 and a TechnoCoat SparkDepo model 300 machines (see Figure 2-3 (a) and (b)) with a potential applied voltage range of 50 to 150 V, and a capacitance ranging from 2.2 to 302.2 μF. The spark frequency can be ranged from 60 to 2000 Hz. Deposition trials throughout this study were performed with a voltage of 100 V and a capacitance of 100 μF. The Standard Application (rotational tool) was employed with a rotational speed of ~500rpm. A pulse frequency of 390Hz was employed throughout the experiments. The AA2199 electrodes were manufactured from thin plate AA2199 product in the T3 (solutionized, stretched, and naturally aged) condition. The thin plate was then sectioned, and rolled until a circular cross-section with a diameter of ~1.75mm was achieved. Prior to deposition the electrodes were cleaned in an ultrasonic bath of acetone. The heat-input of deposition per pulse was calculated using Equation 3-1.

$$HI = \frac{1}{2}CV^2 \qquad \text{(Equation 3-1)}$$

Where *HI* is the heat-input, *C* is the capacitance, and *V* is the applied voltage. All ESD trials were performed within a high-purity argon atmosphere obtained via a Vacuum Atmosphere Systems glove box (see Figure 3-3). Trials were performed with an O_2 concentration of <0.1ppm and <1ppm Trace Moisture (H_20).

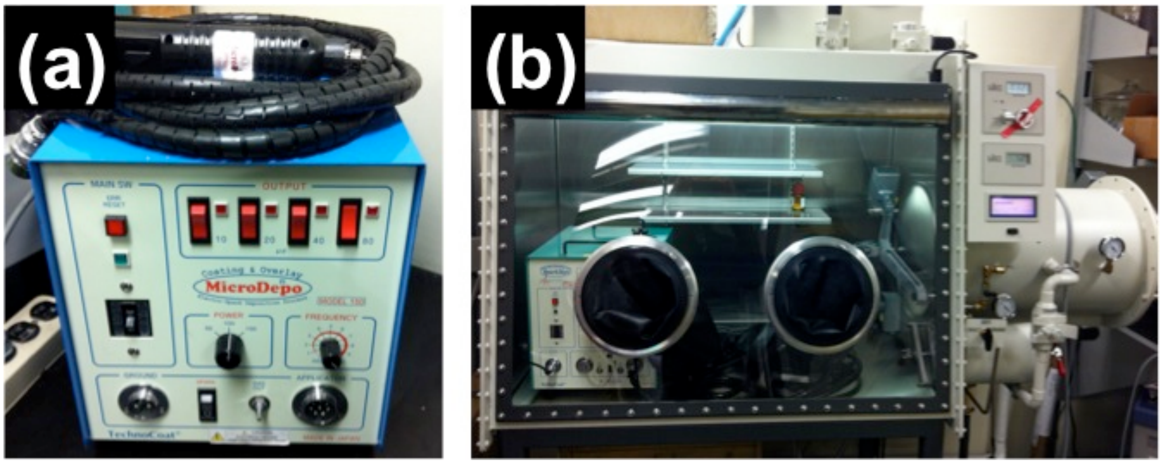

Figure 3-3 – Experimental set-up for the ESD trials. (a) ESD unit employed throughout the study, (b) glove box used to achieve a high purity argon atmosphere for the ESD trials.

3.3 Pulsed-Laser Remelting (PLM)

The PLM samples were manufactured using a Miyacki LW25 neodymium doped yttrium aluminum Garnet (Nd:YAG) micro-laser welding system with an emission wavelength (λ) of 1064nm (the set-up is shown in Figure 3-4). The approximate spot size of the laser is ~150 μm. The laser was mounted on a Machitech XYZ automated table. DeskCNC software, programed using the G-Code language, was used to control the laser table. Laser re-melting was performed in a custom-built argon environmental chamber; the laser was fired through a port of Edmunds Optics laser transparent glass (shown in Figure 3-4(b)). Prior to re-melting a series of three five minute long evacuations and argon back-fills were performed, to ensure the formation of an inert atmosphere within the chamber. Re-melting was performed on a 12.5 by 7.0 mm area, with a laser travel speed of 127 mm/min. The original parent material used for the re-melting experiments was the as-received AA2199 material in thin-sheet form (3mm thickness), in the T3 heat-treated condition. The focal point (~50mm) of the laser was placed upon the surface of the sheet of AA2199 to be re-melted. The laser parameters used throughout this study included a pulse frequency (pulse repetition rate) of 30 pulse-per-second, a pulse duration of 0.5ms, and pulse energies ranging from 0.125-0.5J.

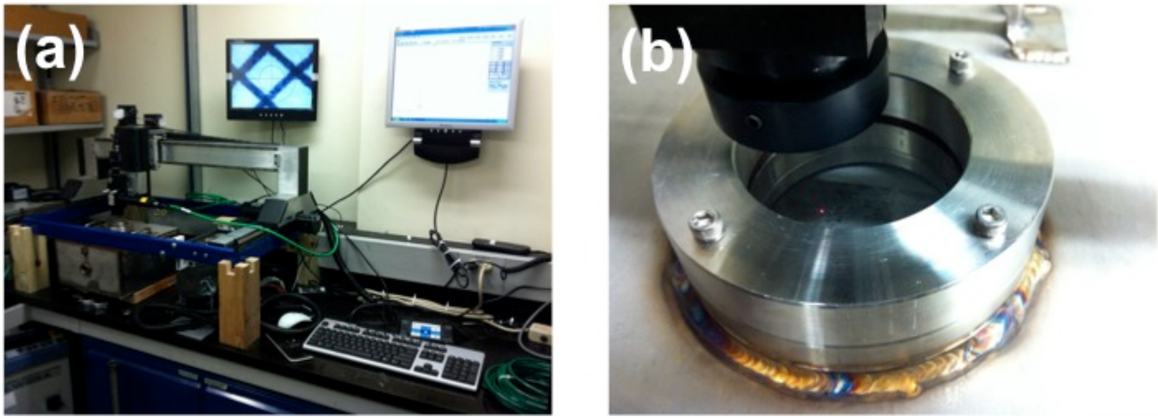

Figure 3-4- The Laser-Remelting set-up employed to perform rapid solidification via laser re-melting, (a) automated laser apparatus, (b) close up of laser transparent port into atmosphere chamber.

3.4 Optical Microscopy

Optical microscopy was performed using both a Nikon light optical microscope and Nikon Stereoscope equipped with a Clemex Vision System. Samples were sectioned, mounted in Bakelite and then ground using 320 grit SiC paper, followed by polishing with 9, 3 and, 1μm diamond suspension, then finishing with 0.05μm colloidal silica. Grinding and polishing were performed using a Buhler Ecomet-3 autopolisher equipped with an Automet-2 head.

3.5 Scanning Electron Microscopy

Scanning Electron Microscopy (SEM) was performed using a Hitachi S-4700, Hitachi SU-8000, Hitachi S3400-N, as well as a Phillips XL-30 FE-SEM electron microscope. SEM analysis was performed on samples that were prepared in the same manner as those for optical microscopy. High-resolution SEM imaging was performed within the SU-8000 at low accelerating voltages (~5kV) to minimize the interaction volume. The electron beam interaction volume was estimated using the Casino Monte Carlo modeling software.

Energy Dispersive Spectroscopy (EDS) chemical analysis was performed using a Phillips XL-30 FE-SEM. Samples were prepared using the previously mentioned process of preparation for a metallographic analysis. Spectra were acquired using an accelerating voltage of 20kV, a beam current of 348μA, and a collection time of 100 seconds. Semi-quantitative analysis was then performed by collecting spectra of pure standards of Al (99.999%) and Cu (99.999%) and using the DTSA-II Fornax software package to compare the known and unknown spectra.

3.6 X-Ray Photoelectron Spectroscopy (XPS)

XPS analysis was performed using a Thermo Scientific XPS system equipped with Avantage analytical software. Depth profiling was accomplished using argon ions accelerated a 3000eV, resulting in a Ta_2O_5/Ta equivalent etching rate of ~1.42nm/s. During data analysis the background was estimated using Shirley analysis.

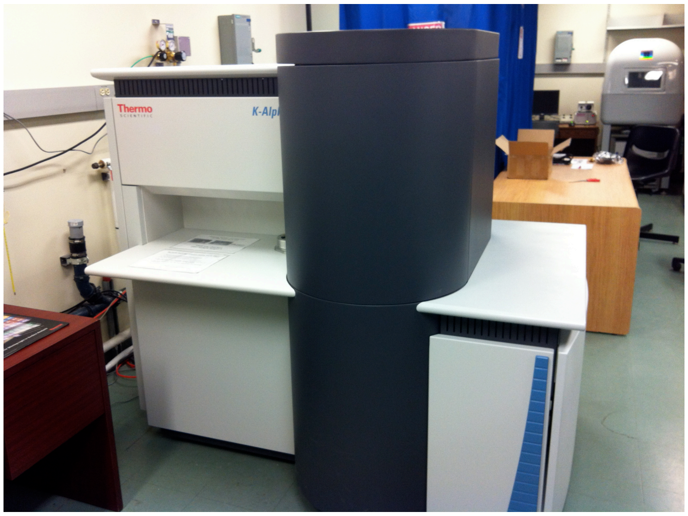

Figure 3-5- Thermo Scientific X-ray Photoelectron Spectroscopy system.

3.7 Time-of-Flight Secondary-Ion-Mass-Spectroscopy (TOF-SIMS)

TOF-SIMS analysis was performed at École Polytechnique de Montréal using an IONTOF TOF-SIMS IV (see Figure 3-6 (a) and (b)) in both negative and positive modes.

Bismuth ions were used for surface milling of the sample. Surface mapping and depth profiling were performed on the same TOF-SIMS instrument. TOF-SIMS depth profiling experiments were then repeated using the same parameters on a Ta_2O_5/Ta standard, and the resultant depth was then measured within an AFM to determine an approximate milling rate for the AA2199 samples.

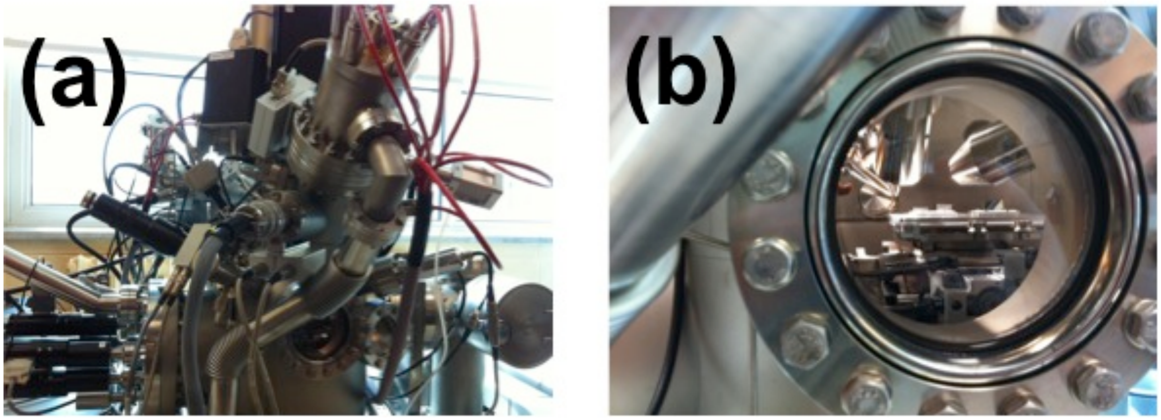

Figure 3-6- (a) TOF-SIMS instrument, (b) Close-up of the analysis chamber

3.8 Atom Probe Tomography

Atom Probe Tomography (APT) was performed using a LEAP4000XHR instrument located at the University of Michigan. Needles were prepared using a FEI Quanta 3D FEG Focused Ion Beam (FIB) microscope, with Ga ions as an etchant. Specimens were analyzed in both voltage and laser pulsing modes at a base temperature of 37K, with a pulse repetition rate of 200kHz, a evaporation rate of 0.005 atom/pulse, a voltage pulse amplitude of 15% or a laser pulse energy of 70pJ. The IVAS software was used for data reconstruction using an image compression factor of 1.2 and an evaporation field of 19V/nm.

3.9 Atomic Absorption (AA)

The bulk lithium concentration of the rapidly solidified material was measured through the application of AA. A Varian Atomic Absorption unit was employed. Samples were digested in a mixture of Nitric (HNO_3) and Hydrofluoric Acid (HF) then diluted to the appropriate concentration range prior to analyses. The AA machine was calibrated using lithium standards of varying concentrations prior to the measurement of the unknown samples.

Figure 3-7- Varian atomic absorption chemical analysis unit.

3.10 X-Ray Diffraction (XRD) Analysis

X-ray diffraction was performed using a Phillips PW1070 diffractometer (Cu Kα λ=1.54056Å) equipped with the HighScore Analytical software package, as well as a Bruker D8 Advance equipped with the AVA software package. Lattice parameter measurements were performed with a 2-theta scan range of 20-100 degrees. A silicon standard was used during all lattice parameter measurements, and the resulting lattice parameter was calculated using the XLat software package [1]. The x-ray penetration depth was estimated through the application of the AbsorbDX software package (Version 1.1.4).

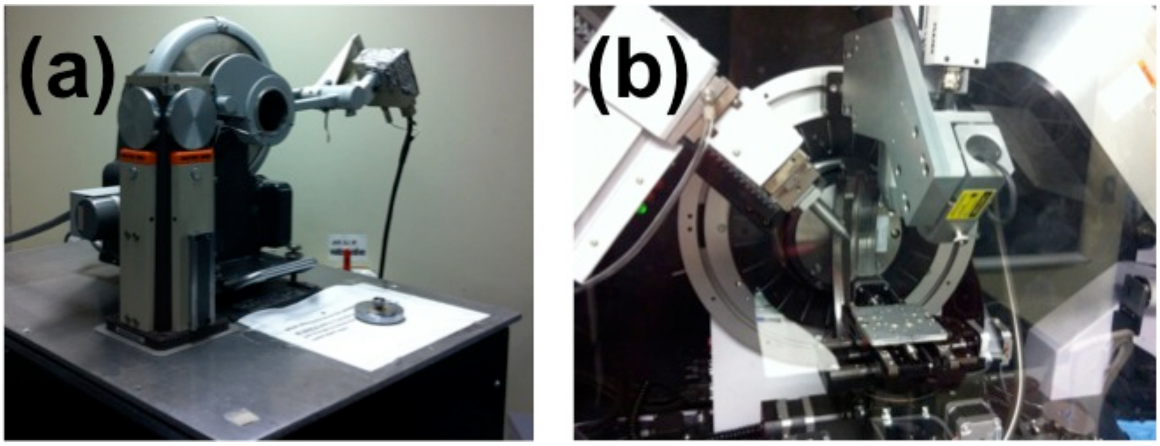

Figure 3-8- XRD systems employed throughout this study. (a) Phillips PW1070 (b) Bruker D8 Advance

3.11 Cell Width Measurements

Throughout the entire project the cell spacing, or cell width was measured from secondary electron images using the lineal intercept method as stated in ASTM E112-96 [2].

3.12 Hardness Testing

Age hardening experiments were performed with and without the inclusion of a pre-aging solutionizing heat-treatment. The solutionizing heat-treatment involved 520°C for 2 hours. Artificial aging was then performed at 120°C for 12 hours and 160°C for 24 hours to obtain the peak-aged condition. Hardness measurements were performed using a Clark Microhardness CM-100AT (see Figure 3-9). A 100g –force applied load was used for the CSC-MIG and ESD samples, while a 10g-force load was applied during the indentation of the LRM samples.

Figure 3-9- Clark micro-Vickers indenter.

3.13 References

[1] Rupp B. XLAT Cell Parameter Refinement. vol. 2012. http://www.ruppweb.org: Life Science Discoveries Inc., 2005.

[2] ASTM. E-112-96 Standard Test Methods for Determining Average Grain Size. West Conshohocken, PA: ASTM International, 2004.

4 Microstructural investigation of a Controlled-Short-Circuiting Metal-Inert-Gas deposited Aluminum-Lithium alloy.[1]

4.1 Preface

As the Controlled-Short-Circuiting Metal-Inert-Gas welding process has been shown to involve very low heat-inputs during deposition with respect to other GMAW processes, it is postulated that solidification will result in refinement of the microstructure and ultimately a reduction in micro-segregation. Furthermore, of all the RSP techniques investigated within this project, the CSC-MIG process is capable of the highest deposition rates, and therefore able to produce larger components during SFF. As the CSC-MIG process is relatively new and unknown, it was selected for study, as it was believed that the determination of the solidification behavior of the CSC-MIG deposited material would be a significant contribution to the welding and SFF communities.

4.2 Abstract

Controlled-Short-Circuiting Metal-Inert-Gas (CSC-MIG) welding was investigated as a potential Solid Freeform Fabrication (SFF) process for AA2199. The low heat input of the CSC-MIG process combined with the high thermal conductivity of the aluminum alloy workpiece resulted in a cooling-rate on the order of 840 - 3500 °C/s being realised during deposition. The solidification time was then calculated using Rosenthal's 3-dimensional heat-flow equations, and determined to range between 2-5ms depending on the location within the weldment. The deposited material displayed a fine (4.3 ±1 μm) cellular structure, comparable to that previously reported for electron beam welding. Through comparison with the Kurz-Giovanola-Trivedi (KGT) model for microstructural development during solidification, the solidification front velocity (SFV) of the CSC-MIG process was estimated to be ~2-4.5x10^{-4}m/s. Chemical analysis via EDS and TOF-

---

[1] To be submitted to The Journal of Science and Technology of Welding and Joining

SIMS revealed lateral segregation of copper to the cell walls, and a similar segregation profile to that predicted by the Clyne-Kurz model. TOF-SIMS revealed a homogeneous lateral lithium distribution, however depth profiling displayed some extent of lithium enrichment at the surface of the deposited material. This is believed to have occurred due to the high diffusivity of lithium within aluminum during solidification.

4.3 Introduction

Aluminum-lithium (Al-Li) alloys have long been studied for use within aerospace and aeronautical applications, due to their high-strength and low density[1]. Lithium is the lightest known metallic element (density = 0.534g/cc), and the only metal (other than beryllium) that increases the elastic modulus of aluminum when alloyed, while reducing the density [2]. The addition of 1 weight percent lithium to aluminum results in an ~3% decrease in density, and a ~6% increase Young's Modulus [3]. Early Al-Li alloys suffered from several issues such as anisotropy of mechanical properties and poor toughness [1]. However, a resurgence in the area of Al-Li alloy development has resulted in the production of third generation Al-Li alloys with improved mechanical behaviour, such as the AA2199 alloy developed by Alcoa [4]. A potential limitation to widespread implementation of Al-Li alloys is the difficulties associated with fusion welding processes. As the transition from traditional mechanical joints such as riveting or fasteners to that of welded joints offers aerospace manufacturers further methods of reducing vehicle weight [5]. Thus, the development of a process capable of producing high-quality Al-Li welds is of interest. Furthermore, recent developments in Solid Freeform Fabrication (SFF) or additive manufacturing techniques based on gas-metal-arc-welding (GMAW) offer the opportunity to directly form components in a near-net-shape process. Such processes allow manufactures to improve the buy-to-fly ratio, and therefore may increase the economics of using an Al-Li alloy [6]. SFF via GMAW processes have previously been employed for various alloy systems [7-10]. It has been determined that in order to ensure adequate mechanical properties of SFF-GMAW components are achieved, control over the solidification behavior (morphology, compositional homogeneity) during the deposition of the material is of utmost importance.

While investigations involving the GMAW of 1st and 2nd generation Al-Li alloys have been performed [11, 12], studies involving the 3rd generation alloys, typically aluminum-lithium-copper alloys (Al-Li-Cu), have mainly focused on non-fusion welding processes such as friction-stir-welding [5, 13-18].

From a solidification standpoint, the processing of Al-Li alloys involves the application of specialized equipment to ensure a proper atmosphere, as the high reactivity of lithium may result in lithium loss to the surrounding environment during solidification [19]. Additionally, copper and lithium tend to segregate during solidification as the equilibrium partition coefficient (k_{eq}) of these solute elements within aluminum is less than one (k_{eq}^{Cu}=0.15, k_{eq}^{Li}=0.55). As such these alloys are normally subjected to a subsequent thermo-mechanical processing (TMP) to chemically homogenize the solidified material [20]. As performing TMP would negate the advantages of near-net-shape processing, removing the necessity of this step is of paramount importance. A potential method to circumnavigate the necessity of TMP would be to solidify the material in a method in which a minimal extent of solute segregation occurs. Rapid solidification processing (RSP) has been shown to reduce the extent of, or completely prevent microsegregation from occurring during solidification [21]. As solute segregation is a diffusion-based process, minimization of the heat-input, as well as the solidification time (t_f) should reduce the effect of microsegregation during deposition solidification.

The Controlled-Short-Circuiting Metal-Inert-Gas (CSC-MIG) welding process combines pulsed and short-circuit GMAW (GMAW-P/GMAW-S) technologies in a novel low heat-input hybrid process[22, 23]. The CSC-MIG process allows for increased material transfer at a lower heat-input. It is postulated that the reduced heat-input of the CSC-MIG process may prevent excessive diffusion of solute within the solid phase, and thereby reduce the extent of solute segregation that occurs during solidification.

This study investigates the effect of the low heat-input CSC-MIG process on the solidification behaviour of deposited bead-on-plate weldments of AA2199 for SFF applications.

4.4 Experimental Procedure

The composition of the Alcoa developed AA2199 alloy used throughout this study is displayed in Table 4-1.

Table 4-1- Composition of AA2199 in atomic percentage.

Element	Al	Li	Cu	Zn	Mg	Mn	Zr	Fe	Si
[at.%]	Bal.	5.3-6.8	1.0-1.2	0.1-0.4	0.05-0.4	0.1-0.5	0.1-0.4	0.03max	0.05max

The alloy was deposited in a bead-on-plate manner via the application of a JetLine Engineering Controlled-Short-Circuiting Metal-Inert-Gas (CSC-MIG) welding machine. The CSC-MIG was mounted on a Machitech XYZ automated table controlled using DeskCNC software. The welding parameters used throughout the entirety of this study are displayed in Table 4-2. Welding trials were performed upon 3.175mm thick rectangular coupons of aluminum alloy 6061 with the dimensions 100 by 38 mm with a welder travel speed of ~17mm/s. This coupon geometry was selected due to a desirable temperature distribution as predicted by two-dimensional heat-flow modeling results, therefore allowing for weld-to-weld comparison.

Table 4-2 - CSC-MIG welding parameters used throughout this study.

Current Parameters	
Arc Current Baseline 1	60A
Arc Current Peak	90A
Arc Current Baseline 2	60A
Short Current Baseline 1	60A
Short Current Peak	60A
Short Current Baseline 2	60A
Current Rise/Fall Rate	200A/ms
Wire Feed Parameters	
Wire Feed Speed Down	5m/min
Delay Before Wire Down	9ms
Wire Feed Speed Up 1	4m/min
Delay Before Wire Up	9ms
Wire Feed Speed Up 2	9m/min
Arc Length	0.5mm
Penetration Delay	0.6ms

Real-time welding waveform signatures were acquired through the application of an Impact Welding Arc Agent 3000P weld monitoring system. The heat-input of each individual weld was calculated in-situ using the Arc Agent software package.

Microscopy analysis was performed using Hitachi SU-8000 and Hitachi S-4700 Scanning Electron Microscopes (SEM). Energy Dispersive Spectroscopy (EDS) was performed using a Phillips XL30 SEM. Semi-quantitative analysis was performed by collecting spectra of pure aluminum and copper standards and using the DTSA-II Fornax software package to compare the known and unknown spectra. Time-of-Flight Secondary-Ion-Mass-Spectroscopy (TOF-SIMS) analysis was employed through the application of an IONTOF TOF-SIMS IV in both negative and positive ion detection modes. Surface mapping and depth profiling were performed on the same TOF-SIMS instrument. To estimate the milling rate of the depth profiling the experiments were repeated using the same etching parameters on a Ta_2O_5/Ta standard, and the resultant depth was then measured with an Atomic Force Microscope (AFM).

4.5 Results

4.5.1 Microstructural Analysis

The resulting solidification microstructure of the CSC-MIG deposited material is displayed in Figure 4-1. The figure displays a fine cellular microstructure consisting of a continuous bright phase forming the cell walls within the as-deposited AA2199. The average cell width as determined using the lineal intercept method, as stated in ASTM E112-96, is ~4.3 ±1 μm. Some globular precipitates are noted within the cells, while larger globules decorate the cell walls. The cellular morphology noted within the microstructure is the result of the breakdown of a planar interface into that of a cellular one, which occurs when the solidification front velocity (SFV) falls below the critical value required for absolute interfacial stability as predicted by the interfacial stability theory of Mullins and Sekerka [24]. As GMAW involves the deposition of a small amount of liquid metal upon a room-temperature substrate, significant thermal gradients can be developed resulting in high cooling-rates being realised. Furthermore, the novel

CSC-MIG process allows the user to reduce the heat-input substantially, by tailoring the waveform, through the implementation of low-duration high-intensity current pulses. The heat-input for the welds used throughout this study was measured to be on the order of ~59J/mm (~1.5kJ/in).

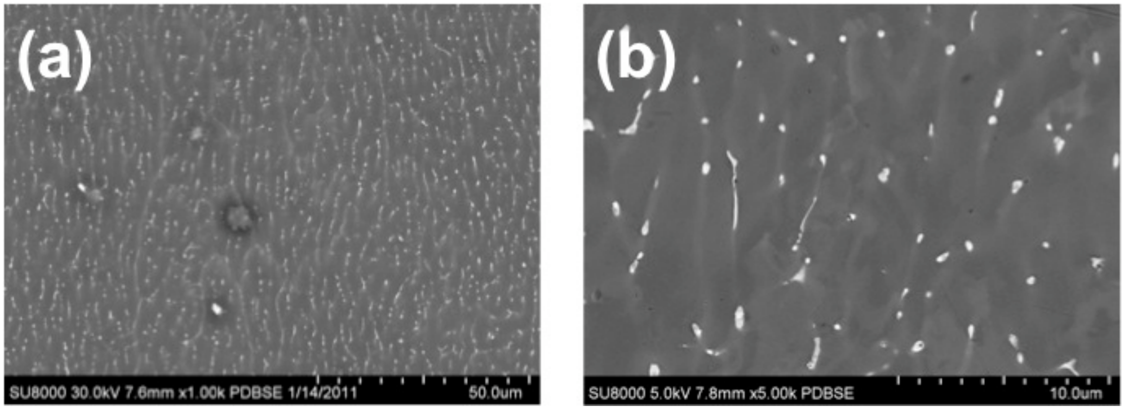

Figure 4-1- SEM image of as-deposited AA2199 material (a) displaying cellular morphology, (b) higher magnification revealing interconnected intra cellular phase.

A cellular structure has been previously reported by studies investigating the weld microstructures obtained during deposition of Al-Cu alloys [25]. As the main alloying element within the AA2199 alloy (in terms of weight percentage) is copper, it is possible to draw a comparison between dendrite arm spacing (DAS) (or cell spacing) and heat-input per unit length data found in literature for binary Al-Cu alloys. The cell size, or primary dendrite arm dendrite spacing as a function of the solidification parameter ($(Q/V)^{1/2}$, where Q is the heat-input and V is the welding speed) previously reported for Al-Cu weldments and is displayed in Figure 4-2 along with that from this study [26, 27]. It can be seen from this plot that the cellular spacing measured within this study fits along the general trend reported by others from measurements within the Al-Cu system. Furthermore, it is noted that the low heat-input of CSC-MIG process resulted in a refinement of the cellular structure. This cell spacing was comparable to that achieved during spray particle deposition by Brown and Adams [26] and by Wanjara and Brochu during electron beam welding [28] and significantly smaller than for the conventional GMAW and GTAW processes.

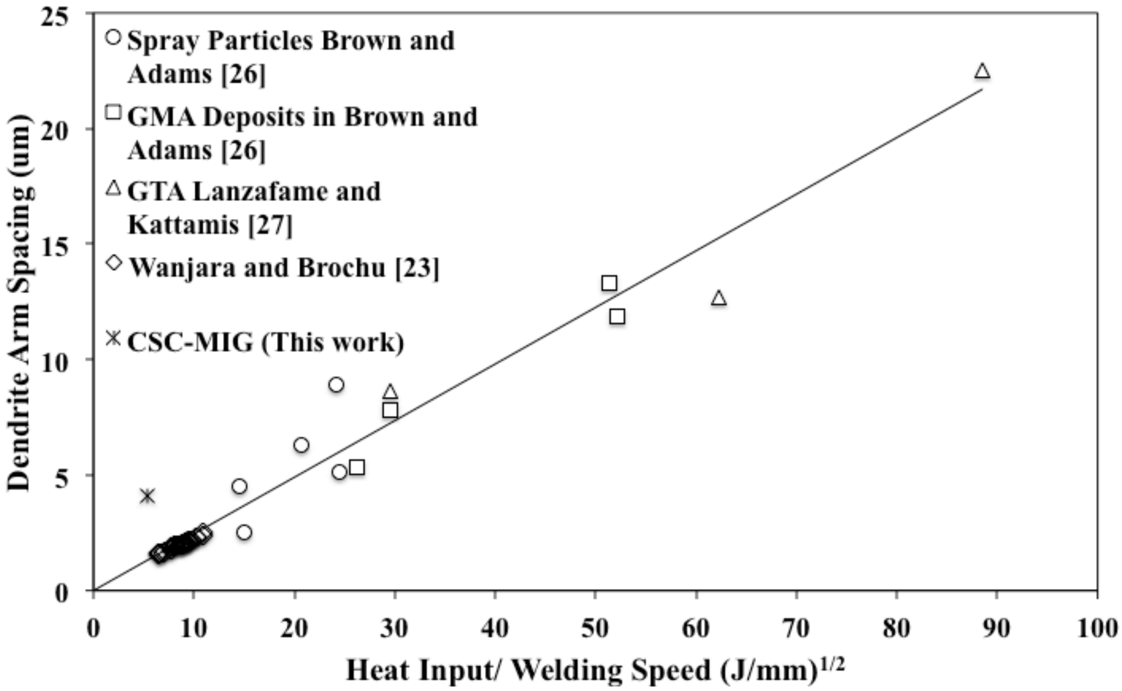

Figure 4-2- Comparison of cell size with that of literature reported values[27, 29].

As the DAS or cell spacing has been shown to be directly related to the cooling-rate realized during solidification, it was then possible to estimate the cooling-rate realized in the deposited AA2199 material through the application of Equation 4-1

$$\lambda = B\left(\frac{\Delta T}{t_s}\right)^{-n} \qquad \text{(Equation 4-1)}$$

where λ is the dendrite arm spacing (or cell spacing), $\Delta T/t_s$ is the cooling-rate, and B and n are material constants. As values of B and n for the AA2199 alloy are not currently available, the values of B and n used during this calculation were 45 ± 10 units of (μm(K/s)^n) and 0.33 (no units) respectively, as determined for an Al-Cu alloy[30]. It was therefore estimated that the cooling-rate realized during CSC-MIG solidification was on the order of 840 -3500 °C/s. This a cooling-rate is comparable to that achieved during the water atomization [31].

The Rosenthal's 3-Dimensional heat-flow equation (see Equation 4-2) was applied to estimate the temperature distribution and the thermal cycle realized at various locations within the deposited material

$$\frac{2\pi(T - T_0)kg}{Q} = exp\left(\frac{-V(R - x)}{2\alpha}\right) \qquad \text{(Equation 4-2)}$$

where T is the temperature at a given location, T_0 is the initial temperature of the workpiece, k is the workpiece thermal conductivity, g is the workpiece thickness, Q is the heat-input of the welder ($Q=EI\eta$, where E is the welder voltage, I is the current, η is the heat-transfer coefficient (0.8 in this case) [29] , V is the travel speed, R is the radial position ($R=(x^2+y^2+z^2)^{1/2}$), x is the position along the weld travel direction, and α is the workpiece thermal diffusivity ($\alpha=k/\rho C$, where ρ is the density and C is the specific heat of the workpiece).

The calculated thermal cycle data for various locations within the deposited material are displayed in Figure 4-3. The two dashed horizontal lines within Figure 4-3 represent the liquidus (upper) and solidus (lower) lines for the AA2199 alloy. These values were calculated through the application of the FactSage thermodynamic modeling software package for the given composition of the alloy.

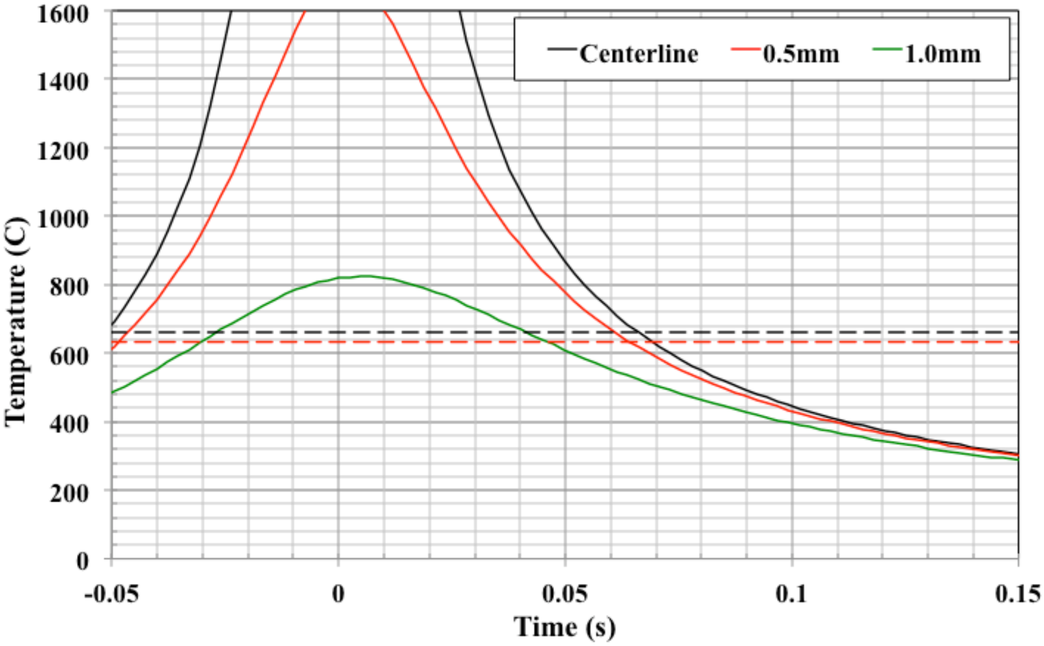

Figure 4-3 - Calculated thermal cycles for various positions within the CSC deposited bead-on-plate weld.

It is noted that as the distance away from the center of the fusion-zone is increased the peak temperature realized is decreased. Furthermore it is noted that the solidification time (t_f) increases with increasing distance from the centerline, as the thermal gradient is lessened. At the centerline the solidification time is on the order of 2ms, while 1mm away from the centerline, the solidification time has increased to approximately 5ms. This short solidification time is the result of the low heat-input of the CSC-MIG process, as it is significantly less than that reported by Huang and Kou for GMAW of the similar AA2219 alloy [25].

It is therefore postulated that the cellular structure formed within the CSC-MIG solidified material was the result of the high cooling rate and low solidification time realized. The formation of a cellular morphology is the result of the de-stabilization of a planar solid-liquid interface via the formation of perturbations, which ultimately become the dendrite tips. While a stable planar interface is traditionally thought of as a low growth rate (or low solidification front velocity (SFV)) phenomenon, Coriell and Sekerka have shown how stabilization may also occur at high growth rates [32]. This stabilization phenomenon has been described by Mullins and Sekerka, who have developed a theory for the absolute stability of a planar interface during solidification [24]. After later modification of the model by Coriell and Sekerka, the theory has been shown to be applicable at both high and low SFV values [32]. The model allows one to calculate the SFV required for absolute stability of a planar interface within a given material during solidification. It was determined using the Mullins and Sekerka model, that for the AA2199 system a SFV of ~1m/s is required to stabilize a planar solid-liquid interface within the high growth rate regime. As a SFV on the order of 1m/s is quite high, and typically induced within processes such as melt spinning [33], Electrospark deposition[34], or laser melting [35] , it is not expected to be obtainable within the CSC-MIG system. However, as the spacing of the cellular morphology formed during solidification is decreased with an increase in SFV, the refinement of the cellular spacing formed within the CSC-MIG samples with respect to other GMAW processes is indicative of a relatively high SFV occurring.

To estimate the SFV realized during CSC-MIG solidification, the Kurz-Giovanola-Trivedi (KGT) model for microstructural development during rapid solidification was applied. The KGT model predicts the dendrite tip radius formed during solidification as a function of the SFV through the solution of Equations 4-3 to 4-8 [36].

$$V^2A + VB + C = 0 \qquad \text{(Equation 4-3)}$$

$$A = \frac{\pi^2\Gamma}{P^2D^2} \qquad \text{(Equation 4-4)}$$

$$B = \frac{mC_0(1-k)\xi_c}{D[1-(1-k)\mathrm{Iv}(P)]} \qquad \text{(Equation 4-5)}$$

$$C = G \qquad \text{(Equation 4-6)}$$

Where V is the SFV, Γ is the Gibbs-Thompson coefficient, m is the slope of the liquidus line of the phase-diagram, P is the Péclet number, k is the equilibrium partition coefficient, D is the liquid interdiffusion coefficient, Iv(P) is the Ivanstov's solution, G is the mean temperature gradient at the solid-liquid interface, and:

$$\xi_c = 1 - \frac{2k}{\left[1 + \left(\frac{2}{P}\right)^2\right] - 1 + 2k} \qquad \text{(Equation 4-7)}$$

The dendrite tip radius as a function of SFV can then be calculated through the application of Equation 4-8.

$$R = 2\pi \left[\frac{\Gamma}{mG_c\xi_c - G}\right]^{1/2} \qquad \text{(Equation 4-8)}$$

Where R is the dendrite tip radius, and G_c is the concentration gradient of the solute at the solid-liquid interface.

In an attempt to estimate the SFV realized during solidification of the CSC-MIG deposited material, the cell width determined from the microstructural analysis was compared with the microstructural morphology predicted by the KGT model. The SFV required to produce the 4.3 ±1 μm wide cells (or an ~2 μm dendrite tip radius) present within the CSC-MIG deposited material is estimated to be ~2-4.5x10^{-4}m/s. This calculated SFV is two orders of magnitude higher than that estimated by Haung and Kou [25] via constitutional supercooling theory (CST) for the GMAW of AA2219, and agrees with the solidification time (t_f) predicted from the calculated thermal cycles.

While a SFV of 2-4.5x10^{-4}m/s is significantly faster than that of traditional ingot-based solidification, the Continuous Growth Model (CGM) for solute trapping during solidification [37, 38], as developed by Aziz, does not predict a deviation from equilibrium partitioning for copper or lithium within aluminum until a SFV ≥2x10^{-2}m/s is achieved. Therefore the solute-trapping phenomenon is not expected to occur during CSC-MIG solidification. Furthermore, Bolling and Tiller have shown that a cellular structure is stabilized via the lateral diffusion of solute from the tip of the cell to the side walls resulting in the solidification of a solute rich inter-cellular phase [39]. In fact, the atomic number contrast within back-scattered electron image present in Figure 4-1, shows that the cell walls are significantly higher in copper concentration than the cell centers.

4.5.2 Segregation Analysis

As equilibrium partitioning of the AA2199 material would result in significant solute enrichment at grain boundaries as well as along the solidification direction, it was of interest to map the solute distribution throughout the microstructure. Therefore an EDS elemental map of the cellular microstructure formed during CSC-MIG deposition of AA2199 was performed to determine the copper distribution within the solidified material. Figure 4-4 displays the area analyzed as well as the resulting EDS maps for Al and Cu, and the resulting EDS spectra from a line-scan across a cell wall displaying the copper enrichment.

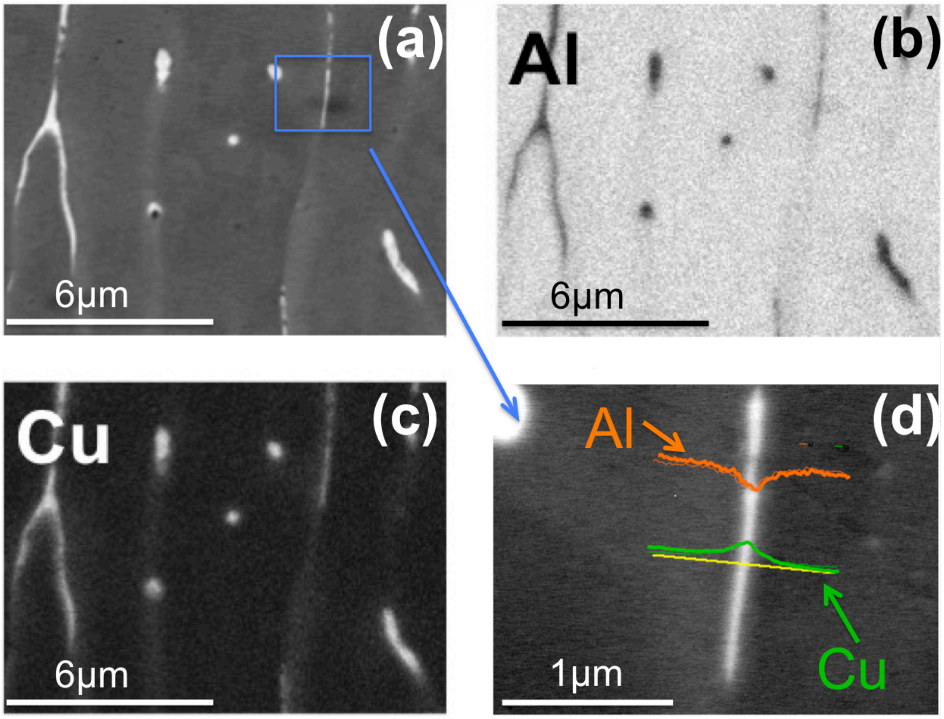

Figure 4-4-(a) Electron image (b) EDS map of Al, (c) EDS map of Cu, (d) Line-scan across a cell wall.

The EDS map and line-scan analysis revealed the presence of a copper rich phase between the cells. This is indicative of significant solute segregation occurring during solidification. The equilibrium partition coefficient of copper within aluminum is approximately 0.15 [40] (k_{eq}^{Cu}=0.15) and therefore significant segregation during solidification is to be expected. This copper rich inter-cellular phase is expected to be the ternary T_2 phase (Al_6CuLi_3) as predicted by FactSage. A study by Chen et al. on the solidification path of a similar composition Al-9.0Li-1.0Cu alloy (atomic percent) also predicted the formation of the T_2 phase [41].

To gain a further understanding of the extent of solute segregation occurring during CSC-MIG solidification, a modified version of the Scheil segregation model was applied. Clyne and Kurz have modified the Scheil cooling model to predict solute distribution across a cell or dendrite to include back diffusion within the solid phase [42]. The Clyne-Kurz model predicts the solute content at the solid-liquid interface as a function of solid fraction through the application of Equations 4-9 to 4-11.

$$C_s' = kC_0\{1-(1-2\Omega k)f_s\}^{(k-1)/(1-2\Omega k)} \qquad \text{(Equation 4-9)}$$

$$\Omega(\alpha) = \alpha\left(1-exp\left(-\frac{1}{\alpha}\right)\right)-\frac{1}{2}exp\left(-\frac{1}{2\alpha}\right) \qquad \text{(Equation 4-10)}$$

$$\alpha = \frac{4D_s t_f}{\lambda^2} \qquad \text{(Equation 4-11)}$$

Where C_s' is the concentration of solute within the solidified solid, k is the equilibrium partition coefficient, C_0 is the initial composition of the melt, f_s is the solid fraction, D_s is the diffusivity in the solid phase, t_f is the solidification time, and λ is the cell-spacing.

Quantitative EDS was then performed and spectra were acquired across a cell and through the cell wall. The resulting solute profile is displayed in Figure 4-5 along with that predicted via the lever rule and the Clyne-Kurz model. It should be noted that both the lever rule and Clyne-Kurz model calculate the solute composition at the progressing solid-liquid interface, and as some level of back diffusion within the solid is expected, the final solute profile may differ from the interface composition profile.

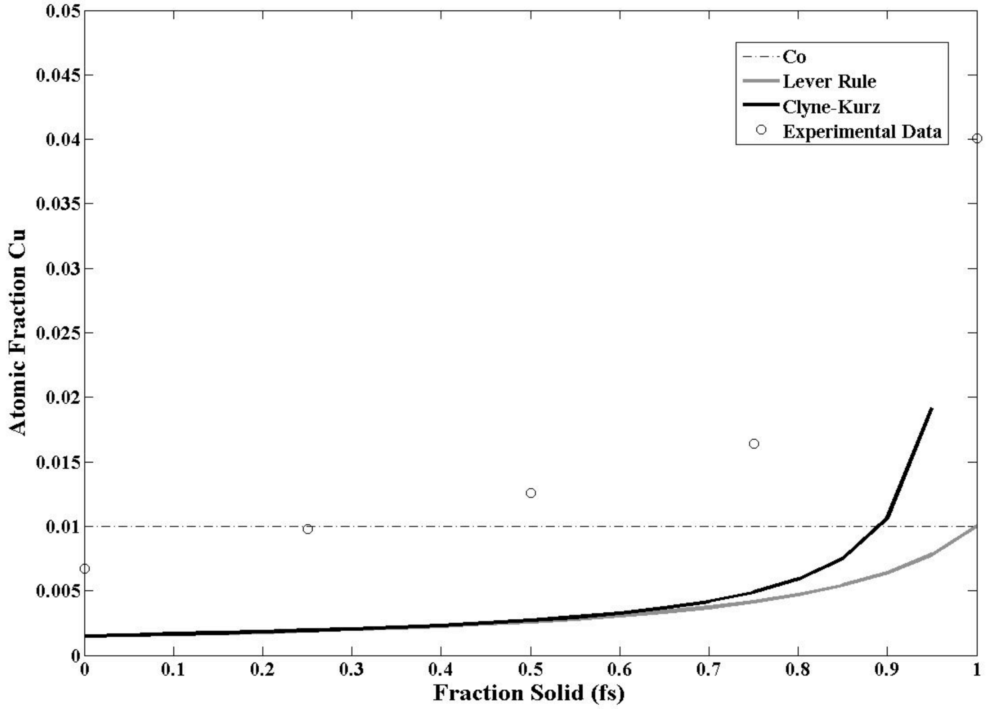

Figure 4-5- Quantitative EDS data displaying the copper concentration profile across a cell compared to that predicted by Lever Rule and Clyne-Kurz.

Figure 4-5 shows that the general trend of the solute profile matches that predicted by the Clyne-Kurz model, however the composition varies significantly. It is noted that the initial composition, corresponding to the cell center, is significantly greater than that to be expected by theory ($k_{eq}C_0$). This phenomenon has been previously reported in a study of solute profiles within Gas-Tungsten-Arc-Welding (GTAW) Al-Cu weldments performed by Norman et al. [43]. The authors stated that this dendrite/cell core enrichment in copper was the result of solute enrichment at the tip of the cell due to a high level of undercooling induced by the relatively high SFV of the GTAW welding process. As the SFV estimated for the CSC-MIG process is greater than that for the GTAW process, it is postulated that a similar phenomenon is occurring, resulting in the enrichment of copper within the cell cores. Given that the core concentration is enriched, it is still noted that the segregation profile is closer to that of the Clyne-Kurz model than that of the lever rule. It is therefore postulated that while back diffusion within the solid occurs during CSC-MIG solidification, the extent is limited.

As the limitations of EDS systems prevent the analysis of lithium distribution, TOF-SIMS mapping and depth profiling was applied. Figure 4-6 displays the resultant TOF-SIMS map of the CSC-MIG deposited material. It is evident from the resulting elemental maps that significant local copper enrichment is occurrs, while the lithium distribution is much more homogeneous. This is to be expected as the equilibrium partition coefficient of copper within aluminum is significantly less than that of lithium within aluminum, k_{eq}^{Cu}=0.15, k_{eq}^{Li}=0.55.

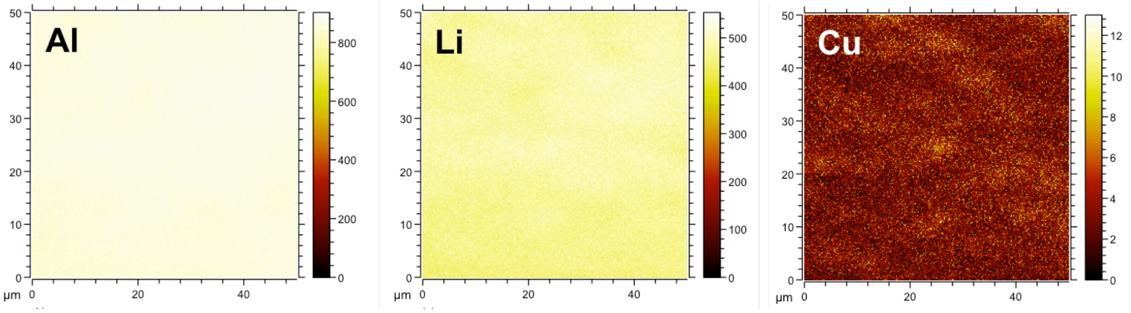

Figure 4-6- TOF-SIMS chemical mapping of Al, Li, and Cu distribution within CSC-MIG deposited AA2199 material.

As the spatial resolution of the TOF-SIMS instrument is on the order of 100nm, the mapping suggests that copper alone is segregating towards the cell boundaries. It should be noted that the size of the lithium bearing precipitates that are expected to form within this system are on the order of <100nm [44], therefore these precipitates would not be visible via the TOF-SIMS technique. As the solidification during welding can be thought of as directional solidification from the substrate, TOF-SIMS depth profile analysis was performed to determine if there was any solute segregation along the solidification direction. The depth profile analysis along the solidification direction is displayed in Figure 4-7. The depth profile data for lithium and the most common lithium isotope (^{6}Li) as well as aluminum displayed a slight lithium enrichment at the surface. This is believed to be due to the high diffusivity of lithium within aluminum and is supported by a previous study by Papazian et al. who has shown that the high lithium diffusivity in AA8090 and AA8091 during heat-treatment resulted in rapid diffusion of lithium to the surface where ultimately the lithium was lost to atmosphere via reaction with hydrogen and oxygen [45]. The analysis of copper and the most common copper isotope (Cu^{65}) (not shown) did not reveal significant surface enrichment.

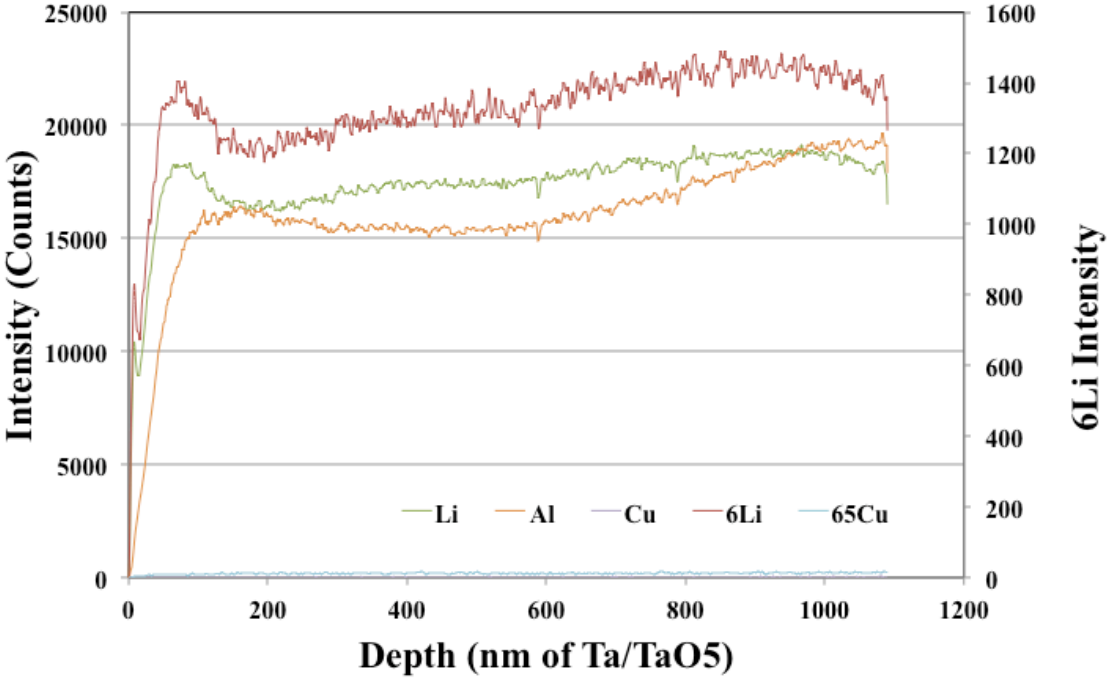

Figure 4-7- TOF-SIMS depth profile of CSC-MIG deposited AA2199 material.

The homogeneous lithium distribution reveals a significant improvement over previous welding studies of lithium bearing alloys, where significant lithium depletion within the weld-zone was noted [19].

4.6 Conclusions

It was determined that the low heat-input of the CSC-MIG process combined with the high thermal conductivity of the aluminum alloy workpiece resulted in a high cooling-rate during deposition on the order of 840 -3500 °C/s being realized. The solidification time was then calculated using Rosenthal's 3-dimensional heat-flow equations, and determined to range between 2-5ms depending on the location within the weldment. This resulted in the formation of a fine (4.3 ±1 μm) cellular structure within the deposited material. Through comparison with the KGT model for microstructural development during solidification the SFV of the CSC-MIG process was estimated to be $\sim 2\text{-}4.5\text{x}10^{-4}$m/s. Chemical analysis via EDS and TOF-SIMS revealed lateral segregation of copper to the cell walls, and a similar segregation profile to that predicted by the Clyne-Kurz model. TOF-SIMS revealed a homogeneous lateral lithium distribution, however depth profiling displayed some extent of lithium enrichment at the surface of the deposited material. This is believed to have occurred due to the high diffusivity of lithium within aluminum during solidification.

4.7 Acknowledgments

The authors would like to acknowledge the support of the Natural Science and Engineering Research Council of Canada (NSERC), the McGill University Engineering Doctoral Award (MEDA) as well as that from the Regroupement Aluminum Research Centre (REGAL). The authors would also like to acknowledge the technical assistant of Mr. Nicolas Brodusch and Ms. Suzie Poulin.

4.8 References

[1] Rioja R, Liu J. The Evolution of Al-Li Base Products for Aerospace and Space Applications. Metallurgical and Materials Transactions A 2012:1.

[2] Martin JW. Aluminum-Lithium Alloys. Annual Review of Materials Science 1988;18:101.

[3] Lavernia EJ, Grant NJ. Aluminium-lithium alloys. Journal of Materials Science 1987;22:1521.

[4] Giummarra C, Thomas B, Rioja RJ. NEW ALUMINUM LITHIUM ALLOYS FOR AEROSPACE APPLICATIONS. Proceedings of the Light Metals Technology Conference 2007 2007.

[5] Steuwer A, Dumont M, Altenkirch J, Birosca S, Deschamps A, Prangnell PB, Withers PJ. A combined approach to microstructure mapping of an Al–Li AA2199 friction stir weld. Acta Materialia 2011;59:3002.

[6] Almeida PMS, Williams S. Innovative process model of Ti-6Al-4V additive later manufacturing using cold metal transfer (CMT). Solid freeform fabrication symposium, 2010.

[7] Jandric Z, Labudovic M, Kovacevic R. Effect of heat sink on microstructure of three-dimensional parts built by welding-based deposition. International Journal of Machine Tools and Manufacture 2004;44:785.

[8] Siminski MR, De Boer FG. Build Strategies for Rapid Prototyping and Wear Replacement by Gas Metal Arc Welding. WTIA 49th Annual Conference. Adelaide, Australia: Welding Technology Institute of Australia, 2001.

[9] Siminski MR, De Boer FG. Weld Path Generation for Rapid Prototyping and Wear Replacement by Robotic Gas Metal Arc Welding. WTIA 50th Annual Conference. Sydney Australia, 2002.

[10] Wang H, Jiang W, Ouyang J, Kovacevic R. Rapid prototyping of 4043 Al-alloy parts by VP-GTAW. Journal of Materials Processing Technology 2004;148:93.

[11] Pickens JR. The weldability of lithium-containing aluminium alloys. Journal of Materials Science 1985;20:4247.

[12] Pickens JR. Recent developments in the weldability of lithium-containing aluminium alloys. Journal of Materials Science 1990;25:3035.

[13] Schneider JA, Nunes AC, Jr., Chen PS, Steele G. TEM study of the FSW nugget in AA2195-T81. Journal of Materials Science 2005;40:4341.

[14] Seidel TU, Reynolds AP. Visualization of the material flow in AA2195 friction-stir welds using a marker insert technique. Metallurgical and Materials Transactions A 2001;32:2879.

[15] Bitondo C, Prisco U, Squilace A, Buonadonna P, Dionoro G. Friction-stir welding of AA 2198 butt joints: mechanical characterization of the process and of the welds through DOE analysis. Int J Adv Manuf Technol 2011;53:505.

[16] Altenkirch J, Steuwer A, Withers PJ. Process-microstructure-property correlations in Al-Li AA2199 friction stir welds. Science & Technology of Welding & Joining 2010;15:522.

[17] Cavaliere P, Cabibbo M, Panella F, Squillace A. 2198 Al–Li plates joined by Friction Stir Welding: Mechanical and microstructural behavior. Materials & Design 2009;30:3622.

[18] Cavaliere P, De Santis A, Panella F, Squillace A. Effect of anisotropy on fatigue properties of 2198 Al–Li plates joined by friction stir welding. Engineering Failure Analysis 2009;16:1856.

[19] Berzina IG, Gusev EB, Ivanov VA, Lukin VI. Investigation of Li distribution in aluminium alloy welds by elemental radiographic analysis. International Journal of Radiation Applications and Instrumentation. Part D. Nuclear Tracks and Radiation Measurements 1992;20:261.

[20] Rezaei A, Ahmadi S, Shokunfar A, Foroutan I. Investigation of Homogenization Treatment in Al-Li-Cu-Zr Alloys. Defect and Diffusion Forum 2008;273-276:536.

[21] Bolling GF, Tiller WA. Growth from the Melt. I. Influence of Surface Intersections in Pure Metals. Journal of Applied Physics 1960;31:1345.

[22] Huismann G, Hoffmeister H. Control of Short Circuiting in MIG-Process Under Hyperbaric Conditions. Offshore Mechanics and Artic Engineering. Libson, Portugal, 1998.

[23] Huismann G. Direct Control of the Material Transfer: The Controlled Short Circuiting (CSC)-MIG Process. ICAWT 2000: Gas Metal Arc Welding for the 21st Century. Orlando, Florida, 2000.

[24] Mullins WW, Sekerka RF. Stability of a Planar Interface During Solidification of a Dilute Binary Alloy. Journal of Applied Physics 1964;35:444.

[25] Huang C, Kou S. Partially Melted Zone in Aluminum Welds - PLanar and Cellular Solidification. Welding Research Supplement 2001;February:46.

[26] Brown PE, Adams CMJ. Fusion-Zone Structures and Properties in Aluminum Alloys. Welding Journal 1960;39:520.

[27] Lanzafame JN, Kattamis TZ. Solidification Structure and Tensile Properties of 2014 Aluminum Alloy Welds. Welding Journal 1973;52:226.

[28] Wanjara P, Brochu M. Characterization of electron beam welded AA2024. Vacuum 2010;85:268.

[29] Kou S. Welding Metallurgy. New Jersey: John Wiley & Sons Inc., 2003.

[30] Munitz A. Microstructure of rapidly solidified laser molten AI-4.5 Wt Pct cu surfaces. MTB 1985;16:149.

[31] Lavernia EJ, Ayers JD, Srivatsan TS. Rapid solidification processing with specific application to aluminium alloys. International Materials Reviews 1992;37:1.

[32] Coriell SR, Sekerka RF. In: Mehrabian R, Kear BH, Cohen M, editors. Rapid Solidification Processing Principles and Technologies. 1980. p.35.

[33] Karakˆse E, Karaaslan T, Keskin M, Uzun O. Microstructural evolution and microhardness of a melt-spun Al-6Ni-2Cu-1Si (in wt.%) alloy. Journal of Materials Processing Technology 2008;195:58.

[34] Heard DW, Boselli J, Rioja R, Marquis EA, Gauvin R, Brochu M. Interfacial morphology development and solute trapping behavior during rapid solidification of an Al–Li–Cu alloy. Acta Materialia 2013.

[35] Zimmermann M, Carrard M, Kurz W. Rapid solidification of Al-Cu eutectic alloy by laser remelting. Acta Metallurgica 1989;37:3305.

[36] Kurz W, Giovanola B, Trivedi R. Theory of microstructural development during rapid solidification. Acta Metallurgica 1986;34:823.

[37] Aziz MJ. Model for solute redistribution during rapid solidification. Journal of Applied Physics 1982;53:1158.

[38] Aziz MJ, Kaplan T. Continuous growth model for interface motion during alloy solidification. Acta Metallurgica 1988;36:2335.
[39] Bolling GF, Tiller WA. Growth from the Melt. Part II. Cellular Interface Morphology. Journal of Applied Physics 1960;31:2040.
[40] Murray JL. The aluminium-copper system. International Metals Reviews 1985;30:211.
[41] Chen S-W, Chuang Y-Y, Austin Chang Y, Chu M. Calculation of phase diagrams and solidification paths of Al-rich Al−Li−Cu alloys. Metallurgical and Materials Transactions A 1991;22:2837.
[42] Clyne TW, Kurz W. Solute redistribution during solidification with rapid solid state diffusion. MTA 1981;12:965.
[43] Norman AF, Drazhner V, Prangnell PB. Effect of welding parameters on the solidification microstructure of autogenous TIG welds in an Al–Cu–Mg–Mn alloy. Materials Science and Engineering: A 1999;259:53.
[44] Yoshimura R, Konno TJ, Abe E, Hiraga K. Transmission electron microscopy study of the evolution of precipitates in aged Al-Li-Cu alloys: the [theta]' and T1 phases. Acta Materialia 2003;51:4251.
[45] Papazian J, Schulte R, Adler P. Lithium depletion during heat treatment of aluminum-lithium alloys. Metallurgical and Materials Transactions A 1986;17:635.

5 Non-Equilibrium Solute Partitioning in a Laser Re-Melted Al-Li-Cu Alloy[2]

5.1 Preface:

As the SFV realized during CSC-MIG solidification was determined to be below that required for microsegregation free solidification, the lower heat-input LRM process was selected to be studied. The wide-range and high degree of control over the heat-input of the LRM process makes it an ideal candidate for the elucidation of the solidification conditions required to reduce microsegregation within AA2199. Furthermore, the lack of an arc within the LRM process allowed for the isolation of the heat-transfer mechanism variable on the residual lithium content, as to be discussed in Chapter 7.

5.2 Abstract

Aluminum-lithium alloy AA2199 was rapidly solidified through the application of a laser re-melting process to determine the relationship between laser pulse energy and microsegregation during solidification. It was determined that laser pulse energies on the order of 0.125 – 0.5 Joules resulted in a fine cellular solidification structure. Through comparison of the measured cell spacing with that predicted by the Kurz-Giovanola-Trivedi (KGT) model it was possible to estimate that solidification front velocities (SFV) between 3 and 25cm/s were realized during solidification. The SFV calculated from the KGT model was then input within the continuous growth model (CGM) for solute trapping developed by Aziz, to predict the deviation from equilibrium partitioning during solidification for all pulse energy levels employed. The chemical profile of lithium within the re-melted samples was measure using X-ray photoelectron spectroscopy (XPS) and compared with that expected for equilibrium segregation. Measurement of the lattice parameter via X-ray diffraction (XRD) revealed that the solute trapping phenomenon

---

[2] To be submitted to Journal of Applied Physics

resulted in the formation of a super saturated solid solution, as evident through a reduction of the lattice parameter from 4.0485 for the starting material to 4.0399 Å in the material re-melted with a pulse energy of 0.125 Joule.

5.3 Introduction

Recent developments in aluminum-lithium alloys have resulted the development of the 3rd generation of Al-Li alloys, which include copper as an alloying elements, such as the Al-Li-Cu alloy AA2199 developed by Alcoa [1]. The alloying of Al with 1 weight percent lithium results in a 3 percent reduction in density and a 6 percent increase in Young's Modulus of the alloy [2] resulting in a low-density alloy with improved specific strength and stiffness [3]. This unique combination of properties makes Al-Li alloys desirable in applications where a reduction of vehicle weight is of utmost importance such as the aerospace and defense industries [4]. The replacement of traditional aerospace joining processes such as riveting or mechanical fastening by fusion welding processes creates the potential for further vehicle weight reductions [5]. One drawback of aluminum-lithium alloys is the difficulty associated with the fusion welding of the material. The segregation of lithium towards grain boundaries (GB) during traditional (slow) solidification has been shown to result in the formation of lithium bearing precipitates at GB's [6]. These lithium rich precipitates then homogenize the slip during deformation and lower the toughness of the alloy [7-9]. While this segregation may be reversed during casting-house production through thermal-mechanical homogenization (TMH) processes [10, 11], when performing joining processes on large-scale components, in-situ TMH is not always possible. This has resulted in the limitation of widespread implementation of aluminum-lithium alloys in applications in which fusion welding is required.

Rapid solidification processing (RSP) has been previously investigated as a method of circumnavigating the necessity of a TMH process [3, 12]. RSP involves progressing the solidification front velocity (SFV) at high rates and has been shown to result in the formation of non-equilibrium structures, including metastable structures [13, 14], and micro-segregation free solidification [15] via the solute trapping phenomenon [16-19].

The application of a laser beam to induce surface re-melting and ultimately rapid solidification has been employed in various material systems [20-23]. Aziz and Smith have shown that the application of laser re-melting to various dilute aluminum binary alloys (Al-Sn, Al-Cu, Al-Ge, and Al-In), can result deviations from equilibrium partitioning [18, 19]. The authors also reported that the Continuous Growth Model (CGM) for solute trapping can accurately describe this phenomenon in aluminum alloys.

The objective of this study is to investigate the ability of pulsed laser re-melting (LRM) to induce the solute-trapping phenomenon within a commercially available next generation aluminum-lithium alloy (AA2199). Therefore preventing the formation of dendrites or cells which could serve as heterogeneous nucleation sites for the strengthening precipitates such as the T_1 phase (Al_2CuLi) [24].

5.4 Experimental methods

The material that was re-melted during these experiments was an ~3mm thick sheet of AA2199 in the T3 (solution heat-treated and then cold-worked, naturally aged) temper. The composition of the AA2199 alloy used throughout this study is displayed in Table 5-1.

Table 5-1 - Composition of AA2199 used throughout this study (at%).

Element	Al	Li	Cu	Zn	Mg	Mn	Zr	Fe	Si
[at.%]	Bal.	5.3-6.8	1.0-1.2	0.1-0.4	0.05-0.4	0.1-0.5	0.1-0.4	0.03max	0.05max

The as-received AA2199 sheet, was analyzed along side the laser re-melted material, and will be referred to as the "control sample" hereafter.

Laser re-melting was performed using a Miyacki LW25 Nd:YAG (λ=1064nm) pulsed micro-laser welding system, focused on the surface of the AA2199 sheet to be re-melted, resulting in a theoretical spot size of ~150 μm. The laser system was mounted on a

Machitech XYZ automated table, controlled using DeskCNC software. Laser re-melting was performed in an argon environmental chamber. Re-melting was performed on a 12.5 by 7.0 mm area, with a travel speed of ~127 mm/min. The conditions employed to fabricate the LRM samples of AA2199 are displayed in Table 5-2. The heat-input (E) of the pulsed laser was calculated using Equation 5-1.

$$E = \frac{\eta P_{av}}{v} \qquad \text{(Equation 5-1)}$$

Where η is the heat source efficiency (taken in 0.85 in this work) [25], P_{av} is the average power, and v is the travel speed. The average power was calculated by multiplying the pulse energy by pulse frequency.

Table 5-2 - Experimental parameters employed during the laser re-melting trials.

	Condition			
Parameter	**1**	**2**	**3**	**4**
Pulse Energy (J)	0.125	0.25	0.375	0.5
Pulse Duration (ms)	0.5	0.5	0.5	0.5
Pulse Frequency (Pulse/s)	30	30	30	30
Peak Power (W)	250	500	750	1000
Heat-Input (J/mm)	1.51	3.01	4.52	6.02

Scanning Electron Microscopy was performed using a Hitachi SU-8000 and a Phillips XL30 electron microscope. Samples for microscopy analysis were mounted in Bakelite and then ground using 320 grit SiC paper, polishing was then performed using 9, 3, and 1 μm diamond paste, and finished with 0.05μm colloidal silica.

X-ray photoelectron spectroscopy (XPS) was performed using a Thermal Scientific K-Alpha XPS system equipped with Avantage analytical software. Depth profile analysis was completed using an argon ion with an ion energy of 3000eV, resulting in a Ta_20_5 equivalent sputtering rate of ~2.69nm/s. Analysis was performed with a beam spot size of 400μm at 10 depths (surface + 9 subsurface), with 10 seconds of sputtering between analyses.

X-ray diffraction was performed using a Phillips PW1070 diffractometer (Cu Kα λ=1.54056Å). Scans were acquired from 20 to 100 degrees, at a scan rate of 1 degree per second. The lattice parameter was calculated using a silicon reference standard and the XLat analytical software.

5.5 Results

5.5.1 Microstructural Analysis

Microstructural analysis revealed a fine cellular morphology within the laser re-melted AA2199 samples. Furthermore, it was noted that an increase in pulse energy (i.e. heat-input) resulted in a larger cell width. Figure 5-1 displays SEM images of samples produced using (a) 0.5, (b) 0.375, (c) 0.25, and (d) 0.125 Joules per pulse, respectively. As all samples were produced using a constant laser travel speed (~127 mm/min) and spot size (~150 μm), it is evident that as the pulse energy of the laser is reduced, the resulting structure becomes more refined, due to the lower heat-input. The samples re-melted with pulse energies of 0.5 (Fig.5-1(a)) and 0.375 (Fig.5-1(b)) Joules per pulse show similar structural evolutions. Both samples reveal an initial planar growth region followed by a morphological change to a cellular structure. The cellular structure then remains consistent throughout the re-melted and solidified material. The sample re-melted with a pulse energy of 0.25 Joules per pulse (Fig.5-1(c)) reveals an initial epitaxial growth region, before transitioning into a further refined cellular structure. A further decrease in pulse energy to 0.125 Joules per pulse (Fig.5-1(d)) then resulted in featureless solidification.

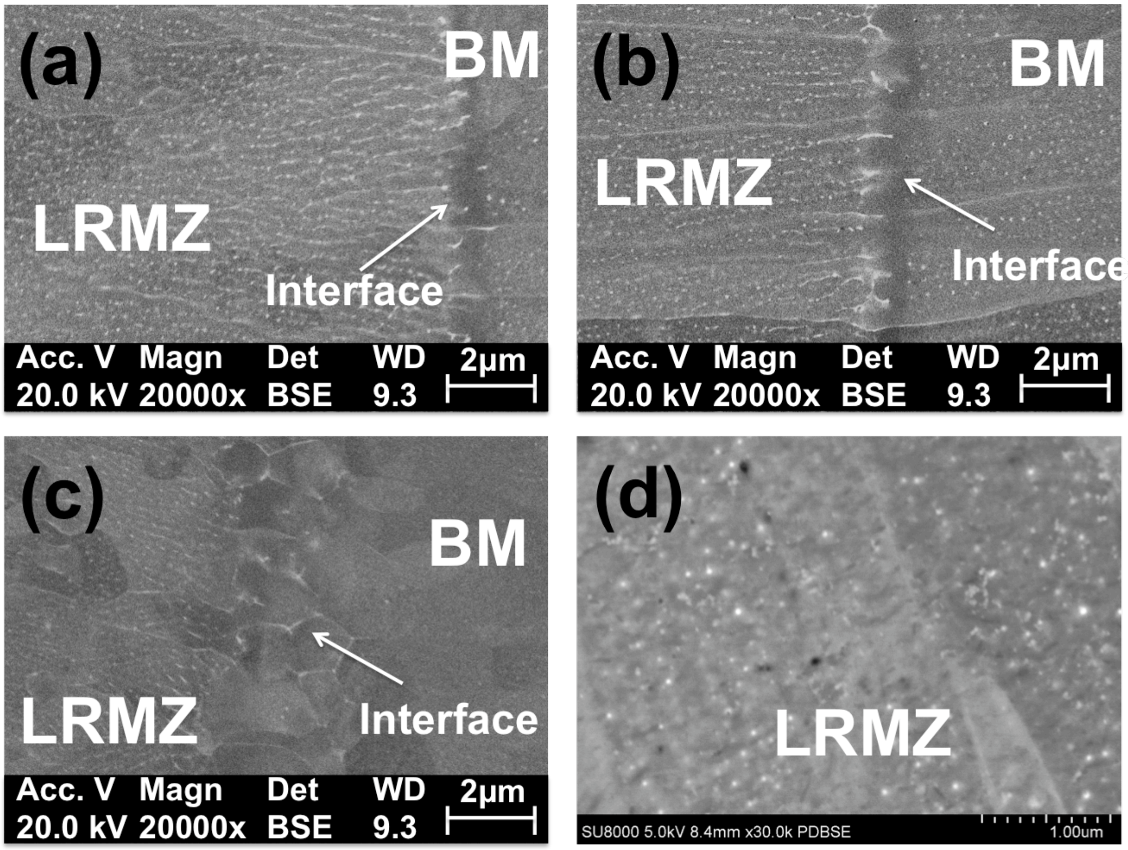

Figure 5-1 - SEM images of as-solidified AA2199 re-melted using various laser pulse energies; (a) 0.5J (b) 0.375J (c) 0.25J (d) 0.125J.

The cellular morphology formed within the samples re-melted with pulse energies of 0.25, 0.375, and 0.5J, is the result the de-stabilization of a planar interface. The development of local perturbations along the solid-liquid interface result in a distortion of the temperature profile along the interface [26], thus resulting in local temperature highs at the peak of a growing cell, and local lows within the troughs. Bolling and Tiller [27] have shown how this cellular interface morphology is then stabilized by the lateral diffusion of solute. The solute is transported from the tip of the growing cell to the troughs, as an increase in solute concentration results in a decrease in equilibrium melting temperature of the alloy, resulting in a heterogeneous solute distribution along the solid-liquid interface [27]. Therefore a cellular morphology is associated with solute microsegregation, as the solute tends to segregates toward the interdendritic region.

A similar morphological development as that reported in this work, was reported by Boettinger et al. who performed electron beam re-melting of Ag-Cu alloys. The authors revealed a breakdown from a planar interface to a cellular morphology when the travel speed was reduced below a critical value [15]. As the SFV induced within the Ag-Cu alloy was shown to be directly related to the travel speed of the continuous electron beam, it was reported that the change in SFV resulted in the de-stabilization of the planar interface.

The absolute stability theory developed Mullins and Sekerka [26] and later refined by Coriell and Sekerka [28], has been demonstrated that a high SFV can stabilize a planar solid-liquid interface during alloy solidification. The resulting interfacial stability theory therefore allows for the prediction of the critical SFV required to stabilize the solid-liquid interface within a specific alloy. The calculated SFV required to stabilize the solid-liquid interface within the AA2199 alloy was then determined to be on the order of ~1m/s, as estimated using the absolute stability theory. The presence of the cellular morphology within the laser re-melted samples is therefore indicative of the realization of a SFV below the critical value required to maintain absolute interface stability.

Based on the theories of interfacial stability by Mullins and Sekerka and non-equilibrium partitioning by Aziz [29], Kurz, Giovanolva, and Trivedi (KGT) developed a model for microstructural development during rapid solidification processing [30]. The KGT model predicts the resulting dendrite arm spacing (or cell width) as a function of the SFV realized during solidification [30]. Through a numerical solution of Equations 5-2 to 5-6 it is possible to calculate the relationship between the Péclet number and the SFV.

$$V^2A + VB + C = 0 \qquad \text{(Equation 5-2)}$$

$$A = \frac{\pi^2\Gamma}{P^2D^2} \qquad \text{(Equation 5-3)}$$

$$B = \frac{mC_0(1-k)\xi_c}{D[1-(1-k)\mathrm{Iv}(P)]} \qquad \text{(Equation 5-4)}$$

$$C = G \qquad \text{(Equation 5-5)}$$

Where *V* is the SFV, *Γ* is the Gibbs-Thompson coefficient, *m* is the slope of the liquidus line of the phase-diagram, *P* is the Péclet number, *k* is the partition coefficient, *D* is the liquid interdiffusion coefficient, Iv(*P*) is the Ivanstov's solution, *G* is the mean temperature gradient at the interface, and:

$$\xi_c = 1 - \frac{2k}{\left[1 + \left(\frac{2}{P}\right)^2\right] - 1 + 2k} \qquad \text{(Equation 5-6)}$$

The dendrite tip radius as a function of SFV can then be calculated through the application of Equation 5-7.

$$R = 2\pi \left[\frac{\Gamma}{mG_c\xi_c - G}\right]^{1/2} \qquad \text{(Equation 5-7)}$$

As displayed in Figure 5-1, decreasing the pulse energy, or heat-input, resulted in a decrease in the SFV realized during solidification, and a coarsening of the cellular structure. Through comparison of the microstructure with that predicted by the KGT model, it was possible to estimate the SFV realised during the re-melting experiments. The cell spacing, measured using the lineal intercept method as stated in ASTM E112-96, and corresponding SFV value estimated through the KGT model are displayed in Figure 5-2.

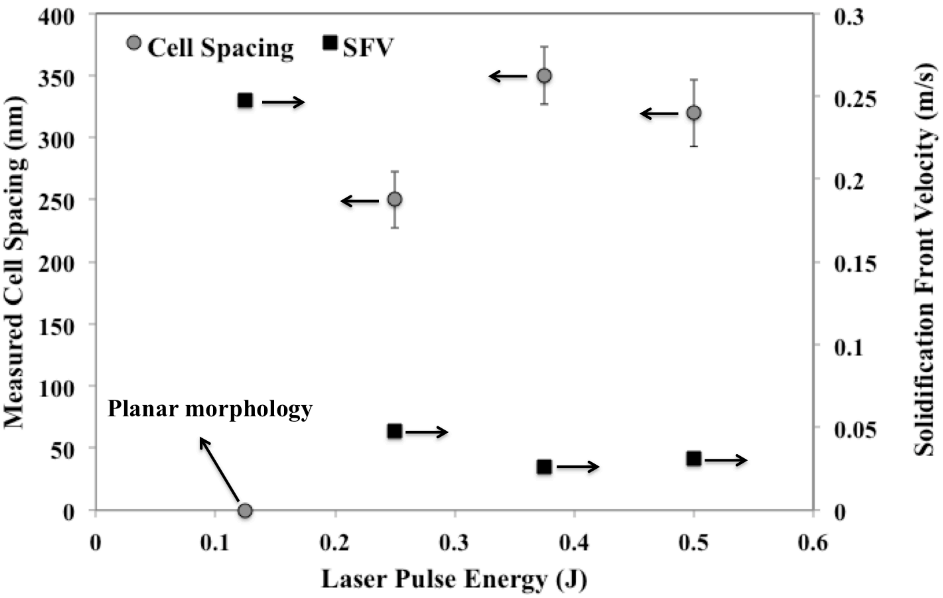

Figure 5-2- The measured cellular spacing and corresponding SFV as a function of laser pulse-energy.

It can be seen that as the pulse energy is increased, the cell spacing is increasing and the SFV is decreasing. The SFV realized throughout the experiments is estimated to range between 3 and 25cm/s depending on the specific laser pulse energy employed. The Continuous Growth Model (CGM) for solute trapping during RSP, as developed by Aziz [29], predicts that for the AA2199 alloy, a SFV ≥1cm/s will result in a deviation from equilibrium segregation. It is then possible to calculate the effective partition coefficient realized during solidification through the application of the CGM for solute trapping using Equation 5-8.

$$k(v) = \frac{\frac{v}{v_D} + k_{eq}}{\frac{v}{v_D} + 1} \qquad \text{(Equation 5-8)}$$

Where k_{eq} is the equilibrium partition coefficient, V is the SFV, and v_D is the diffusive speed. As laser re-melting is analogous to directional solidification, i.e. unidirectional heat-flow and growth, a variation in the partition coefficient realized during solidification will manifest as a difference in solute profile throughout the solidified material. X-ray Photoelectron Spectroscopy (XPS) depth-profiling was performed to determine the solute profile of lithium with respect to depth, within the solidified material, and is displayed in Figure 5-3.

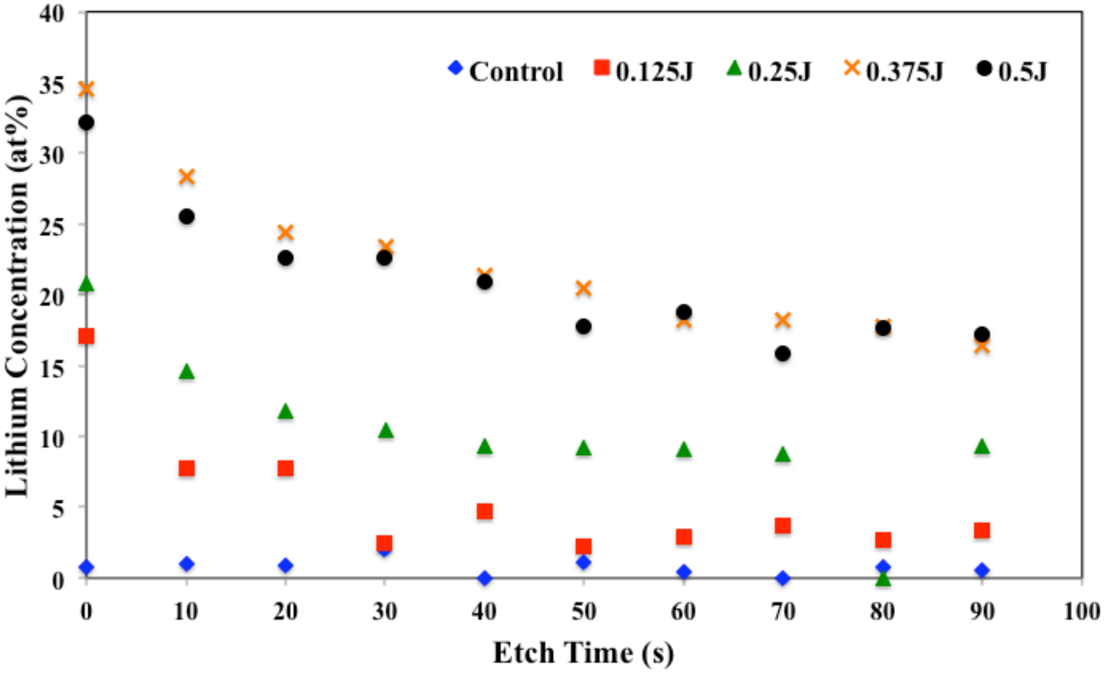

Figure 5-3 - X-Ray Photoelectron Spectroscopy depth profile analysis of RSP AA2199 with various laser energies.

It can be clearly noted from Figure 5-3 that as the pulse energy (heat-input) of the laser is increased the surface becomes more enriched in lithium. As the equilibrium partition coefficient of lithium less than unity (k_{eq}≈0.55), one would therefore expect the liquid phase to become enriched in lithium during solidification, as solute is being rejected from the solid phase to the liquid phase. Therefore the last solid to form (i.e. the surface of the re-melted region) would display an enrichment in lithium content. As the pulse-energy of the laser is decreased, the SFV imparted during solidification increased, and resulted in a higher effective partition coefficient as predicted by the CGM, thus the surface enrichment of lithium is reduced. The lowest investigated heat-input of 0.25J per pulse results in a solute profile that is similar to that of the as-received AA2199 material (control sample). Beyond a 30 second sputter depth (~81nm of Ta_20_5 equivalent) the solute profile of the 0.125J sample and the control sample are comparable. It is important to note that only the first several hundred nanometers of material were analyzed during the XPS depth profiling, while the re-melted zone thickness ranged from ~15 to 50μm depending on the pulse-energy employed. This explains why such significant solute enrichments were noted at higher pulse energies. If in fact solute trapping is being induced during the laser re-melting experiments, then the result should be a super saturated solid solution (SSSS) of aluminum containing lithium and copper. Experiments performed by Zimmermann et al. on an Al-Cu eutectic alloy with heat-inputs between 0.16 and 6.375 J/mm, comparable to that of the present study, revealed SFV values in excess of 50cm/s. These high SFV values resulted in the propagation of a planar solidification front, an increase in the effective partition coefficient and the formation of a SSSS [31]. Therefore the lattice parameter of the re-melted samples was measured via x-ray diffraction and is displayed in Figure 5-4. The x-ray penetration depth was estimated to be a maxima of ~60μm using the AbsorbDX software package (Version 1.1.4). As the thickness of the re-melted material varied from ~15 to 50μm, it must be assumed that some of the substrate (original un-melted) material is being detected during the lattice parameter measurements.

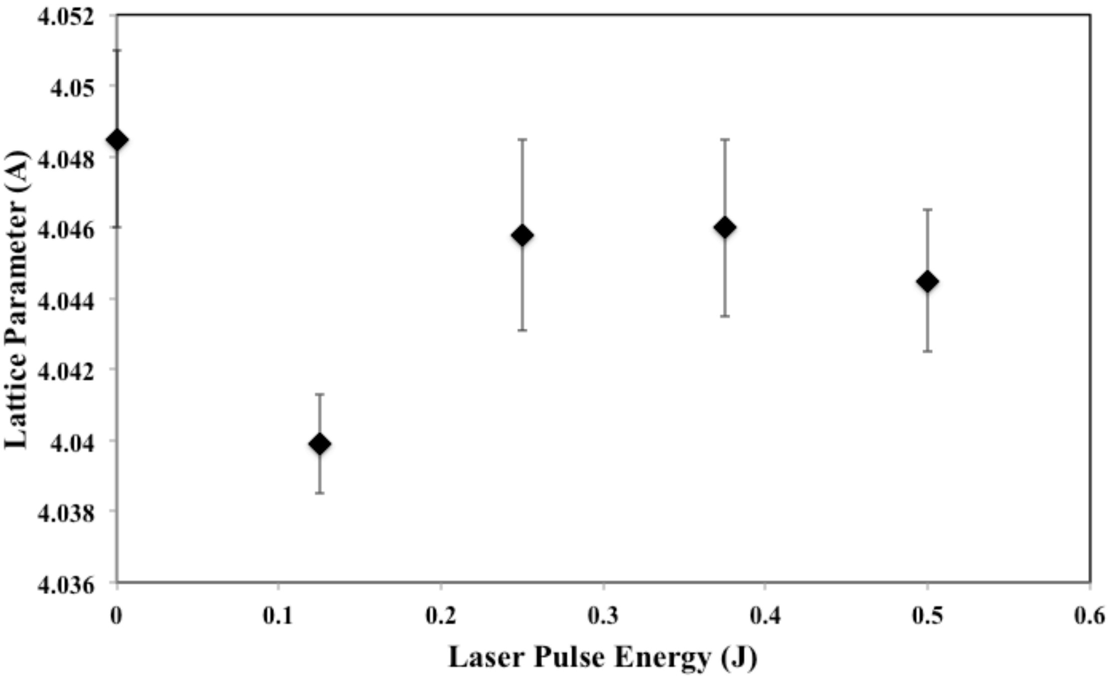

Figure 5-4 - Laser Pulse Energy vs. Lattice Parameter for the re-melted AA2199 samples.

However, despite the possibility of having the original material affect the measurement, the lattice parameter of the sample re-melted with a pulse energy of 0.125J (4.0399Å) displays a significant reduction with respect to pure aluminum (4.0495Å), as well as the AA2199 control sample (4.0485Å). Based on the rule of mixtures it is postulated that the actual lattice parameter of the LRM zone alone, would be lower than that measured here. Previous work by Axon and Hume-Rothery [32] has shown that the inclusion of both lithium and copper within the aluminum lattice in the form of a SSSS results in a decrease in the lattice parameter. It is therefore postulated that a laser pulse-energy of 0.125J, induced the formation of a SSSS involving lithium and copper. This hypothesis is further supported by the XPS solute profile which revealed a minimal surface enriched region within the 0.125J pulse energy sample, indicative of some extent of solute-trapping occurring during solidification. This result provides insight into the possibility of producing microsegregation free AA2199 laser welded joints. Cui et al. produced full penetration welding in an Al-Li alloy 5A90 via continuous Nd:YAG laser beam welding [33]. The authors produced butt joints in 3mm thin-plate using a laser power of 1.8kW and a travel speed of ~45mm/s, resulting in a heat-input of ~34J/mm. This high heat-input resulted in the formation of an equiaxed grain structured within the weld nugget and significant softening of the re-solidified material with respect to the parent material [33]. The loss of hardness was determined to be the result of a reduction in the strengthening precipitate δ' (Al_3Li). The current study reveals that through a reduction of heat-input, it is possible to avoid the formation of an equiaxed zone. This can be accomplished by tuning the average laser power and travel speed to promote a high SFV, resulting in non-equilibrium partitioning at the solid-liquid interface, and producing a fine cellular or featureless solidification structure. The SSSS formed due to the high SFV induced by a heat-input of ~1.5 J/mm could therefore be efficacious to subsequent heat-treatment processing.

5.6 Conclusions

Laser re-melting experiments resulted in low heat-input induced within the base metal during solidification resulting in the formation of a fine cellular solidification structure with laser pulse energies ranging from 0.5 – 0.25 J per pulse. These energies resulted in cell widths ranging from 350 – 250 nm. The resulting cell size was then compared with that predicted by the KGT model to estimate the SFV realized during solidification. It was determined that the SFV within these laser re-melted samples ranged between 3 and 5cm/s. The lowest pulse energy employed (0.125J per pulse) resulted in a low heat-input of ~1.5J/mm and produced a featureless solidified morphology. It was therefore determined that the SFV induced within these samples was on the order of 1m/s, as this is the SFV calculated for absolute stability. The CGM for solute trapping then predicted a deviation from equilibrium partitioning during solidification for all pulse energy levels employed due to the high SFV values. This non-equilibrium partitioning was then measured through the application of XPS depth profiling, where it was revealed that an increase in pulse energy resulted in an increase in surface enrichment of solute (lithium). The lowest pulse energy investigated in this study (0.125J) revealed minimal surface enrichment of lithium after solidification, therefore implying significant solute trapping occurring. Lattice parameter measurements of the RSP material revealed that the samples re-melted with a pulse energy of 0.125J displayed a reduction of the lattice parameter to 4.0399 Å, with respect to the starting material (4.0485 Å) as well as that of pure aluminum. This supports the hypothesis of solute trapping occurring during solidification, as both lithium and copper have been shown to reduce the lattice parameter of aluminum when trapped in SSSS. It is therefore postulated that low heat-input laser re-melting is capable of producing a non-equilibrium featureless solidification morphology.

5.7 Acknowledgments

The authors would like to acknowledge the support of the Natural Science and Engineering Research Council of Canada (NSERC), the McGill University Engineering Doctoral Award (MEDA) as well as that from the Regroupement Aluminium (REGAL), Aluminum Research Centre (REGAL).

5.8 References

[1] Giummarra C, Thomas B, Rioja RJ. NEW ALUMINUM LITHIUM ALLOYS FOR AEROSPACE APPLICATIONS. Proceedings of the Light Metals Technology Conference 2007 2007.
[2] Lavernia EJ, Grant NJ. Aluminium-lithium alloys. Journal of Materials Science 1987;22:1521.
[3] Lavernia EJ, Srivatsan TS, Mohamed FA. Strength, deformation, fracture behaviour and ductility of aluminium-lithium alloys. Journal of Materials Science 1990;25:1137.
[4] Rioja R, Liu J. The Evolution of Al-Li Base Products for Aerospace and Space Applications. Metallurgical and Materials Transactions A 2012:1.
[5] Steuwer A, Dumont M, Altenkirch J, Birosca S, Deschamps A, Prangnell PB, Withers PJ. A combined approach to microstructure mapping of an Al–Li AA2199 friction stir weld. Acta Materialia 2011;59:3002.
[6] Liu Y, Hu Z, Zhang Y, Shi C. The solidification behavior of 8090 Al-Li alloy. Metallurgical and Materials Transactions B 1993;24:857.
[7] Lynch SP, Muddle BC, Pasang T. Ductile-to-brittle fracture transitions in 8090 Al-Li alloys. Acta Materialia 2001;49:2863.
[8] Lynch SP, Muddle BC, Pasang T. Mechanisms of brittle intergranular fracture in Al-Li alloys and comparison with other alloys. Philosophical Magazine A 2002;82:3361
[9] Lynch SP, Wilson AR, Byrnes RT. Effects of ageing treatments on resistance to intergranular fracture of 8090 Al---Li alloy plate. Materials Science and Engineering: A 1993;172:79.

[10] Rioja RJ. Fabrication methods to manufacture isotropic Al-Li alloys and products for space and aerospace applications. Materials Science and Engineering: A 1998;257:100.
[11] Rezaei A, Ahmadi S, Shokunfar A, Foroutan I. Investigation of Homogenization Treatment in Al-Li-Cu-Zr Alloys. Defect and Diffusion Forum 2008;273-276:536.
[12] Boettinger WJ, Coriell SR, Sekerka RF. Mechanisms of microsegregation-free solidification. Materials Science and Engineering 1984;65:27.
[13] Brochu M, Heard DW, Milligan J, Cadney S. Bulk nanostructure and amorphous metallic components using the electrospark welding process. Assembly Automation 2010;30:248.
[14] Brochu M, Portillo JG, Milligan J, Heard DW. Development of Metastable Solidification Structures Using the Electrospark Deposition Process. The Open Surface Science Journal 2011;3:105.
[15] Boettinger W, Shechtman D, Schaefer R, Biancaniello F. The Effect of Rapid Solidification Velocity on the Microstructure of Ag-Cu Alloys. Metallurgical and Materials Transactions A 1984;15:55.
[16] Aziz MJ, Tsao JY, Thompson MO, Peercy PS, White CW. Solute Trapping: Comparison of Theory with Experiment. Physical Review Letters 1986;56:2489.
[17] Baker JC, Gahn JW. Solute trapping by rapid solidification. Acta Metallurgica 1969;17:575.
[18] Smith PM, Aziz MJ. Solute trapping in aluminum alloys. Acta Metallurgica et Materialia 1994;42:3515.
[19] Smith PM, Reitano R, Aziz MJ. Solute Trapping in Metals. Mat. Res. Soc. Symp. Proc., vol. 279: Materials Research Society, 1993.
[20] Guan YC, Zhou W, Li ZL, Zheng HY. Study on the solidification microstructure in AZ91D Mg alloy after laser surface melting. Applied Surface Science 2009;255:8235.
[21] Hoadley AFA, Rappaz M, Zimmermann M. Heat-flow simulation of laser remelting with experimenting validation. MTB 1991;22:101.
[22] Pan QY, Huang WD, Lin X, Zhou YH. Primary spacing selection of Cu 瑕 Mn alloy under laser rapid solidification condition. Journal of Crystal Growth 1997;181:109.
[23] Zhang K, Chen GN. Effect of SiC particles on crystal growth of Al–Si alloy during laser rapid solidification. Materials Science and Engineering: A 2000;292:229.
[24] Cassada WA, Shiflet GJ, Starke EA. The effect of plastic deformation on Al2CuLi (T 1) precipitation. MTA 1991;22:299.
[25] Min D, Shen J, Lai S, Chen J, Xu N, Liu H. Effects of heat input on the low power Nd:YAG pulse laser conduction weldability of magnesium alloy AZ61. Optics and Lasers in Engineering 2011;49:89.
[26] Mullins WW, Sekerka RF. Stability of a Planar Interface During Solidification of a Dilute Binary Alloy. Journal of Applied Physics 1964;35:444.
[27] Bolling GF, Tiller WA. Growth from the Melt. Part II. Cellular Interface Morphology. Journal of Applied Physics 1960;31:2040.
[28] Coriell SR, Sekerka RF. In: Mehrabian R, Kear BH, Cohen M, editors. Rapid Solidification Processing Principles and Technologies. 1980. p.35.
[29] Aziz MJ. Model for solute redistribution during rapid solidification. Journal of Applied Physics 1982;53:1158.

[30] Kurz W, Giovanola B, Trivedi R. Theory of microstructural development during rapid solidification. Acta Metallurgica 1986;34:823.

[31] Zimmermann M, Carrard M, Kurz W. Rapid solidification of Al-Cu eutectic alloy by laser remelting. Acta Metallurgica 1989;37:3305.

[32] Axon HJ, Hume-Rothery W. The Lattice Spacings of Solid Solutions of Different Elements in Aluminium. Proc. R. Soc. Lond. A 1948;193:1.

[33] Cui L, Li X, He D, Chen L, Gong S. Effect of Nd:YAG laser welding on microstructure and hardness of an Al–Li based alloy. Materials Characterization 2012;71:95.

6 Interfacial morphology development and solute trapping behavior during rapid solidification of a Al-Li-Cu alloy[3]

6.1 Preface

The ability of the LRM process to induce planar solidification and ultimately solute trapping generated interest as well in the ESD process. As ESD and LRM display similar heat-inputs, while the ESD process is significantly cheaper and easier to operate, it was of interest to determine if the ESD process was also capable of inducing a planar solidification front at a similar heat-input. Furthermore, as there has been controversy within the literature regarding the solidification behavior of the ESD process, the ability to de-mystify the behavior was deemed to be a potentially important contribution to the scientific community.

6.2 Abstract:

An aluminum-lithium-copper alloy was rapidly solidified via the Electrospark Deposition process. High-resolution Scanning Electron Microscopy (HR-SEM), Time-Of-Flight Secondary-Ion-Mass-Spectroscopy (TOF-SIMS) and Atom Probe Tomography (APT) were employed to investigate the distribution of solute within the deposited materials. The TOF-SIMS data revealed evidence that solute trapping of lithium occurred during solidification, while SEM and 3D-APT revealed the presence of fine copper rich cells within the microstructure (~30-60nm in width). This morphology correlated directly with the microstructural morphology predicted by the Kurz-Giovanola-Trivedi (KGT) model for microstructural development during rapid solidification. The KGT model, which can be used to describe the planar-cellular transition within a microstructure, then predicted a solidification front velocity of ~1m/s being realized during ESD solidification. This SFV

---

[3] Published in Acta Materialia (In Press) 2013

corroborated the chemical mapping data, and therefore supported the solute trapping hypothesis, as the Continuous Growth Model for solute trapping as developed by Aziz and Kaplan predicts significant trapping of lithium at a SFV of 1m/s. Finally APT revealed the presence of Al_3Li phase upon the copper rich cell walls. It was then determined that the Al_3Li was not formed during solidification, as predicted by a time dependent nucleation model for phase prediction during rapid solidification, and therefore is the result of a subsequent aging process.

6.3 Introduction

Aluminum-lithium (Al-Li) alloys have garnered interest within the aerospace industry due to their low density and high strength, with a focus on the new generation alloys, such as the aluminum-lithium-copper alloy AA2199, developed by Alcoa [1] [2, 3]. However, one obstacle to wide spread implementation of Al-Li alloys has been the difficulties associated with fusion welding of lithium containing alloys. During solidification Al-Li alloys experience solute segregation, or microsegregation, due to the partitioning of lithium [4] and other alloying elements such as copper [5]. Although these issues can be circumnavigated through post-solidification thermal-mechanical treatment [6], the high lithium diffusivity in the solid state, with respect to other alloying elements, may lead to further lithium depletion during subsequent homogenization heat treatments [7, 8]. A solidification technique capable of producing an Al-Li deposit with a homogeneous chemical distribution would remove the necessity for a homogenization heat-treatment and expand the range of applicable processing conditions for Al-Li alloys.

Rapid solidification processing (RSP) of aluminum alloys have been widely studied, and the ability to capture, or engulf solute atoms within a rapidly progressing solid-liquid interface has been proven [9]. This entrapment phenomenon has become to be known as “solute trapping”. Several models describing the behavior of solute trapping during RSP have been developed, such as the Baer et al. model [10], or the Continuous Growth Model (CGM) of Aziz and Kaplan that has been shown to accurately describe the solute trapping behavior of aluminum alloys [11, 12]. Smith and Aziz [13] have performed pulsed laser remelting experiments on various dilute (<1at.% solute) binary aluminum alloy systems to validate the CGM, including the aluminum-copper system, and it has therefore been deemed accurate in describing interface attachment kinetics. While the CGM describes the attachment kinetics, the Mullins and Sekerka interfacial stability theory was developed to the interfacial morphology during solidification [14]. The Mullins and Sekerka model predicts the critical solute concentration required for a planar interface to become unstable and breakdown to form a cellular interface, for a given solidification front velocity (SFV) [14]. However, while the Mullins-Sekerka model does include surface tension effects, it assumes local equilibrium at the liquid-solid interface, as the model was developed to describe interfacial morphology changes at low growth rates, or low SFV, where interfacial equilibrium is a reasonable assumption. As RSP results in large deviations from equilibrium at the liquid-solid interface, the model was later modified by Hoglund et al. for applications of rapid solidification [15]. A more recently developed model that was developed with RSP in-mind is that of Kurz, Giovanolva and Trivedi (KGT) [16]. The KGT model can be used to describe the microstructural development of an alloy during rapid solidification by accounting for the stabilization of an interface at a high SFV due to increased surface tension.

Electrospark deposition (ESD) is a micro-arc welding process that has a high energy density and low heat-input [17]. The low heat-input combined with small amount of material deposited each pulse, results in cooling rates on the order of 10^5-10^6 °C/s being realized [18]. This rapid solidification therefore allows the formation of non-equilibrium microstructures, as previously displayed by the formation of nanostructured Al-Si [19] and Al-Ni [20] alloys, and the deposition of amorphous alloys [21, 22]. As conventional solidification is heat-flow limited, the effect of local interface conditions on the resulting solid are minimal. This however is not true for rapid solidification, in which interface conditions, such as solute distribution play a direct role in the morphology of the solidified material. Saepen and Turnbull have estimated that the local liquid-solid interface conditions become of importance when the temperature decay profile reaches ambient temperature at a distance of ~60μm in pure metals and ~1mm in metallic alloys [23]. When a such a temperature decay profile is achieved the regime of interface-limited growth begins [23], and the importance of interface conditions are amplified. While the exact SFV induced by such a thermal decay profile would be a function of the given melt properties, the resulting solid would exhibit a non-equilibrium microstructure. Various researchers have investigated the mass transfer mechanisms of ESD [24-27], however few have studied the solidification behavior, and ultimately liquid-solid interface characteristics of the process. Xie and Wang [28, 29] made an initial attempt at estimating the SFV of an ESD deposited MCrAlY alloy, however the authors estimated the SFV through the application of constitutional supercooling criterion, and therefore neglected to account for the increased interface stability due to surface tension.

The objective of this paper is to investigate the rapid solidification behavior of ESD deposited material and to assess the ability of ESD to induce solute trapping behavior. The chemical distribution of solute was measured within RSP material and compared with the CGM model for solute trapping. Furthermore, the microstructural morphology was compared with the microstructure predicted by the KGT model. This then allowed for the estimation of solidification properties such as the SFV realized during ESD as well as the stable interface morphology.

6.4 Experimental procedure

Rapidly solidified samples of AA2199 (composition displayed in Table 6-1) were manufactured using an Electrospark Deposition (ESD) process. Deposition was performed using a capacitance of 100uF and a voltage of 100V, with a discharge frequency of ~1kHz in an Ar environment containing at most 0.1 ppm O_2. Electrodes (anodes) of ~1.75mm in diameter were manufactured from a sheet of AA2199. The ESD material was then deposited upon an AA2199 alloy substrate (cathode) material to prevent dilution of the solute due to mixing of the anode and cathode materials. Figure 6-1(a) displays a schematic of the ESD process used throughout this experiment, while Figure 6-1(b) displays a close-up schematic detailing the positioning of the electrode and the substrate [30].

Table 6-1 - Composition of AA2199 in atomic percentage.

Element	Al	Li	Cu	Zn	Mg	Mn	Zr	Fe	Si
[at.%]	Bal.	5.3-6.8	1.0-1.2	0.1-0.4	0.05-0.4	0.1-0.5	0.1-0.4	0.03max	0.05max

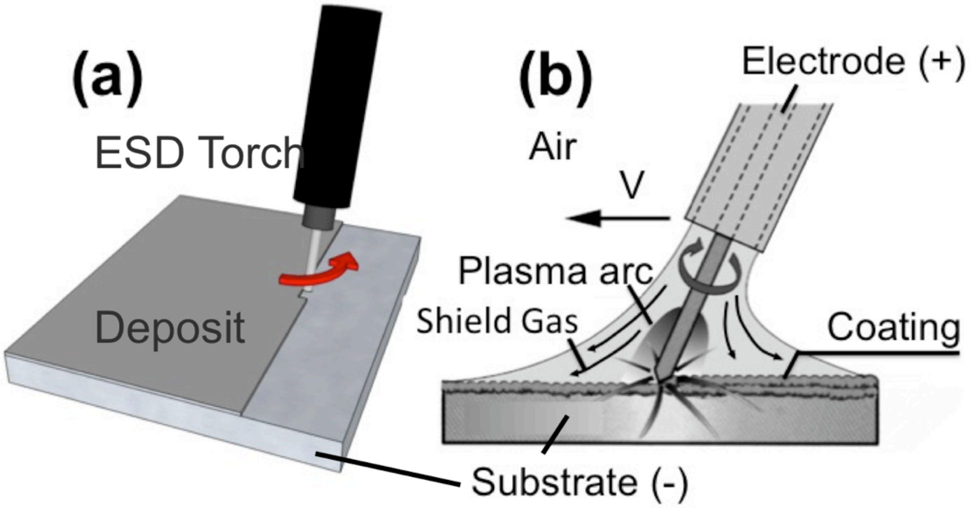

Figure 6-1 - (a) Schematic of the ESD set-up used throughout the experiment; (b) schematic of the electrode substrate region [30].

Time-of-Flight Secondary-Ion-Mass-Spectroscopy analysis was performed using an IONTOF TOF-SIMS IV in both negative and positive modes. Bismuth ions were used for surface milling of the sample. Surface mapping and depth profiling were performed on the same TOF-SIMS instrument. TOF-SIMS experiments were then repeated using the same parameters on a Ta_2O_5/Ta standard, and the resultant depth was then measured within an AFM to determine an approximate milling rate for the AA2199 samples.

Microscopy Analysis was performed using a Hitachi SU-8000 Scanning Electron Microscope (SEM) in both backscattered diffraction mode, for bulk samples, as well as Scanning Transmission Electron Microscopy (STEM) mode for thin disc samples. STEM samples were prepared through grinding until a desired thickness of 100um was achieved, then electro-jet polished in a mixture of 30% HNO_3 and 70% CH_3OH. The current and voltage were ~31uA and 2kV respectively.

Atom Probe Tomography (APT) was performed using a LEAP4000XHR instrument located at the University of Michigan. Needles were prepared using a FEI Quanta 3D FEG Focused Ion Beam (FIB) microscope, with Ga ions as an etchant. Specimens were analyzed in both voltage and laser pulsing modes at a base temperature of 37K, with a pulse repetition rate of 200kHz, an evaporation rate of 0.005 atom/pulse, a voltage pulse amplitude of 15% or a laser pulse energy of 70pJ. The IVAS software was used for data reconstruction using an image compression factor of 1.2 and an evaporation field of 19V/nm.

6.5 Results and Discussion

6.5.1 Heat-flow during ESD solidification

As the equilibrium partition coefficients of lithium and copper within aluminum are 0.55 [31] and 0.15 [32] respectively , it is well known that these solutes will segregate during conventional solidification. This segregation results in an increased solute content at grain boundaries [33]. In an attempt to reduce this segregation by inducing solute trapping during solidification, AA2199 was rapidly solidified using the ESD process. Due to the low heat-input of the ESD process combined with the small amount of material transferred during each pulse, solidification proceeds very rapidly. To determine if the ESD process enters the realm of interface limited growth, the temperature decay profile for a single ESD pulse was estimated through the application of the Adam's 2-dimensional heat-flow equation (Equation 6-1) [34].

$$\frac{1}{T_p - T_0} = \frac{4.13 V Y g \rho C}{H_{net}} + \frac{1}{T_m - T_0} \qquad \text{(Equation 6-1)}$$

Where T_p is the temperature realized at a given position, T_0 is the initial temperature of the substrate, T_m is the melting temperature of the substrate material, g is the substrate thickness, H_{net} is the heat-input of the ESD splat, V is the velocity of the ESD torch relative to the substrate, Y is the distance from the center of the splat-deposition, ρ is the density and C is the specific heat of the workpiece.

As the particular ESD used during the experiments consisted of an RC circuit, the heat-input (H_{net}) was calculated as a function of the fraction of the capacitor bank discharge using Equation 6-2. Complete discharge of the capacitor bank during deposition is typically not observed, and therefore the true heat-input realized should be some fraction of this estimated value.

$$H_{net} = n * \frac{1}{2} C V^2 \qquad \text{(Equation6- 2)}$$

Where C is the capacitance and V is the voltage used to charge the capacitor bank, and n is the fraction of total capacitor discharge (ranging between 0.1 and 1).

The resulting thermal decay profiles are revealed in Figure 6-2. Thermal decay to a temperature below 100°C was determined to occur within ~30μm of the ESD pulse location, therefore supporting the hypothesis that mechanisms related to interface-limited growth are of importance during the solidification of ESD deposited material. It is therefore reasonable to apply the CGM for solute trapping as developed by Aziz et al. for RSP, to the solidification of ESD deposited material.

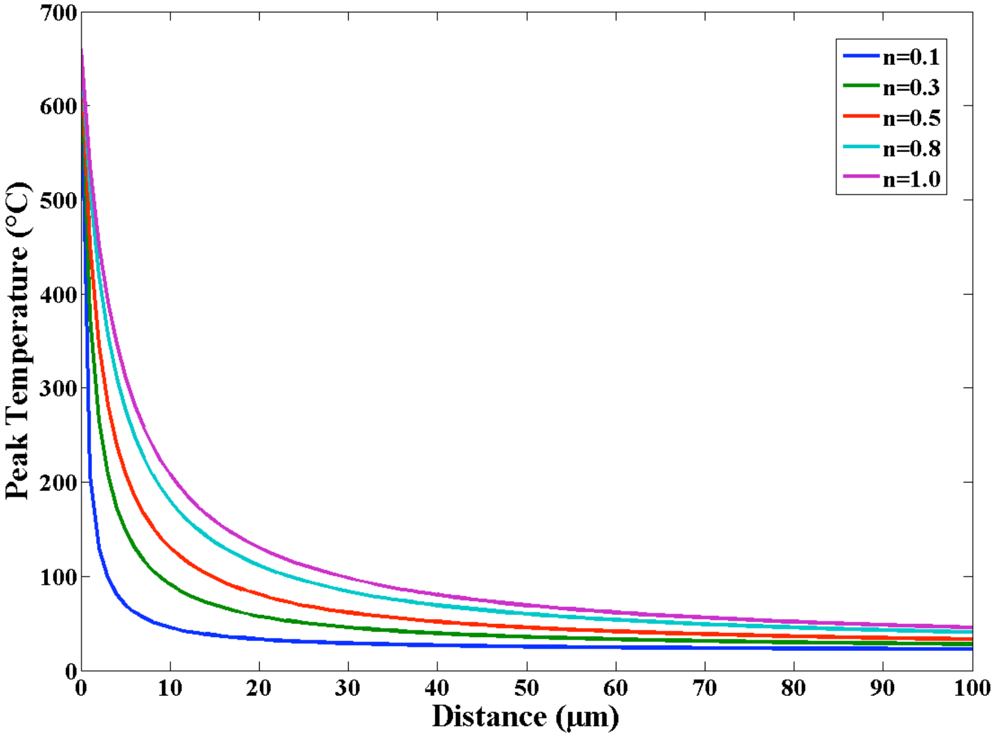

Figure 6-2- Thermal decay profiles as a function of the capacitor discharge fraction (n).

6.5.2 Solute Trapping Behavior of ESD Solidification

The CGM is used to estimate the effective partition coefficient during solidification as a function of SFV. The CGM was then applied to calculate the effective partition coefficients of lithium and copper within aluminum using Equation 6-3 and is displayed within Figure 6-3.

$$k(v) = \frac{\frac{v}{v_D} + k_{eq}}{\frac{v}{v_D} + 1} \qquad \text{(Equation 6-3)}$$

Where v is the SFV, v_D is the diffusive speed, and k_{eq} is the equilibrium partition coefficient.

The diffusive speed (v_D) is physically defined as the time required for an atom to diffuse across the solid/liquid interface, and therefore can be calculated by dividing the interface diffusivity D_I, by the interface width (L). However, as discussed by Smith et al. [35] difficulties in measuring both interface diffusivity and width render the direct calculation of v_D inaccurate. While investigating the solute trapping behavior of aluminum alloys, Smith and Aziz [13] noted an inverse relationship between the diffusive speed and the equilibrium partition coefficient. The authors also noted this relationship within silicon alloys.

During the calculation of this model the diffusive speed of copper at concentrations of 1 atomic percent was taken to be 6.7m/s as determined by Smith and Aziz during pulsed laser re-melting experiments [13]. The diffusive speed of lithium within aluminum was then calculated based on the assumption of an inverse relationship between the diffusive speed and the equilibrium partition coefficient as stated by Smith and Aziz [13]. Therefore the value of the diffusive speed of lithium within aluminum was estimated as 1m/s.

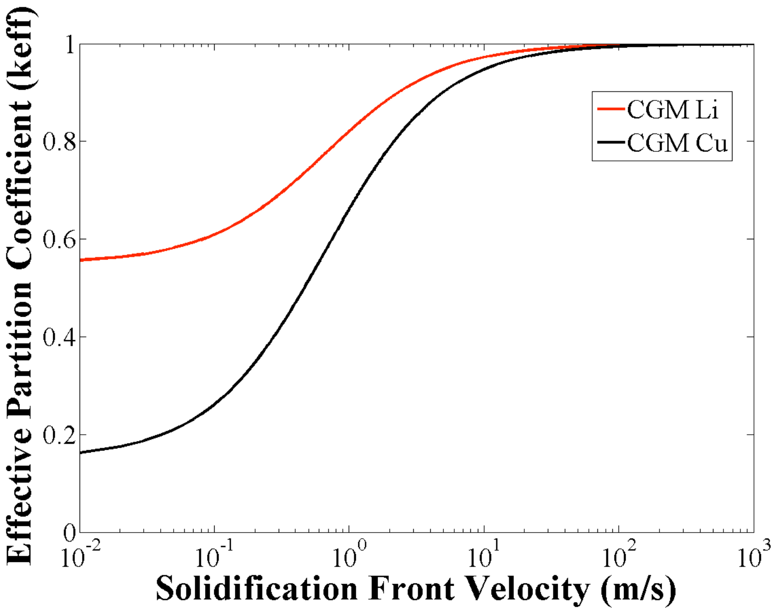

Figure 6-3- Effective partition coefficient vs. SFV as described by the Aziz model.

The resulting curves for effective partition coefficient vs. SFV reveal a significant increase in the extent of solute trapping (increase in partition coefficient) with increasing SFV. The CGM predicts significant deviations from equilibrium partition coefficient values for both lithium and copper within aluminum, at a SFV greater than 0.1m/s. For complete solute engulfment (k=1) to occur the CGM predicts a SFV of ~100m/s is required.

It should be noted that the equilibrium partition coefficient of lithium (0.55) is greater than that of copper, as such, the calculated effective partition coefficient curve for lithium within aluminum is greater than that of copper within aluminum at all values of SFV, implying that assuming that there is no competition between lithium and copper for lattice sites, the segregation of copper atoms will be the limiting factor during the ESD solidification process. The assumption of no competition for the occupation of aluminum lattice sites between lithium and copper during solidification is justified as the atomic radii of aluminum, lithium, and copper are 143, 152, and 128pm respectively [36], therefore lithium and copper are substitutional elements within the aluminum lattice, and due to the high number of available sites with respect to atomic concentrations of the two solutes, competition can be neglected. Furthermore, the copper-lithium phase diagram [37], predicts no phase formation between the pair, and analysis of the enthalpy of mixing between Al-Li, Al-Cu, and Li-Cu, predicts no significant interaction between lithium and copper. Furthermore, to ensure that the usage of the equilibrium partition coefficient of the binary alloys (Al-Cu and Al-Li) was acceptable, the partition coefficients of lithium and copper within the ternary alloy was calculated through the application of the FactSage thermodynamic software package. The liquidus and solidus projections were calculated, and used to calculate the partition coefficient of both solutes via the relationship, $k_{eq}=C_S/C_L$, where C_S and C_L are the solute content in the solid and liquid respectively. Comparison of the calculated ternary partition coefficients with those calculated from the binary systems, across the solidification range, are displayed in Figure 6-4.

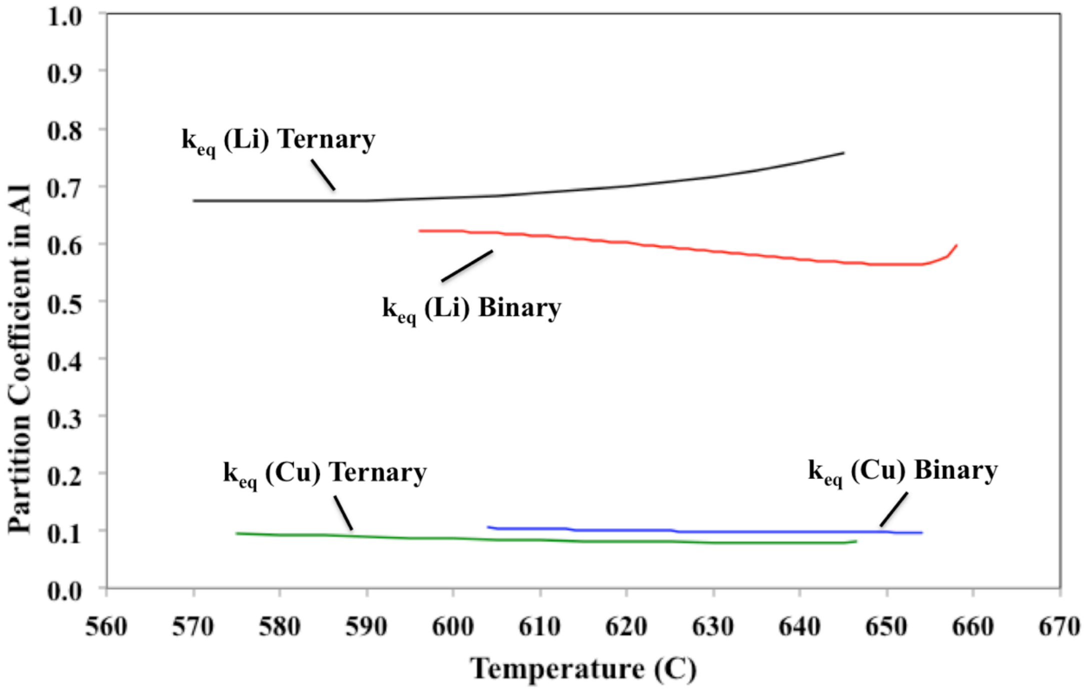

Figure 6-4- Comparison of the partition coefficients of Li and Cu in Al, calculated for the binary Al–X and Al–Li–Cu systems.

The comparison reveals a negligible variation of the partition coefficient of copper between the ternary and binary systems. While a more significant change in partition coefficient of lithium occurs between the ternary and binary systems, the effect of SFV on k_{eq} is more pronounced. It is therefore appropriate to use the binary partition coefficient values as the k_{eq} value for the CGM model.

To serve as a control, a sample of AA2199 was solidified under an argon atmosphere with a controlled cooling-rate of ~1K/s (see Appendix 1). As expected, significant segregation of the solute towards the aluminum dendrite tips occurred, as revealed through EDS mapping of copper throughout the microstructure (see Appendix 1), resulting in the formation of a large areas of the copper rich θ-phase. The microstructure of the as-deposited material is displayed in Figure 6-5. This micrograph displays a grain-size of ~4-6µm, a significant reduction to that of the equilibrium cooled control sample, with some intragranular precipitates present. As the solidification of material deposited via ESD can be thought of as uni-directional, upward from the substrate [25, 29], the presence of solute would result in the last material to solidify (the surface) being solute enriched. TOF-SIMS mapping of an area 100μm by 100μm, on the surface of an ESD solidified sample is shown in Figure 6-6. This particular scan area was selected as it is significantly larger than grain size of the deposited material, as displayed in Figure 6-5, therefore if grain-boundary segregation were to occur it should be detected. Figure 6-6 shows that elemental lithium and the most common lithium isotope (Li^6), as well as copper (Cu^{63}) were homogeneously distributed throughout the microstructure. The homogeneous lateral distribution of lithium and copper within the AA2199 ESD deposited material is evidence of the avoidance of solute-segregation to grain-boundaries during ESD solidification.

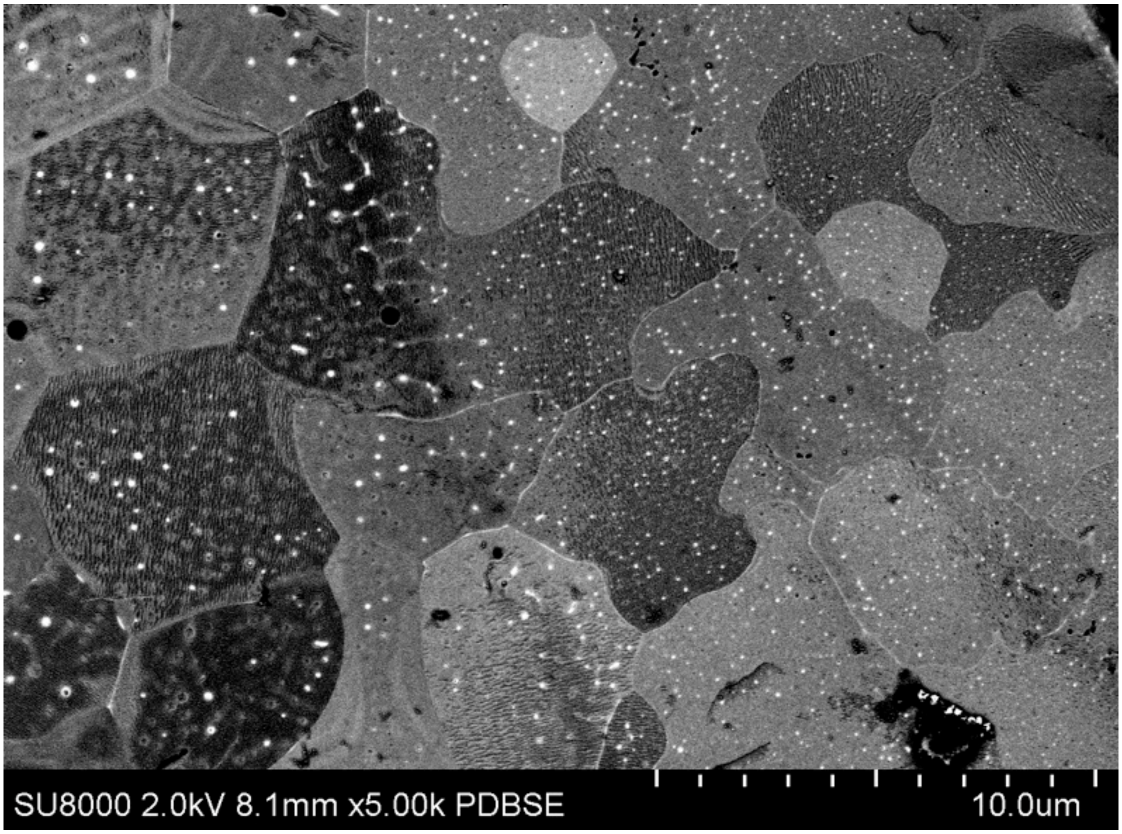

Figure 6-5- Back-Scattered electron micrograph of ESD deposited AA2199 displaying ~5-7um grain size.

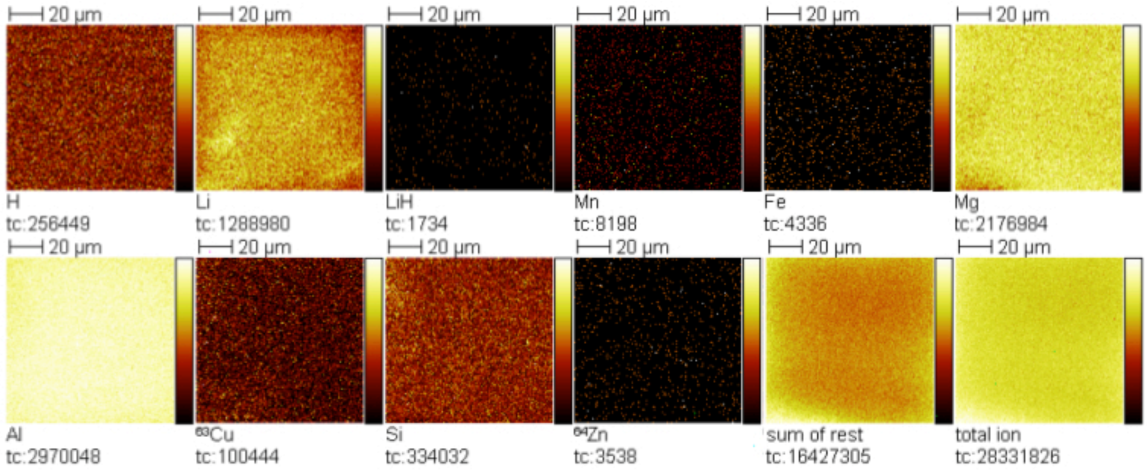

Figure 6-6- TOF-SIMS mapping of solute distribution within as-deposited ESD AA2199.

The TOF-SIMS was also operated in the semi-quantitative depth profile analysis mode, to determine distribution of the lithium and copper with respect to the solidification direction. Depth profile analysis was performed in various locations throughout the microstructure and a representative sample is displayed here. It should be noted that the spatial resolution of the TOF-SIMS is on the order of 100nm, the depth resolution is on the order of several monolayers, and is therefore significantly more sensitive that then lateral chemical profiling. The resulting TOF-SIMS depth profiles are displayed in Figure 6-7. The etching rate was estimated to be ~0.06nm/s of Ta_2O_5/Ta equivalent. This was then used to estimate the depth of etching during the TOF-SIMS depth profile experiments.

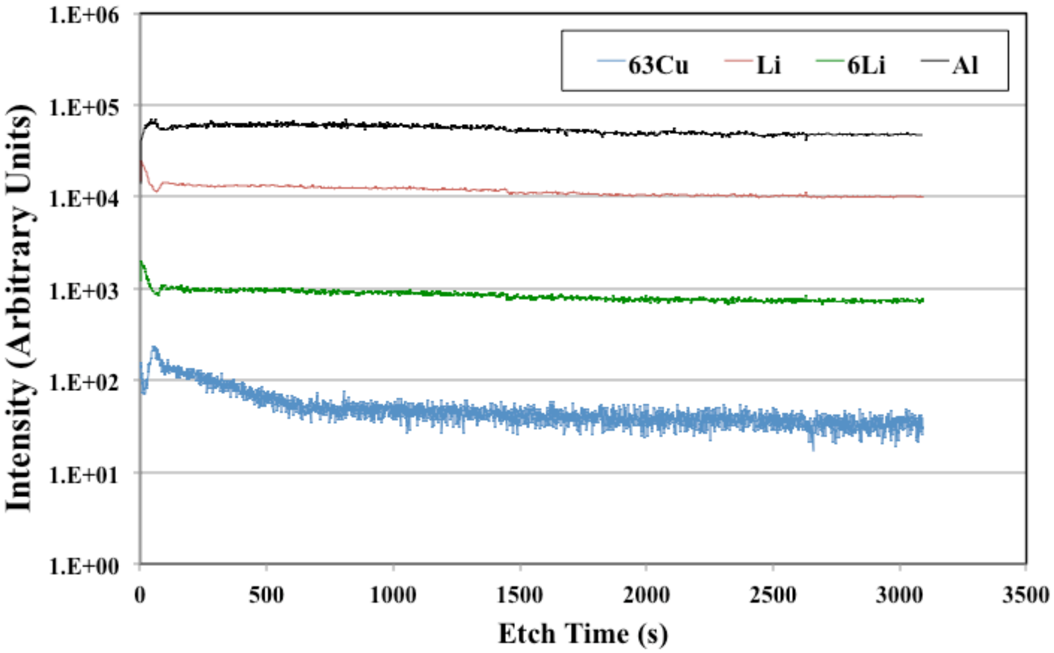

Figure 6-7- TOF-SIMS depth profile revealing homogeneous solute (lithium and copper) distribution.

The depth profiles reveal a consistent vertical distribution of lithium and Li^{6}, this is indicative of some extent of solute-trapping occurring. If equilibrium partitioning were to take place, the final solidified layer (closest to the surface) should be significantly enriched in solute. This however, was not the case, and the depth profile data is in support of the solute-trapping hypothesis. The depth profile of copper displays an enrichment of copper towards the surface of the deposited material. This enrichment is indicative of some extent of solute segregation of copper occurring during ESD solidification. As the ESD process involves solidification of both the electrode and substrate materials (both AA2199 in this case), knowledge of the initial solute profile of either substrate or electrode will therefore not be applicable to the solute profile obtained after deposition. It was therefore not possible to estimate an achieved partition coefficient or SFV from chemical profile data alone.

6.5.3 Microstructural analysis of ESD deposited AA2199

Further High-Resolution SEM investigation of the deposited material revealed the presence of a fine cellular structure consisting of 30-40nm wide cells, as displayed in Figure 6-8(a). The chemical composition of the cell walls was then measured through the application of an ESD line scan across a cell wall with an accelerating voltage of 2KeV (producing an interaction volume of approximately 20nm as predicted using a Monte Carlo software package) and revealed significant copper enrichment (shown in Figure 6-8(b)). This microstructural morphology is therefore consistent with the breakdown of the solid-liquid interface from a planar morphology to a cellular one. This occurs as perturbations that form within the advancing planar interface distort the temperature fields along the interface, resulting in solute redistribution. This cellular morphology was not clearly detected within the lateral TOF-SIMS mapping analysis, as the spatial resolution of the instrument is ~100nm, which is greater than that of the cell size (~30-60nm).

This cellular structure has been reported to arise in RSP of similar materials in previous studies [38, 39]. Zimmermann et al. reported a wavy cellular eutectic structure on the same order of magnitude (~40nm) at solidification front velocities between 20 and 50 cm/s during the laser remelting of a eutectic aluminum-copper alloy [39]. Lieblich and Torralba also reported a cellular structure in rapidly solidified Al-Li-Ti alloys [38]. The authors reported a fine cellular structure with cell diameters on the order of 0.5µm, and an enrichment of titanium within the cells. The cellular structure obtained in the ESD deposited material during our experiment is not present throughout the entire ESD deposit. In fact a planar interface is initially noted, prior to the stabilization of the cellular interface. This initial planar interface is due to the extremely high thermal gradient experienced by the material in direct contact with the substrate. The fact that the microstructure evolves from a planar to cellular morphology leads the authors to believe that spinodal decomposition of the solid solution is not directly responsible for the cellular microstructure. It has been previously shown that spinodal decomposition of aluminum-copper alloys occurs at room temperature and results in the formation solute lean and solute rich areas [40]. However as the solute compositions of both the planar and cellular areas are identical, it is believed that this microstructural morphology transition is the result of a change in the solid-liquid interface morphology. This morphological change allows for a reference point of sorts, when making comparisons between the observed microstructure and that predicted by the KGT model. It is therefore possible to infer the solidification characteristics prior to and subsequent to the reference point of morphology change within the ESD deposited material.

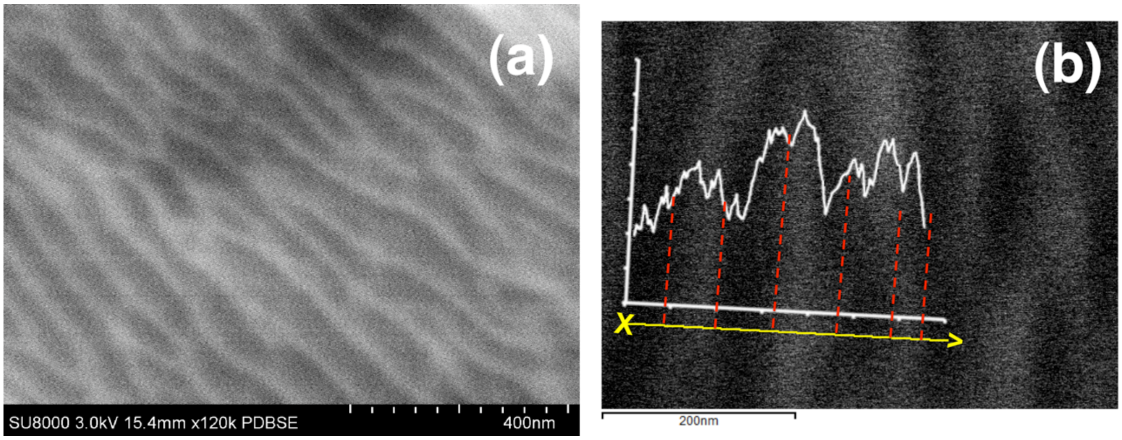

Figure 6-8- (a) Back-Scattered electron micrograph of as-deposited AA2199 revealing fine cellular structure, (b) High-resolution Cu EDS line scan of Cu concentration across cellular feature.

The Kurz-Giovanola-Trivedi (KGT) model for interface stability at low and high SFV can then be applied to determine the solidification properties such as SFV. The KGT model allows one to calculate the dendrite tip radius during solidification, and therefore determine the point at which a planar interface becomes unstable and forms a cellular morphology. The KGT model calculates the dendrite tip radius through Equation 6-4.

$$R = 2\pi \left[\frac{\Gamma}{mG_c\xi_c - G}\right]^{1/2} \qquad \text{(Equation 6-4)}$$

Where R is the dendrite tip radius, Γ is the Gibbs-Thompson coefficient, m is the slope of the liquidus line of the phase-diagram, G_c is the concentration gradient of the solute at the liquid-solid interface, G is the mean temperature gradient at the interface, and

$$\xi_c = 1 - \frac{2k}{\left[1+\left(\frac{2}{P}\right)^2\right] - 1 + 2k} \qquad \text{(Equation 6-5)}$$

Where P is the Péclet number.

The thermal gradient (G) used throughout the calculations was derived from the derivative of the thermal decay model. As the Adam's 2-D heat-flow equations estimates T as a function of position in both the X and Y directions, then it was possible to use $\partial T/\partial X$ and $\partial T/\partial Y$ to estimate a thermal gradient in various locations throughout the deposit. Furthermore, it should be noted that at higher SFV values, the dependence of R on G is very small, and therefore the approximate nature of the G estimation is suitable. The G_c value was determined through the application of a mass balance across the dendrite tip.

As during RSP, it is well known that the partition coefficient (k) and slope of the liquidus line on the phase diagram (m), are a function of the SFV, and therefore models to describe the effect of velocity on these parameters must be included within the KGT model. To accomplish this the KGT model was modified to include a velocity dependent partition coefficient, as described by the CGM [11] displayed in Equation 6-3, as well as a velocity dependent kinetic liquidus slope, as derived by Boettinger [41], and displayed in Equation 6-6.

$$m\big(k(v)\big) = m_c\left(1 + \frac{k_{eq-k\left[1-ln\left(\frac{k}{k_{eq}}\right)\right]}}{1-k_{eq}}\right) \qquad \text{(Equation 6-6)}$$

Where m_c is the equilibrium slope of the liquidus line of the phase-diagram, and k is the effective partition coefficient, as calculated using Equation 6-3.

The Péclet number and dendrite tip radius as a function of the SFV were then calculated. The velocity criterion was solved numerically through the application of the Newton-

Raphson method, where the initial velocity guess was determined using the Maximum Velocity Criterion equation as developed by Bolling and Tiller [42]. The convergence criteria used was:

$$e = \frac{v_{i+1} - v}{v_i} < 0.001 \qquad \text{(Equation 6-7)}$$

Zener approximation was then applied to solve the Ivantsov approximation.

Figure 6-9 (a) and (b) display the Péclet Number and Dendrite Tip Radius as a function of SFV respectively. The KGT model therefore predicts the breakdown from a planar-interface (infinite dendrite tip radius) to a cellular morphology at a SFV of approximately 1-2m/s. Since it is possible to view the particular location within the deposited sample in which the cellular morphology appears, and the microstructure prior to the cellular breakdown location implies the propagation of a planar interface, one can then infer that the initial SFV imparted by the ESD is greater than 1-2m/s. A SFV in the range of 1-2m/s also corroborates the solute-trapping hypothesis supported by the chemical profile data, as the CGM model predicts significant trapping of both lithium (k_{eff}=~0.85) and copper (k_{eff}=~0.7) within the aluminum matrix at a SFV of ~1-2m/s.

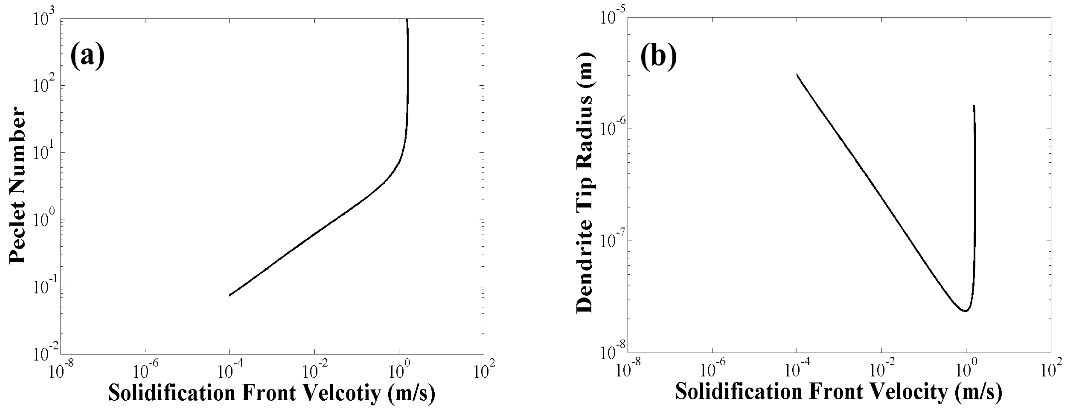

Figure 6-9- (a) Péclet Number vs SFV, (b) Dendrite Tip Radius vs SFV

Furthermore, it can be deduced from Figure 6-9(b) that when the planar interface no longer remains stable, the initial radius of the cellular perturbations formed within the rapidly solidified AA2199 material is on the order of ~20nm, implying a cell width of ~40nm. This predicted value closely correlates with the measured cell width of ~30-60nm.

This result is in direct disagreement with the findings of Xie and Wang [28, 29], where the authors calculated the approximate SFV using constitutional supercooling theory. However constitutional supercooling theory neglects the stabilization of the interface via surface tension effects, and is therefore not a valid approach for the ESD process.

As it was not possible to deduce whether or not lithium is involved in the cellular morphology during the TOF-SIMS analysis (due to spatial resolution) or during the EDS analysis (due to difficulties in analyzing lithium using electron microscopy techniques), atom probe tomography (APT) was applied to analyze the chemical composition of a cell. The APT analysis performed on the rapidly solidified ESD material confirms the presence and spacing of the copper rich cells as displayed in Figure 6-10. It is also noted that while lithium is not present within the cell walls, clusters of lithium atoms decorate the copper rich cell walls. Further analysis of the lithium rich areas revealed the chemical composition of the clusters is close to that of stoichiometric metastable Al_3Li (δ') phase (see Figure 6-11). It is therefore of interest to determine if the metastable Al_3Li phase formed during solidification, or if it was precipitated from a supersaturated solid solution in either an aging process due to subsequent layer deposition, or natural aging, as has been shown to occur by Baumann and Williams [43]. Dai et al. have studied the nucleation and formation of the stable and metastable phases present in undercooled Al-Li melts during atomization [44]. Their findings revealed that at hypoeutectic compositions (>~26at.% Li), nucleation of Al is favoured for all cooling-rates. This claim was then validated using a model for prediction of phase suppression during RSP by via time dependent nucleation theory as developed by Shao and Tsakiropoulos, for predicting phase-suppression during RSP [45] (procedure shown in Appendix 6.2.).

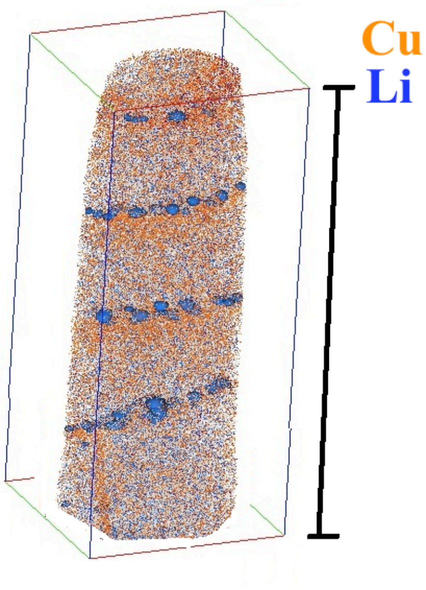

Figure 6-10- 3D reconstruction from an APT analysis displaying Cu and Li distribution. The blue surfaces delineate regions of Li concentrations greater than 10at.%Li. The scale bar represents 150nm.

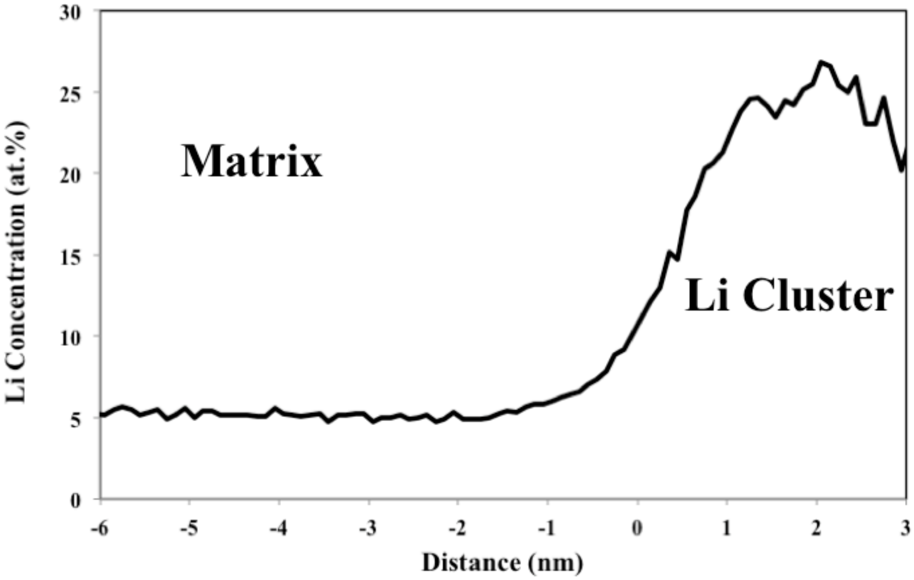

Figure 6-11- Proximity histogram based on the Li-isoconcentration surfaces shown in Figure 10, revealing the average Li concentration in the Li-rich clusters..

It is therefore postulated that the cellular structure was formed prior to the precipitation of Al_3Li upon the cell walls, and not vice-versa. This phenomenon was also noted by Leiblich and Torralba during the RSP of Al-Li-Ti alloys [38]. The authors postulated that the preferential coarsening of the Al_3Li phase on the Ti rich cell walls was due to the Ti gradient throughout the microstructure. The authors go on to state that the Ti in solid solution must retain vacancies, which are essential to assist in the lithium diffusion, and therefore restricts Li mobility. It is assumed a similar phenomenon is occurring with copper in this case and therefore responsible for the heterogeneous coarsening of Al_3Li.

6.6 Conclusions

It was determined that rapidly solidified AA2199 via the ESD process displayed evidence of solute trapping due to a high solidification front velocity. TOF-SIMS mapping techniques revealed a homogeneous distribution of lithium within the RSP material, while TOF-SIMS depth profiling revealed some surface segregation of copper.

Microstructural analyses of the deposited material revealed the transformation of a planar morphology to that of very fine copper rich cells, ranging from 30-60nm in width. The KGT model for microstructural development during rapid solidification was applied to gain insight into the solidification behavior of the ESD material. The KGT model predicted an interface stability threshold SFV of ~1-2m/s, above which the interface will remain planar, and below which a cellular morphology will form. This transitional SFV therefore supports the argument of solute trapping occurring, as the CGM model predicts significant deviations from equilibrium partitioning for both lithium and copper at velocities on the order of 1m/s. Furthermore, the KGT model accurately predicts the cellular morphology subsequent to interfacial breakdown. The model predicted a cellular radius of approximately ~20nm (or ~40nm wide cells), which is in direct correlation with the microstructural analysis of the rapidly solidified material. Therefore supporting the hypothesis that the ESD process is capable of producing a SFV in excess of 1m/s and therefore able to induce solute-trapping behavior during solidification.

It was not possible to determine the role lithium played in the cellular formation through application of TOF-SIMS or EDS, therefore APT was employed. The APT analysis revealed that lithium was not present within the cell walls, however globular Al_3Li was found present upon the copper rich cell walls. A time dependent nucleation theory was then applied to determine that the metastable Al_3Li phase was not formed during solidification, but instead precipitated out of solid solution during a natural aging process.

6.7 Acknowledgments

The authors would like to acknowledge the support of the Natural Science and Engineering Research Council of Canada (NSERC), the McGill University Engineering Doctoral Award (MEDA) as well as that from the Regroupement Aluminum Research Centre (REGAL). The authors would also like to acknowledge the technical assistance of Mr. Nicolas Brodusch and Ms. Suzie Poulin. Finally the authors would like to thank Mr. Christian Banner for performing some of the APT sample preparation and experiments and Mr. Manas Paliwal and Mr. Dong-Geun Kim for the fruitful discussions.

6.8 References

[1] Giummarra C, Thomas B, Rioja RJ. NEW ALUMINUM LITHIUM ALLOYS FOR AEROSPACE APPLICATIONS. Proceedings of the Light Metals Technology Conference 2007 2007.
[2] Ma YE, Staron P, Fischer T, Irving PE. Size effects on residual stress and fatigue crack growth in friction stir welded 2195-T8 aluminium – Part I: Experiments. International Journal of Fatigue 2011;33:1417.
[3] Steuwer A, Dumont M, Altenkirch J, Birosca S, Deschamps A, Prangnell PB, Withers PJ. A combined approach to microstructure mapping of an Al–Li AA2199 friction stir weld. Acta Materialia 2011;59:3002.
[4] Berzina IG, Gusev EB, Ivanov VA, Lukin VI. Investigation of Li distribution in aluminium alloy welds by elemental radiographic analysis. International Journal of Radiation Applications and Instrumentation. Part D. Nuclear Tracks and Radiation Measurements 1992;20:261.
[5] Chen S-W, Chuang Y-Y, Austin Chang Y, Chu M. Calculation of phase diagrams and solidification paths of Al-rich Al−Li−Cu alloys. Metallurgical and Materials Transactions A 1991;22:2837.
[6] Sokolowski JH, Sun X-C, Byczynski G, Northwood DO, Penrod DE, Thomas R, Esseltine A. The removal of copper-phase segregation and the subsequent improvement

in mechanical properties of cast 319 aluminum alloys by a two-stage solution heat treatment. Journal of Mat. Pro. Tech. 1995;53:385.

[7] Papazian J, Schulte R, Adler P. Lithium depletion during heat treatment of aluminum-lithium alloys. Metallurgical and Materials Transactions A 1986;17:635.

[8] Esposto FJ, Zhang CS, Norton PR, Timsit RS. Segregation studies of an Al---Li alloy. Surface Science 1993;290:93.

[9] Baker JC, Cahn JW. Solute trapping by rapid solidification. Acta Metallurgica 1969;17:575.

[10] Baeri P, Poate JM, Campisano SU, Foti G, Rimini E, Cullis AG. Dependence of trapping and segregation of indium in silicon on the velocity of the liquid-solid interface. Applied Physics Letters 1980;37:912.

[11] Aziz MJ. Model for solute redistribution during rapid solidification. Journal of Applied Physics 1982;53:1158.

[12] Aziz MJ, Kaplan T. Continuous growth model for interface motion during alloy solidification. Acta Metallurgica 1988;36:2335.

[13] Smith PM, Aziz MJ. Solute trapping in aluminum alloys. Acta Metallurgica et Materialia 1994;42:3515.

[14] Mullins WW, Sekerka RF. Stability of a Planar Interface During Solidification of a Dilute Binary Alloy. Journal of Applied Physics 1964;35:444.

[15] Hoglund DE, Aziz MJ, Stiffler SR, Thompson MO, Tsao JY, Peercy PS. Effect of nonequilibrium interface kinetics on cellular breakdown of planar interfaces during rapid solidification of Si-Sn. Journal of Crystal Growth 1991;109:107.

[16] Kurz W, Giovanola B, Trivedi R. Theory of microstructural development during rapid solidification. Acta Metallurgica 1986;34:823.

[17] Johnson RN, Sheldon GL. Advances in the electrospark deposition coating process. Journal of Vacuum Science & Technology A: Vacuum, Surfaces, and Films 1986;4:2740.

[18] Johnson RN. ElectroSpark Deposition: Principles and Applications. 45th Annual Technical Conference Proceedings 2002:87.

[19] Milligan J, Heard DW, Brochu M. Formation of nanostructured weldments in the Al-Si system using electrospark welding. Applied Surface Science 2010;256:4009.

[20] Heard DW, Brochu M. Development of a nanostructure microstructure in the Al-Ni system using the electrospark deposition process. Journal of Materials Processing Technology 2010;210:892.

[21] Cadney S, Brochu M. Formation of amorphous Zr41.2Ti13.8Ni10Cu12.5Be22.5 coatings via the ElectroSpark Deposition process. Intermetallics 2008;16:518.

[22] Cadney S, Goodall G, Kim G, Moran A, Brochu M. The transformation of an Al-based crystalline electrode material to an amorphous deposit via the electrospark welding process. Journal of Alloys and Compounds;In Press, Corrected Proof.

[23] Spaepen F, Turnbull D. Crystallization Processes. In: Poate JM, Mayer JW, editors. Laser Annealing of Semiconductors. Academic Press Inc., 1982.

[24] Changjun C, Maocai W, Yiming L, Dongsheng W, Ren J. Mass transfer trends and the formation of a single deposition spot during high-energy micro-arc alloying of AZ31 Mg alloy. Journal of Materials Processing Technology 2008;198:275.

[25] Galinov IV, Luban RB. Mass transfer trends during electrospark alloying. Surface and Coatings Technology 1996;79:9.

[26] Lesnjak A, Tusek J. Processes and properties of deposits in electrospark deposition. Science and Technology of Welding and Joining 2002;7:391.
[27] Liu J, Wang R, Qian Y. The formation of a single-pulse electrospark deposition spot. Surface and Coatings Technology 2005;200:2433.
[28] Xie Y-j, Wang M-c. Microstructural morphology of electrospark deposition layer of a high gamma prime superalloy. Surface and Coatings Technology 2006;201:691.
[29] Xie Y-j, Wang M-c. Epitaxial MCrAlY coating on a Ni-base superalloy produced by electrospark deposition. Surface and Coatings Technology 2006;201:3564.
[30] Wang W-f, Wang M-c, Sun F-j, Zheng Y-g, Jiao J-m. Microstructure and cavitation erosion characteristics of Al-Si alloy coating prepared by electrospark deposition. Surface and Coatings Technology 2008;202:5116.
[31] Gayle F, Vander Sande J, McAlister A. The Al-Li (Aluminum-Lithium) system. Journal of Phase Equilibria 1984;5:19.
[32] Murray JL. The aluminium-copper system. International Metals Reviews 1985;30:211.
[33] Choi P-P, Al-Kassab T, Kirchheim R. Investigation of sputter-deposited Al–2at.%Cu layers by means of the tomographic atom probe (TAP). Scripta Materialia 2005;53:323.
[34] Rosenthal D. The Theory of Moving Sources of Heat and Its APplication to Metal Treatments. The American Society of Mechanical Engineers. Detroit, Michigan, 1946.
[35] Smith PM, Reitano R, Aziz MJ. Solute Trapping in Metals. Mat. Res. Soc. Symp. Proc., vol. 279: Materials Research Society, 1993.
[36] Dean JA, Lange NA. Lange's handbook of chemistry: McGraw-Hill, 1999.
[37] Pelton A. The Cu−Li (Copper-Lithium) system. Journal of Phase Equilibria 1986;7:142.
[38] Lieblich M, Torralba M. Cellular microstructure and heterogeneous coarsening of δ′ in rapidly solidified Al-Li-Ti alloys. Journal of Materials Science 1991;26:4361.
[39] Zimmermann M, Carrard M, Kurz W. Rapid solidification of Al-Cu eutectic alloy by laser remelting. Acta Metallurgica 1989;37:3305.
[40] Rioja R, Laughlin D. The early stages of GP zone formation in naturally aged Ai-4 wt pct cu alloys. Metallurgical and Materials Transactions A 1977;8:1257.
[41] Boettinger WJ, Coriell SR. Science and Technology Of The Undercooled Melt: Rapid Solidification Materials and Technologies. In: Sahm PR, Jones H, Adam CM, editors. 1986. p.81.
[42] Bolling GF, Tiller WA. Growth from the Melt. III. Dendritic Growth. Journal of Applied Physics 1961;32:2587.
[43] Baumann S, Williams D. Experimental observations on the nucleation and growth of δ′ (Al<sub>3</sub>Li) in dilute Al-Li alloys. Metallurgical and Materials Transactions A 1985;16:1203.
[44] Dai S, Yu G, Yan M. Nucleation and Formation of Stable and Metastable Phases in Undercooled Al-Li Melts. Journal of Materials Science and Technology 1993;9:190.
[45] Shao G, Tsakiropoulos P. Prediction of phase selection in rapid solidification using time dependent nucleation theory. Acta Metallurgica Materialia 1994;42:2937.

Appendix 6.1. Control Sample

A sample of AA2199 was solidified in an argon atmosphere, with a cooling rate of ~1K/s. The resulting microstructure is shown in Figure A1.1.

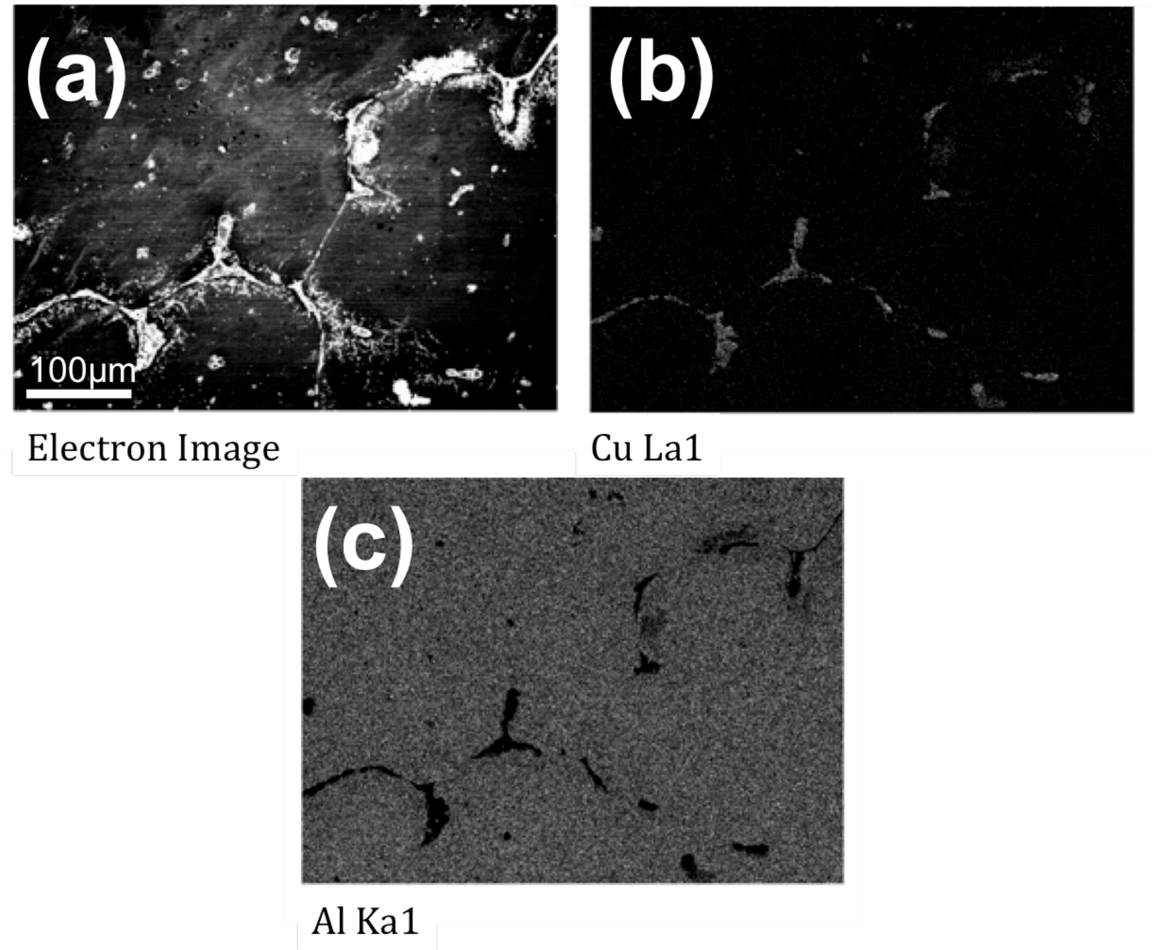

Figure 6-12- Electron micrograph (a) and EDS mapping of Cu (b) and Al (c) of equilibrium solidified AA2199 sample.

Appendix 6.2. Calculation of primary solidification phase during RSP.

The determination of phase selection was performed through the application of a time dependent nucleation model for RSP, as developed by Shao and Tsakiropoulos. The time required for nucleation was calculated using Equation A6.2-1.

$$\tau = \frac{7.2Rf(\theta)}{1-\cos(\theta)} \cdot \frac{a^4}{d_a^2 x_{L,eff}} \cdot \frac{T_r}{DS_m \Delta T_r^2}$$ (Equation A6.2-1)

Where is the nucleation time, R is the ideal gas-constant, $f(\theta) = 0.25[2 - 3cos\theta + cos^2\theta]$, θ is the wetting angle, a is the atomic jump distance, d_a is the average atomic diameter of the solid phase which has formed and is described using Equation A6.2-2. $x_{L,eff}$ is the effective alloy concentration, $T_r = T/T_m$, where T_m is the melting temperature of the solid phase, D is the diffusion coefficient, S_m is the molar entropy of fusion for the desired phase, $\Delta T_r = 1 - T_r$.

$$d_a = \left[\frac{\square m}{N_0 \rho}\right]^3$$ (Equation A6.2-2)

Where W_m is the average molar weight of the solid phase, N_0 is Avogadro's Number, and ρ is the density of the solid phase. As suggested in the original paper by Shao and Tsakiropoulos, the diffusion coefficient (D) was estimated using Stokes-Einstein relationship.

$$\frac{\eta D}{T} = \frac{k}{6d_{a,L}}$$ (Equation A6.2-3)

Where the k is the Boltzman constant, the viscosity (n) is calculated using $\eta = 10^{-3.3} exp\left[\frac{3.34T_L}{T-T_g}\right]$, where T_L and T_g are the liquidus temperature and ideal glass transition temperature of the solid phase, respectively.

7 Aging Response of a Rapidly Solidified Aluminum-Lithium Alloy[4]

7.1 Preface

As the RSP techniques employed resulted in a range of solidified structures, and the ultimate goal of the project was to assess the feasibility of the techniques to be used within a SFF process, the age hardening response was of interest. Similarly, as RSP has been determined to affect the aging behavior of metals, it was of interest to determine if the RSP techniques could potentially remove the necessity of a pre-aging cold-working process normally required during aging of Al-Li alloys.

7.2 Abstract

The natural and artificial age-hardening response of AA2199 rapidly solidified via Controlled-Short-Circuiting Metal-Inert-Gas (CSC-MIG) welding, Electrospark Deposition (ESD), and Laser Re-melting (LRM) was investigated. It was determined that the CSC-MIG deposited material displayed a low hardness in both the T1 condition and the T5 condition. This was determined to be due to the loss of lithium due to burn-out within the arc during deposition, as well as the result of the formation of a large volume fraction of a ternary eutectic phase during solidification. The ESD deposited material displayed a small amount of lithium burn-out, and therefore the T1 hardness suffered slightly. The T5 hardness of the ESD material however obtained a hardness of ~99HV, which is significantly less than the ~150HV of the T8' BM. It was determined that this was due to the lack of a cold-working process prior to aging. It was also revealed that the T1 hardness of the LRM material is similar to the T3 BM. It is therefore concluded that the LRM process is capable of producing SFF components of AA2199, which can achieve adequate hardness via a natural aging process, without requiring cold-working. Finally the LRM solidified material in the T5 condition was determined to be capable of

---

[4] To be submitted to The Journal of Materials Processing Technology

aging to 81% of the hardness (~122HV) of the BM in the T8' condition, without the application of a cold working process.

7.3 Introduction

Solid freeform fabrication (SFF), or additive manufacturing, is a near-net-shape process which offers aerospace manufacturers the ability to improve the buy-to-fly ratio by largely reducing scrap generation during manufacturing [1]. SFF has been traditionally performed using thermoplastics or resins for three-dimensional rapid prototyping applications [2]. The development of processes such as selective laser sintering (SLS) or Gas-Metal-Arc-Welding (GMAW) SFF has created the possibility of producing functional metallic components [3-7].

Aluminum-lithium (Al-Li) alloys are of interest to aerospace manufacturers as they offer a low density, high stiffness alternative to traditional aerospace materials [8]. While early generation (1st and 2nd gen.) Al-Li alloys suffered from anisotropic tensile behavior and low toughness [8], recent developments have resulted in the production of a third generation of Al-Li alloys such as the AA2199 alloy developed by Alcoa [9]. The AA2199 alloy, featuring a reduced lithium content (<2 weight percent), has addressed the undesirable properties of the previous generations through control of the microstructure and precipitates present via thermal-mechanical processing (TMP) and compositional changes [8]. As the AA2199 alloy is based on the AA2xxx series of age-hardenable alloys, the precipitation behavior of this alloy is vital to the strengthening of the alloy. The decomposition of a supersaturated solid solution (SSSS) within Al-Li alloys has been studied extensively [10, 11]. It has been shown that in binary Al-Li alloys the main strengthening phase is that of the metastable δ' phase (Al_3Li). Within Al-Cu-Li alloys, the ratio of the copper to lithium concentration has been shown to control the precipitation sequence [12]. The precipitation sequence of a high copper (3-5 wt%), low lithium (1-2 wt%) alloy has been shown to progress from the SSSS via the precipitation of δ' as well as the evolution of the θ' (Al_2Cu) phase [12]. A low copper (~2 wt%), high lithium (>2wt%) alloy has been shown to evolve via the co-precipitation of the δ' and T_1 phases (Al_2CuLi) [12]. As the majority of the copper within in the alloy is assumed to be incorporated into the T_1 phase, very little θ' is expected to form, and is therefore assumed to not contribute to strengthening of the alloy. Guimmarra et al. have proposed that the AA2199 alloy is strengthened by the δ', θ', and T_1 precipitates, as well as a modified version of the T_1 precipitate in which magnesium substitutes for lithium to form the S' phase (Al_2Cu,Li-Mg) [9]. However, a transmission electron microscopy (TEM) investigation of the AA2199 alloy in the T8E74 temper, by Steuwer et al., did not reveal the presence of the θ' or S' phases [13]. Instead it was determined that the T8E74 material mostly contained the T_1 phase, with a low volume fraction of δ' present. The high volume fraction of T_1 phase is of great significance within the AA2199 alloy, as the precipitate offers the largest strengthening potential [13]. This is because the T_1 phase is very effective at stopping slip within the matrix as the thin platelets form upon the [1 1 1] matrix planes [13, 14].

It has been shown previously that the formation of the δ' phase (Al_3Li) at grain boundaries (GB's) results in the localization of stresses and lowers the toughness of the material [15]. Similarly, in Al-Cu-Li-Zr alloys it has been determined that the formation of a thin film of the T_1 phase (Al_2CuLi) along GB's has also been associated with the poor toughness behavior of the alloy [16]. Cassada et al. have shown how the deformation or cold-working of aluminum-lithium alloys prior to aging resulted an increased volume fraction of precipitates and also promoted nucleation away from grain and subgrain boundaries through the increase of dislocation density [10]. Furthermore, Kaigorodova et al. have stated that the deleterious effects of the heterogeneous precipitation events can be minimized through the refinement of the microstructure [16]. As rapid solidification processing (RSP) has been shown to be capable of significantly refining the microstructures of aluminum alloys [17], and RSP techniques such as Controlled-Short-Circuiting Metal-Inert-Gas (CSC-MIG), Electrospark Deposition (ESD), and Laser Re-melting (LRM) have been shown to be capable of performing SFF, this study will investigate the aging response of AA2199 deposited via these three RSP techniques [18-20].

7.4 Experimental Methods

CSC-MIG deposited samples were fabricated using a JetLine Engineering CSC-MIG welding machine mounted on a Machitech XYZ automated table. The automated table was controlled using DeskCNC software by executing a G-code program. Welding trials were performed upon rectangular coupons of aluminum alloy 6061 with the dimensions 38 mm by 100 mm, and a thickness of 3.175 mm. The heat-input, measured via a real-time welding oscilloscope, of the CSC-MIG trials was ~ 60J/mm (1.5kJ/in).

ESD was performed using a TechnoCoat SparkDepo model 300 machine. Deposition was performed at a capacitance of 100 μF and a voltage of 100 V, resulting in a pulse energy of ~0.5 Joules, and a heat-input of ~1.5 J/mm. The standard applicator (rotational tool) was used with a rotational speed of ~500 rpm. A pulse frequency of 390 Hz was employed.

Laser re-melted samples were manufactured using a Miyachi LW25 micro-laser welding system mounted on a Machitech XYZ automated table. DeskCNC software was used to control the laser table. Laser re-melting was performed in an argon environmental chamber. Re-melting was performed on a 12.5 mm by 7.0 mm area, with a travel speed of 127 mm/min, a peak pulse energy of 0.125 Joules, a pulse frequency of 30 Hz, and a pulse duration of 0.5 ms, resulting in a heat-input of ~1.5 J/mm.

Scanning Electron Microscopy was performed using a Hitachi SU-8000 microscope, as well as a Hitachi 3400-N microscope. Samples were mounted in Bakelite and then ground using 320 grit SiC paper, polishing was then performed using 9, 3, and 1 μm diamond paste, and finished with 0.05 μm colloidal silica.

The composition of the AA2199 alloy used throughout this study is displayed in Table 7-1.

Table 7-1 - Composition of AA2199 in atomic percentage.

Element	Al	Li	Cu	Zn	Mg	Mn	Zr	Fe	Si
[at.%]	Bal.	5.3-6.8	1.0-1.2	0.1-0.4	0.05-0.4	0.1-0.5	0.1-0.4	0.03max	0.05max

The RSP samples were heat-treated in the as-solidified condition. Natural aging to the T1 condition was performed at room temperature, while artificial aging to the T5 condition was performed at 120 °C for 12 hours, before increasing to 160 °C for 24 hours, as this was determined to achieve peak-hardness within a previous study. Micro-Vickers hardness measurements were performed using 100 g-F for the CSC-MIG and ESD samples, and a 10 g-F load for the LRM samples, in accordance with ASTM standard E384.

For comparison purposes the hardness of the AA2199 alloy in the T3, or solutionized, cold-worked, and naturally aged condition, as well as the T8', or solutionized, cold-worked, and artificially aged condition, is shown.

7.5 Results and Discussions

The microstructures formed as a result of the three RSP techniques are displayed in Figure 7-1. It can be seen from Figure 7-1(a) that the CSC-MIG process resulted in the formation of a cellular morphology, with an average cell width of ~4.3 µm. This cellular morphology is accompanied by significant solute segregation, as noted by the presence of a copper rich inter-cellular phase (bright phase). The ESD solidified material shown in Figure 7-1(b) also reveals a cellular structure, however as a result of the lower heat-input of the ESD process, a higher solidification front velocity (SFV) was induced during solidification culminating in a significant refinement of the cells to a width of ~40nm. The material solidified via LRM as displayed in Figure 7-1 (c) displays a featureless microstructure. It was determined that this microstructure was the result of the SFV being greater than that required to maintain a stable planar solid-liquid interface.

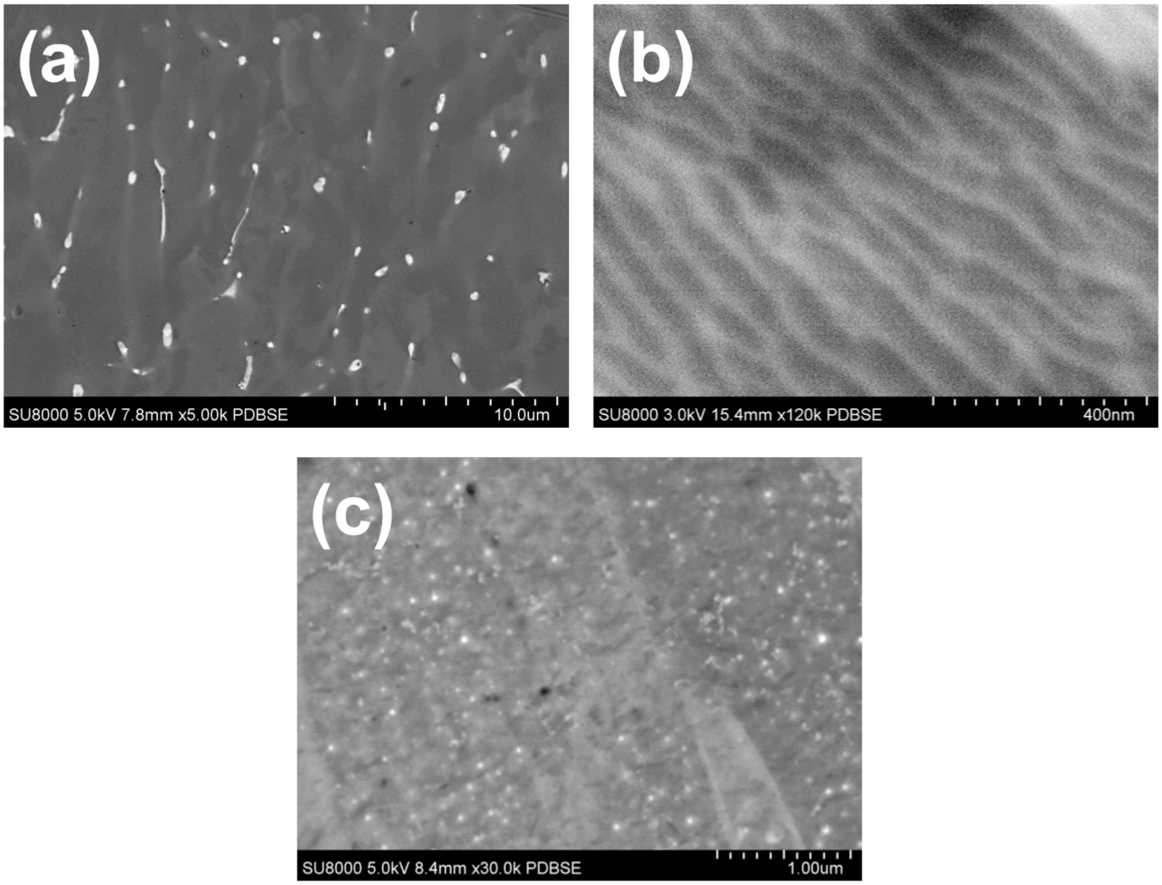

Figure 7-1- Microstructure of the rapidly solidified material in the as-deposited naturally aged (T1) condition produced via (a) CSC-MIG, (b) ESD, (c) LRM.

As the strengthening precipitates have been shown to heterogeneously precipitate upon grain boundaries it is customary to perform a cold working process prior to artificial aging of Al-Li-Cu alloys [10, 16]. The role of this cold-working is to increase the dislocation density within the material. It has been reported that this improves the strength of the heat-treated alloy by increasing the precipitate density, as well as promoting nucleation at sites other than grain boundaries (GB's), and therefore preventing the homogenization of slip during deformation [10]. However, as the purposed of this study is to investigate the applicability of the RSP techniques to SFF applications, the utilization of a cold-working process prior to aging is counterproductive to the near-net-shape processing advantage of SFF. Therefore throughout this study cold-working of the RSP material was not performed.

The aging response of the AA2199 solidified via CSC-MIG, ESD, and LRM is displayed in Figure 7-2. The hardness is reported in the T1, or as-solidified naturally aged condition, as well as the T5, or as-solidified and artificially aged, condition. It can be noted that the CSC-MIG solidified material displays the lowest T1 hardness of ~40HV, while the base-metal (BM) displayed a T3 hardness of ~90HV. Furthermore, while the CSC-MIG deposited material did respond to aging, the T5 hardness of ~90HV, is less than that noted by ESD and LRM processes, and significantly less than that noted for the T8' BM. This loss of hardness is believed to be due to the loss of lithium during deposition, as well due to the large fraction of ternary eutectic formed with respect to the other RSP techniques employed. As a Gas-Metal-Arc-Welding (GMAW) process, the CSC-MIG process involves the formation of an arc to facilitate heat transfer during deposition. Berzina et al. have previously revealed that lithium burn-out can occur within an electrical arc resulting in significant lithium depletion within GMAW deposited Al-Li alloys [21]. Wet chemical analysis of the CSC-MIG deposited material via atomic absorption revealed a residual lithium content within the deposited material of ~1.25 weight percent, an ~11% reduction. As lithium plays an important role in the formation of the strengthening precipitates, δ' and T_1, the reduction of lithium content would directly manifest as a loss of hardness. In addition to the lithium loss, the increased extent of inter-cellular eutectic phase present in the CSC-MIG deposited material (as evident in Figure 7-1) also has a negative effect on the aging response. As the solutes (lithium and copper) are essential to the formation of the strengthening precipitates, the increased volume fraction of inter-cellular ternary eutectic phase present within the CSC-MIG microstructure would reduce the amount of solute available for precipitate formation. A similar result was reported by Lippold during the study of the ageing behavior of commercial Al-Li welds [22]. Lippold reported that the formation of a solute rich eutectic phase deprived the surrounding Al matrix of solute, and therefore limited the aging potential of the weldment. While a solutionizing process prior to aging would be expected to dissolve this eutectic phase, the introduction of a pre-aging solutionizing process proved deleterious to the overall hardness. This phenomenon has also been reported and explained by Papzian et al. [23], and Fox et al. [24]. The previously mentioned authors have shown that the high diffusivity and reactivity of the lithium within the alloy result in significant lithium oxidation and surface depletion during solutionizing treatments, which culminates in a loss of microhardness of the alloy. Furthermore, as the goal of this research project is to investigate the ability of the RSP technique to produce a SFF component, solutionizing a component at temperature in excess of 500°C is assumed to be impractical.

The as-deposited naturally aged (T1) hardness of the ESD solidified material displays an increase in hardness with respect to the as-deposited CSC-MIG material, and is slightly lower than that obtained by the LRM process, as well as the T3 BM. This slight decrease is believed to be due to lithium burn-out as noted during CSC-MIG processing, as the ESD process involves the pulsing of a high frequency short-duration electrical arc between the electrode and the substrate. Wet chemical analysis then revealed a small amount of lithium depletion during deposition (<3%). It is therefore believed that this small loss of lithium, combined with the lack of cold-working prior to natural ageing, is responsible for the difference in hardness between the ESD T1 material and the T3 BM. The ESD material was shown to respond to aging, and a peak hardness of ~99HV was obtained in the T5 condition. This T5 hardness is greater than the T3 BM, while significantly less than the peak-aged T8' BM. Again, the T8' BM has been subjected to cold-working prior to aging. As the scope of this study is to investigate metal deposition processes capable of facilitating SFF, the inclusion of a cold-working process is impractical. However, Cassada et al. [10] and Rioja et al. [25] have shown that the cold-working of Al-Li alloys prior to artificial aging increases the dislocation density and ultimately the precipitate density, therefore resulting in an increased hardness with respect to non-cold-worked material.

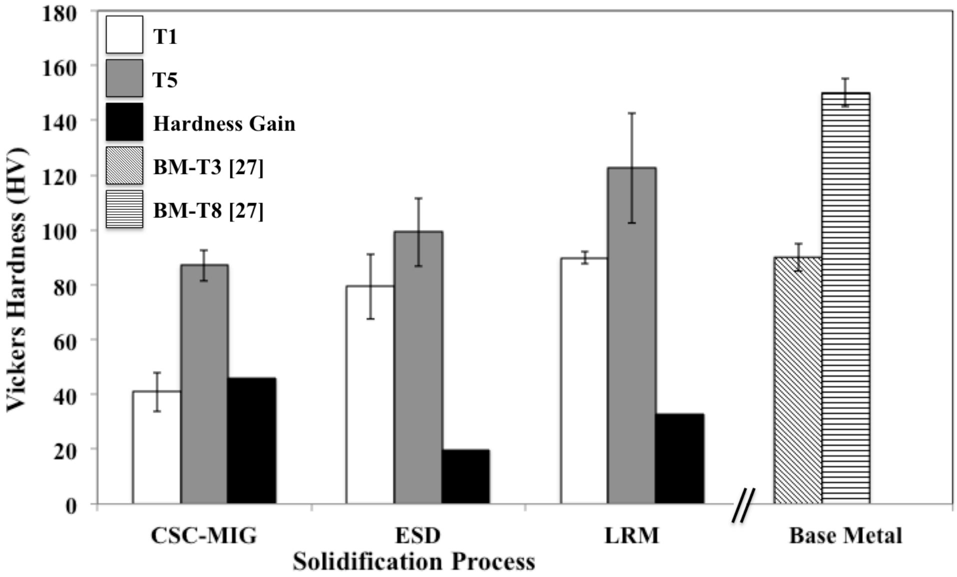

Figure 7-2- Aging response of various RSP techniques.

The T1 hardness of the LRM process can be seen to be greater than that resulting from the CSC-MIG and ESD processes. As LRM does not employ an electrical arc to transfer the heat necessary for melting, lithium burn-out was not an issue. It is also noted that the T1 hardness of the LRM material is comparable to that achieved by the BM in the T3 condition. This is of interest as the result supports the hypothesis that the LRM process removes the necessity of the cold-working process prior to natural aging, as experienced by the T3 BM. While the cold-working prior to aging has been shown to increase dislocation density during artificial aging as previously discussed, it has also proven efficacious during natural aging. Ringer et al. have shown that for an Al-Cu-Li alloy, stretching prior to natural aging resulted in a hardness increase of ~28HV [26]. Furthermore, the authors displayed that the Al-Cu-Li alloy experienced no natural aging without the pre-aging cold-working process being employed. The authors postulated that this was due to the low copper content of the alloy (~3 weight %, similar to the AA2199 alloy), a lack of free vacancies, or the lack of growth of the δ' phase (Al_3Li) formed during the quenching process [26]. A microstructural comparison of the T1 LRM and T3 BM structures is displayed in Figure 7-3. It can be seen that while the grain size of the material differs significantly, as to be expected due to the RSP, the precipitate density seems to be higher in the LRM material. As previously shown the super saturated solid solution (SSSS) induced during LRM solidification due to the extremely high SFV realized, produced a more homogenous solute distribution within the solidified material. It is then postulated that this homogeneous SSSS combined with the reduced grain size due to RSP, promoted nucleation of the precipitates. A similar phenomenon has been reported in rapidly solidified Al-Mn alloys. Shechtman et al. have shown that cells or subgrains formed during melt-spinning of an Al-Mn alloy, can serve as fast diffusion pathways for solute, increasing the coarsening rate during aging [27].

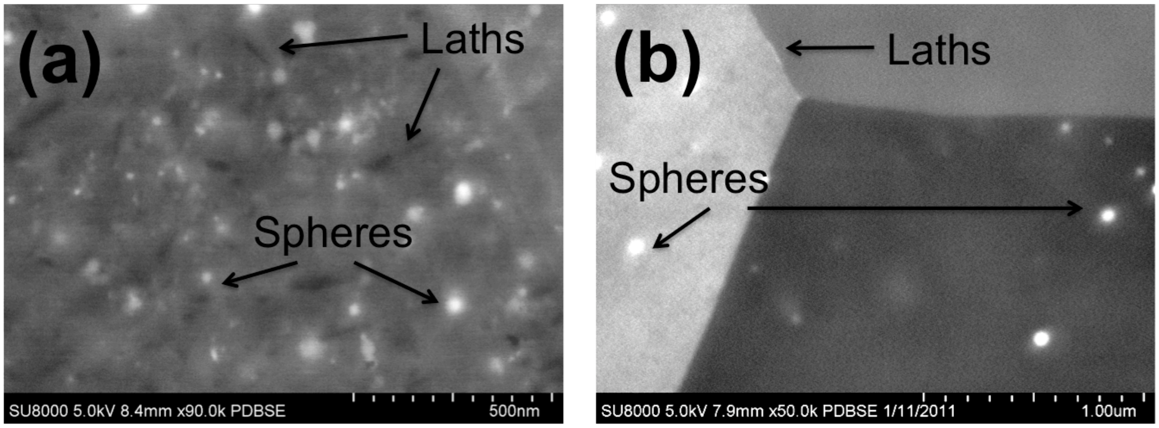

Figure 7-3- Back-scattered electron image of (a) LRM material in T1 condition, (b) T3 BM (courtesy of Rosen Ivanov [28]).

This is further supported by a microscopy analysis at the interface between the material re-solidified during LRM and the material that was not melted, as there is a small initial epitaxial growth region in which a fine cellular structure is present. Figure 7-4 displays a cell boundary from within this small initial cellular region, where ultra-fine circular precipitates can be seen to decorate the cell boundary, supporting the hypothesis of the cell network serving as a diffusion pathway for the solute.

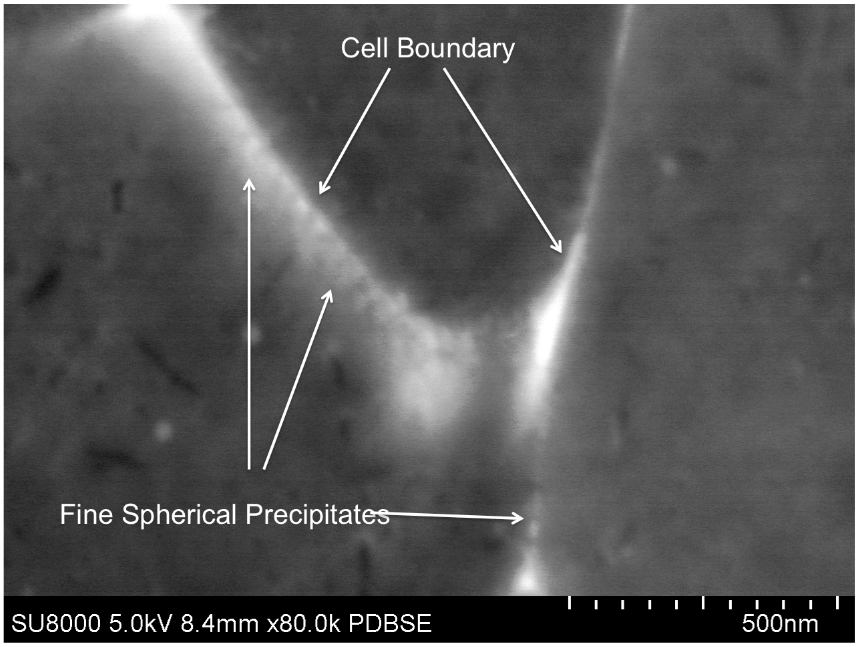

Figure 7-4- Initial cellular morphology within the LRM material displaying fine precipitates along the cell boundary.

The T5 hardness of the LRM material displays a hardness of ~122HV. While this represents a significant improvement over that of the CSC-MIG and ESD processes, it is approximately 30HV less than the T8' BM, accounting for ~81% of the hardness of the T8' BM. Again this is believed to be due to the lack of cold-working prior to aging. While the RSP is capable of producing a SSSS with homogeneous solute distribution, and the fine cellular structure is believed to increase the precipitate coarsening rate by enhancing diffusion, the lower dislocation density of the non-cold-worked material results in fewer nucleation sites available. The increased dislocation density as a result of cold-working has been shown to offer more nucleation sites, resulting in not only higher precipitate density, but also a decrease of the length of the plate-like T_1 (Al_2CuLi) precipitates [10]. Ringer et al. reported that stretching prior to artificial aging resulted in a hardness increase of ~20HV [26]. Furthermore, the authors reported that the time required to obtain peak-hardness during artificial aging was shortened from 200 hours in the non-stretched condition to 45 hours after cold-working. Analysis of the microstructure of the artificially aged LRM material and the BM in the T8' condition as displayed in Figure 7-5, revealed the differences in precipitate density and morphology.

It can be seen that the BM in the T8’ condition (Figure 7-5(b)) displays a higher density of precipitates, as well as the present of some large precipitates. Meanwhile the LRM T5 material looks similar to the T1 condition.

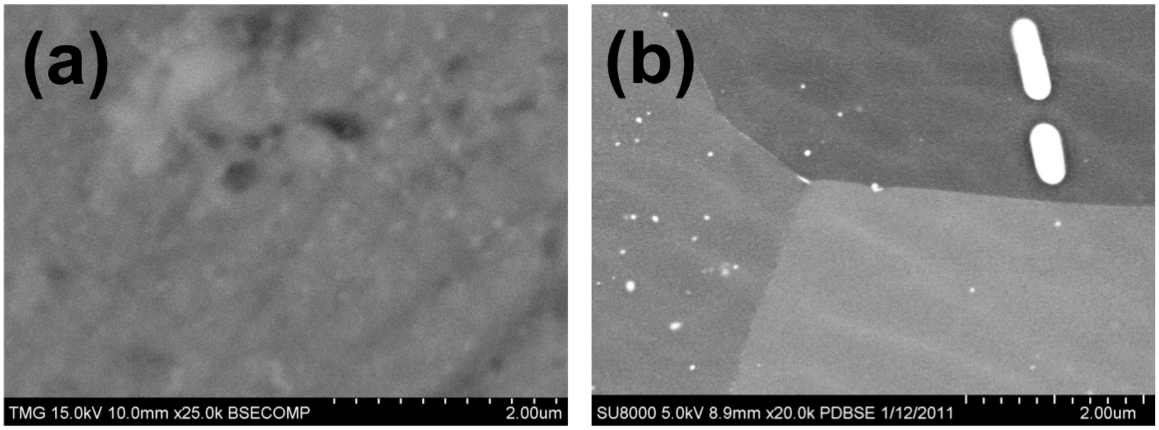

Figure 7-5 - Microstructure of the artificially aged (a) LRM material and (b) BM in the T8 condition (Courtesy of Rosen Ivanov)[28].

It was therefore determined that while the hardness of the RSP material in the T5 condition is less than that of the BM in the T8’ condition, due to the lack of cold-working performed, the LRM process is capable of producing a T1 hardness similar to that of the BM in the T3 condition. It is therefore postulated that the LRM process is capable of producing SFF components of AA2199, which can achieve adequate hardness via a natural aging process, without requiring cold-working.

7.6 Conclusions

It was determined that the CSC-MIG deposited material displayed a low hardness in the T1 condition and the T5 condition. This was determined to be due to the loss of lithium due to burn-out within the arc during deposition, as well as the result of the formation of a large volume fraction of a ternary eutectic phase. The ESD deposited material displayed a small amount of lithium burn-out, and therefore the T1 hardness suffered slightly. The T5 hardness of the ESD material however obtained a hardness of ~99HV, which is significantly less than the ~150HV of the T8’ BM. It was determined that this was due to the lack of a cold-working process prior to aging. It was also revealed that the T1 hardness of the LRM material is similar to the T3 BM. It is therefore concluded that the LRM process is capable of producing SFF components of AA2199, which can achieve adequate hardness via a natural aging process, without requiring cold-working. Finally the LRM solidified material in the T5 condition was determined to be capable of aging to 81% of the hardness (~122HV) of the BM in the T8' condition, without the application of a cold working process.

7.7 Acknowledgments

The authors would like to acknowledge the support of the Natural Science and Engineering Research Council of Canada (NSERC), the McGill University Engineering Doctoral Award (MEDA) as well as that from the Regroupement Aluminum Research Centre (REGAL). The authors would also like to acknowledge the technical assistant of Mr. Nicolas Brodusch, Rosen Ivanov, and Mr. Mazen Samara.

7.8 References

[1] Almeida PMS, Williams S. Innovative process model of Ti-6Al-4V additive later manufacturing using cold metal transfer (CMT). Solid freeform fabrication symposium, 2010.
[2] Pham DT, Gault RS. A comparison of rapid prototyping technologies. International Journal of Machine Tools and Manufacture 1998;38:1257.
[3] Horrii T, Kirihara S, Miyamoto Y. Freeform fabrication of superalloy objects by 3D micro welding. Materials & Design 2009;30:1093.
[4] Jandric Z, Labudovic M, Kovacevic R. Effect of heat sink on microstructure of three-dimensional parts built by welding-based deposition. International Journal of Machine Tools and Manufacture 2004;44:785.
[5] Mughal M, Fawad H, Mufti R. Finite element prediction of thermal stresses and deformations in layered manufacturing of metallic parts. Acta Mechanica 2006;183:61.
[6] Sheng Z, Chao L, Can-duo S, Jian L. Microstructure and Micro Mechanical Property of Part Formed by GMAW Surfacing Rapid Prototyping. Key Engineering Materials 2010;419-420:853.

[7] Wang Z, Guan K, Gao M, Li X, Zeng X. Tensile properties of 304 stainless steel fabricated by selective laser melting. Optical Society of America, 2012. p.MF1B.4.

[8] Rioja R, Liu J. The Evolution of Al-Li Base Products for Aerospace and Space Applications. Metallurgical and Materials Transactions A 2012:1.

[9] Giummarra C, Thomas B, Rioja RJ. NEW ALUMINUM LITHIUM ALLOYS FOR AEROSPACE APPLICATIONS. Proceedings of the Light Metals Technology Conference 2007 2007.

[10] Cassada WA, Shiflet GJ, Starke EA. The effect of plastic deformation on Al2CuLi (T 1) precipitation. MTA 1991;22:299.

[11] Gayle FW, Heubaum FH, Pickens JR. Structure and properties during aging of an ultra-high strength Al-Cu-Li-Ag-Mg alloy. Scripta Metallurgica et Materialia 1990;24:79.

[12] Lavernia EJ, Grant NJ. Aluminium-lithium alloys. Journal of Materials Science 1987;22:1521.

[13] Steuwer A, Dumont M, Altenkirch J, Birosca S, Deschamps A, Prangnell PB, Withers PJ. A combined approach to microstructure mapping of an Al–Li AA2199 friction stir weld. Acta Materialia 2011;59:3002.

[14] da Costa Teixeira J, Cram DG, Bourgeois L, Bastow TJ, Hill AJ, Hutchinson CR. On the strengthening response of aluminum alloys containing shear-resistant plate-shaped precipitates. Acta Materialia 2008;56:6109.

[15] Lavernia EJ, Srivatsan TS, Mohamed FA. Strength, deformation, fracture behaviour and ductility of aluminium-lithium alloys. Journal of Materials Science 1990;25:1137.

[16] Kaigorodova LI, Pushin VG, Rasposienko DY, Pilyugin VP. Effect of severe plastic deformation on the formation of the nanocrystalline structure and the aging of the multicomponent aluminum-lithium alloy with small additions of Sc and Mg. Phys. Metals Metallogr. 2011;111:72.

[17] Lavernia EJ, Ayers JD, Srivatsan TS. Rapid solidification processing with specific application to aluminium alloys. International Materials Reviews 1992;37:1.

[18] Heard DW, Brophy S, Brochu M. Solid freeform fabrication of Al-Si components via the CSC-MIG process. Canadian Metallurgical Quarterly 2012;51:302.

[19] Brochu M, Heard DW, Milligan J, Cadney S. Bulk nanostructure and amorphous metallic components using the electrospark welding process. Assembly Automation 2010;30:248.

[20] Brandl E, Palm F, Michailov V, Viehweger B, Leyens C. Mechanical properties of additive manufactured titanium (Ti–6Al–4V) blocks deposited by a solid-state laser and wire. Materials & Design 2011;32:4665.

[21] Berzina IG, Gusev EB, Ivanov VA, Lukin VI. Investigation of Li distribution in aluminium alloy welds by elemental radiographic analysis. International Journal of Radiation Applications and Instrumentation. Part D. Nuclear Tracks and Radiation Measurements 1992;20:261.

[22] Lippold JC. Ageing behaviour of commercial aluminium-lithium welds. Journal of Materials Science 1995;30:4155.

[23] Papazian J, Schulte R, Adler P. Lithium depletion during heat treatment of aluminum-lithium alloys. Metallurgical and Materials Transactions A 1986;17:635.

[24] Fox S, Flower HM, McDarmaid DS. Oxidation induced solute depletion in Al-Cu-Mg-Li alloys. Scripta Metallurgica 1986;20:71.

[25] Rioja RJ, Bretz PE, Sawtell RR, Hunt WH, Ludwiczak EA. Int. Conf. on Aluminum Alloys, vol. III: Chameleon Press, London, 1986. p.1781.
[26] Ringer S, Muddle B, Polmear I. Effects of cold work on precipitation in Al-Cu-Mg-(Ag) and Al-Cu-Li-(Mg-Ag) alloys. Metallurgical and Materials Transactions A 1995;26:1659.
[27] Shechtman D, Schaefer RJ, Biancaniello FS. Precipitation in rapidly solidified Al-Mn alloys. MTA 1984;15:1987.
[28] Ivanov R. The effects of friction stir welding on the mechanical properties and microstructure of a third generation Al-Li alloy. Mining and Materials Engineering, vol. Master of Applied Science (Thesis): McGill University, 2012.

8 General Discussion

The extent of solute segregation that occurs during solidification is a function of the solidification parameters including; thermal gradient (*G*), cooling-rate (*dT/dt*), and SFV. As shown by Aziz when a solid-liquid interface is advanced at a rate which is greater than the diffusive speed of a given solute, then the solute atom is engulfed, or entrapped within the growing solid [1]. Therefore RSP offers the ability to reduce or completely remove microsegregation effects, and ultimately the necessity of secondary TMP for homogenization [2]. Furthermore, deposition-based RSP techniques such as CSC-MIG, LRM, and ESD have been shown to be capable of performing SFF. SFF processing offers aerospace manufacturers the ability to drastically improve the buy to fly ratio, as subsequent machining processes and ultimately scrap production is minimized by the near-net-shape fabrication technique. As the application of a near-net-shape fabrication technique removes the ability to perform cold-work (i.e. deformation) to the component, which is traditionally applied for Al-Li alloy components [3, 4] the ability to induce featureless solidification via RSP techniques is of utmost importance.

The objective of this study was to investigate the feasibility of several RSP techniques to deposit AA2199 in a manner in which equilibrium segregation of the solute was avoided. As previously discussed, non-equilibrium partitioning may be accomplished through the rapid progress of the solid-liquid interface. The CGM of Aziz predicts that at a SFV greater than ~10^{-2}m/s deviations from equilibrium with respect to solute partitioning of both copper and lithium within aluminum begins to occur. Furthermore, Spaepen and Turnbull have stated that a process in which the thermal decay profile obtains an ambient temperature at a distance less than 60μm in pure materials or ~1mm in metal alloys from the heat source, then interfacial attachment kinetics become important [5]. As the end goal of this project was to determine if a given technique is capable of allowing the SFF of standalone components, RSP techniques which have been previously shown to be proficient in SFF applications were investigated. These processes included, CSC-MIG welding, LRM, and ESD. A comparison of the approximate deposition rate for each process investigated within this study is shown in Figure 8-1. It is noted that while the CSC-MIG process is capable of rather high deposition rates, on the order of several kilograms per hour, the LRM and ESD processes display significantly lower deposition rates below a kilogram per hour. This is directly related to the relative heat-input of each individual process, shown in Figure 8-2. It can be seen that the CSC-MIG process involved the highest heat-input, while the LRM and ESD processes employed a significantly lesser heat-input.

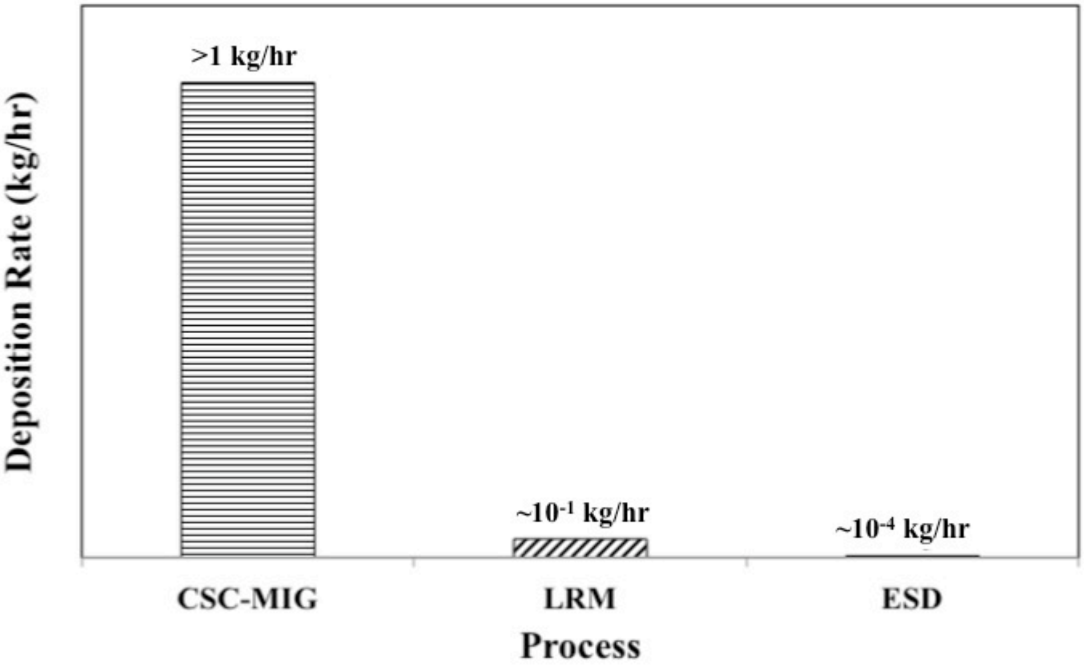

Figure 8-1 - Approximate deposition rate comparison for individual processes used throughout this study.

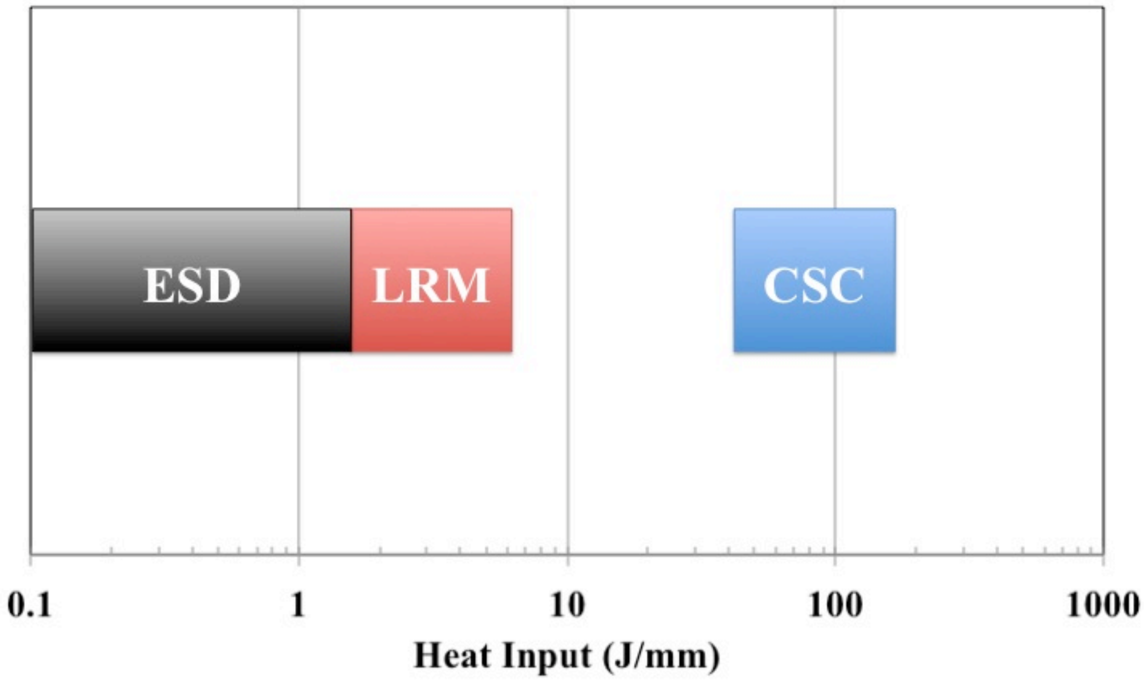

Figure 8-2- Heat-input comparison for individual RSP techniques employed in this study.

Cahn has stated that when the driving force for solidification is high, a crystal grows via the continuous mechanism [6]. Furthermore Cahn presented an equation to estimate the SFV in the continuous growth regime.

$$SFV = \frac{\beta}{a}\left(\frac{D}{RT}\right)\left(L\frac{\Delta T}{T}\right) \qquad \text{(Equation 8-1)}$$

Where β is a geometric factor, a is the interatomic distance, D is the liquid self-diffusion coefficient, R is the ideal gas constant, T is the temperature, L is the latent heat of fusion per unit volume, and ΔT is the tip undercooling. It can be seen therefore that the interface mobility is described by the $\left(\frac{D}{RT}\right)$ term, while the $\left(L\frac{\Delta T}{T}\right)$ term represents the driving force. This would therefore imply that an increase in the undercooling, would result in an increase in the SFV. Flood and Hunt have shown that increasing the cooling-rate results in an increase in thermal gradient, and therefore an increase the SFV realized [7]. As the cooling-rates and thermal gradients of LRM and ESD are higher than that realized during CSC-MIG solidification, it was expected that these processes would induce a higher SFV.

A comparison of the microstructures formed during RSP of the AA2199 material via CSC-MIG, LRM, and ESD are shown in Figure 8-3 (a-d).

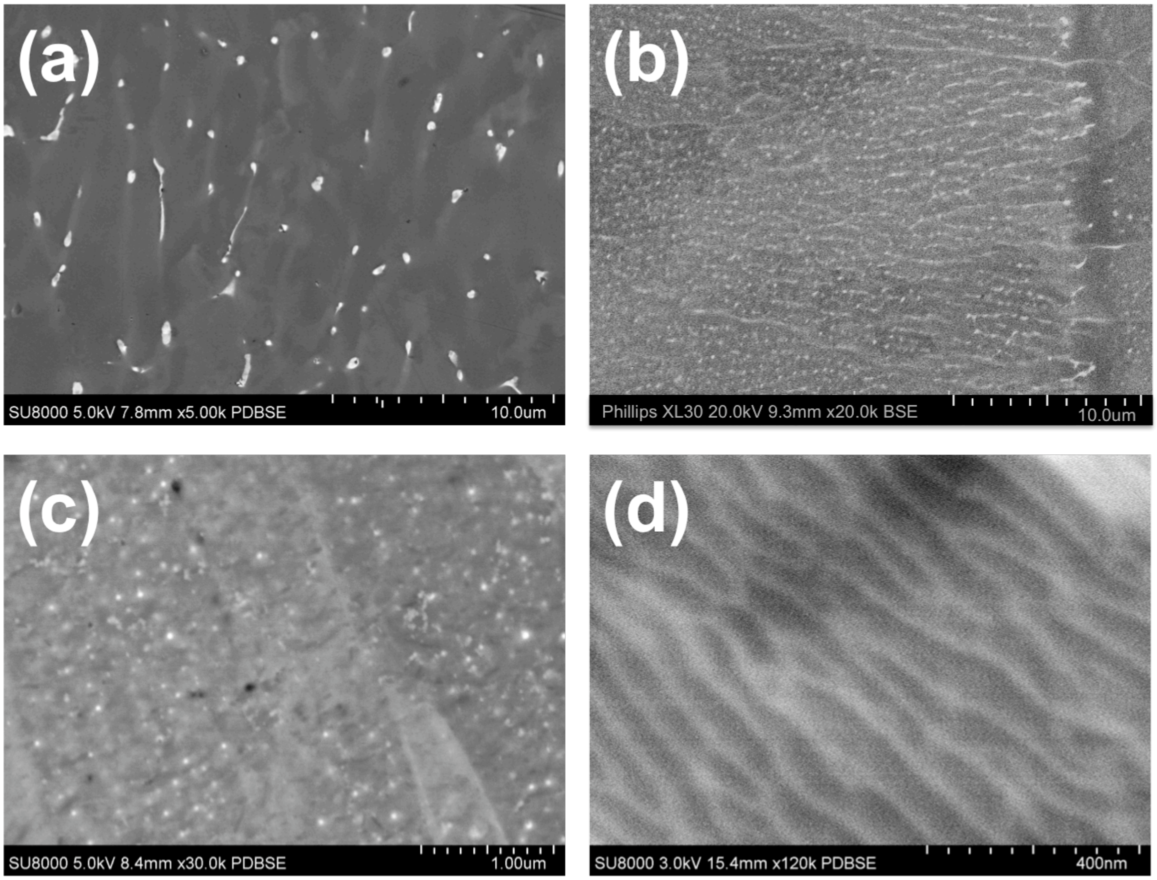

Figure 8-3- SEM images displaying the microstructure of the material deposited using the various RSP techniques. (a) CSC-MIG, (b) LRM with 0.5J Pulse-energy, (c) LRM with 0.125J pulse energy, (d) ESD

It can be seen that the CSC-MIG, LRM (with a pulse energy>0.125J), and ESD processing routes resulted in the formation of a cellular structure except for the LRM sample re-melted with a pulse energy of 0.125J (HI=1.5J/mm), which will be discussed in detail later. A summary of the cell size realized with respect to heat-input is shown in Figure 8-4. The CSC-MIG solidified sample displayed the largest cell size of ~4.3 ±1μm. This is to be expected as the dendrite arm spacing or cell width is directly related with the growth rate and thermal gradient [8]. The high heat-input of the CSC-MIG process (HI=60J/mm) with respect to LRM and ESD, should result in a lower thermal gradient being achieved. The LRM sample solidified with a pulse energy of 0.5J (HI=6.02J/mm) displayed a cell size of ~320 ±27nm, while the ESD solidified material (1.5J/mm) displayed a very fine cell size of ~40 ±5nm. It should be noted that while the cell size as a function of heat-input relationship appears linear on a log-log plot, this relationship only holds true within the cellular forming region. Therefore as absolute stability is predicted at a SFV greater than 1m/s, and initial cellular breakdown is predicted to correlate to a cell-size of ~40nm, this plot cannot be used to extrapolate information below a cell-size of ~40nm.

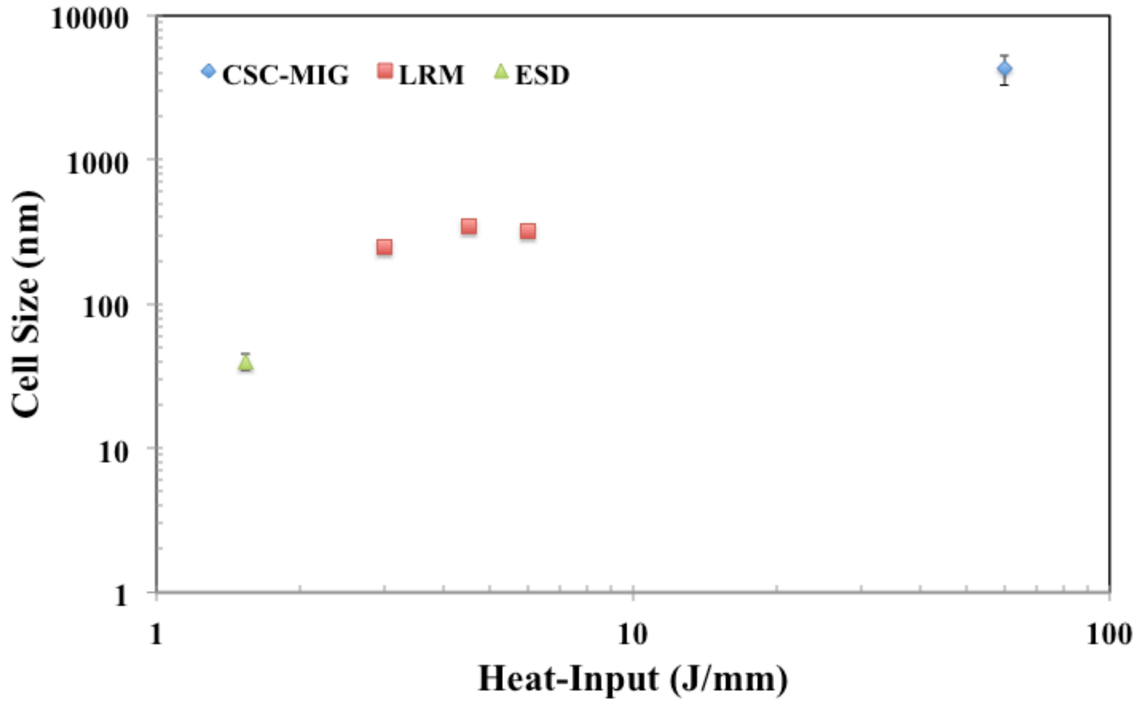

Figure 8-4- Measured cell size as a function of the heat-input for the material deposited using CSC-MIG, LRM, and ESD.

As the heat-input of the CSC-MIG process is so much larger than the LRM and ESD it can be assumed that the thermal gradient of the CSC-MIG process is significantly less than that of the LRM and ESD processes, therefore resulting in a coarsening of the cellular structure. Furthermore it can be noted that the heat-input of the LRM process varies, depending on pulse energy from ~6 – 1.5J/mm, the lowest being similar to that of the ESD process. This concurs with the SEM and cell-size analysis which displayed a larger cell structure within the high-energy LRM samples.

As previously mentioned it was noted that when the LRM technique was performed with a low pulse energy resulting in a heat-input of ~1.5J/mm the cellular morphology is not present. This is indicative of a planar solidification front being realized during solidification. However, when the ESD process was performed with a similar heat-input of ~1.5J/mm, cellular breakdown occurred. The reason for this discrepancy is believed to be due to the limitation of heat-transfer at the splat interface. Shingu and Ozaki have shown that if the contact between the deposited material, in a splat cooling system similar to that of ESD, and the substrate is not ideal, then the solidification rate is limited by the heat-flow across this interface [9]. In comparison, Boettinger et al. have stated that as LRM experiments involve the metal being melted in direct contact with itself, the knowledge of heat-transfer coefficient is not required as the contact is assumed to be continuous and consistent [10]. It is therefore postulated that the intimate contact between the re-melted region and the substrate (heat-sink) promotes a more efficient heat-extraction, than that occurring between the deposited material (splat) and substrate (heat-sink) during ESD.

Throughout this study the KGT model for microstructural evolution during rapid solidification was employed to estimate the SFV realized during RSP. It should be noted that the KGT model predicts that the thermal gradient may have an effect of the SFV, however the thermal gradients displayed little effect on the dendrite tip radius (or cell spacing) realized at high SFV values. The calculated SFV was then used within the Continuous Growth Model (CGM) of Aziz to determine the extent of the deviation from equilibrium partition occurring at the solid-liquid interface. The study then aimed to validate the predicted non-equilibrium partitioning values by experimentally measuring the solute distribution within the solidified material. As the RSP technique selected for the study represented a range of heat-inputs and thermal gradients, it was hypothesized that the cell size and ultimately SFV would scale with the heat-input. The relationship between the dendrite tip radius (cell spacing) and SFV is shown in Figure 8-5. This figure is annotated to display the cell spacing measured for each RPS technique employed, as well as the resulting SFV. The resulting SFV as a function of the heat-input of the specific process is shown in Figure 8-6.

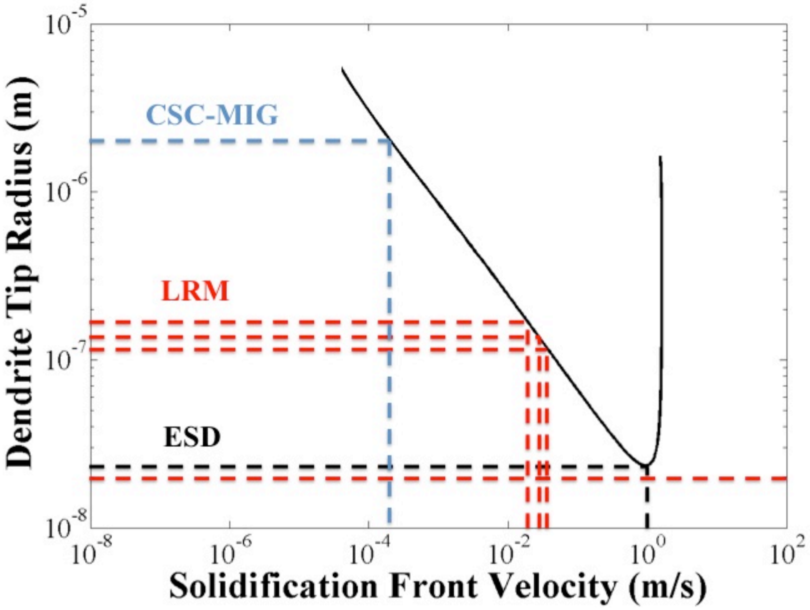

Figure 8-5- Dendrite tip radius (cell spacing) vs. SFV as calculated from the KGT model, displaying the measured cell spacing reported for the various techniques employed and their correlating SFV values.

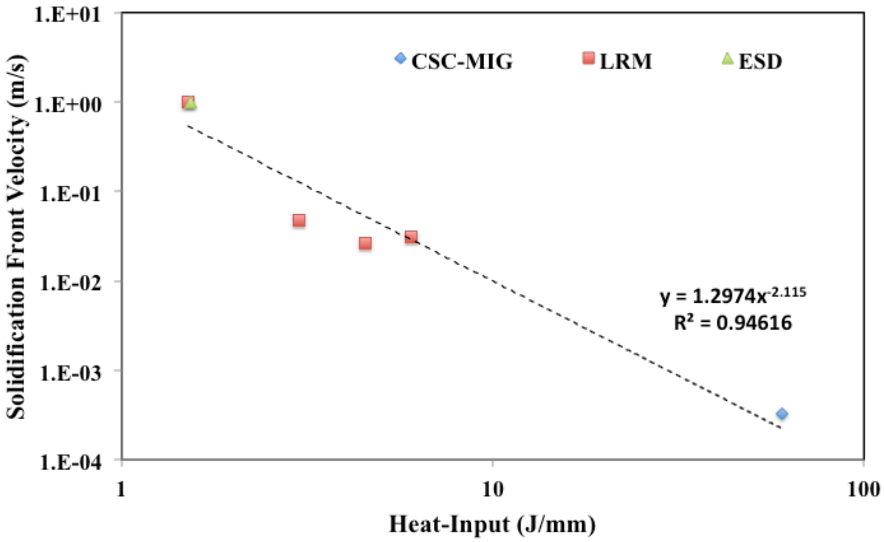

Figure 8-6- SFV as a function of the Heat-Input for each RSP technique investigated.

It can be seen that the CSC-MIG process resulted in the lowest SFV. This is to be expected as the process also displayed the lowest thermal gradient and cooling rate, and the highest heat-input. The LRM processing resulted in a range of SFV values between 3 cm/s and greater than 1m/s, depending on the laser energy employed. The lowest pulse energy employed during the LRM experiments, 0.125J, resulted in featureless solidification morphology indicative of a planar solid-liquid interface being realized during solidification. This was similar to that realized during the ESD solidification, in which the transition from a planar to cellular morphology was noted. It can therefore be determined that the LRM technique, when operated under the pulse energy of 0.125J, is comparable to that of the ESD technique. This is believed to occur because although the ESD process was performed with a pulse energy of 0.5J, significantly greater than that of the LRM process, the shorter pulse duration results in a very comparable heat-input to the system.

These SFV values were then correlated with an approximate effective partition coefficient through the application of the CGM. The effect of SFV on the equilibrium partition coefficient of Li and Cu within Al is displayed within Figure 8-7, the ranges of SFV calculated for each process are also shown within the figure.

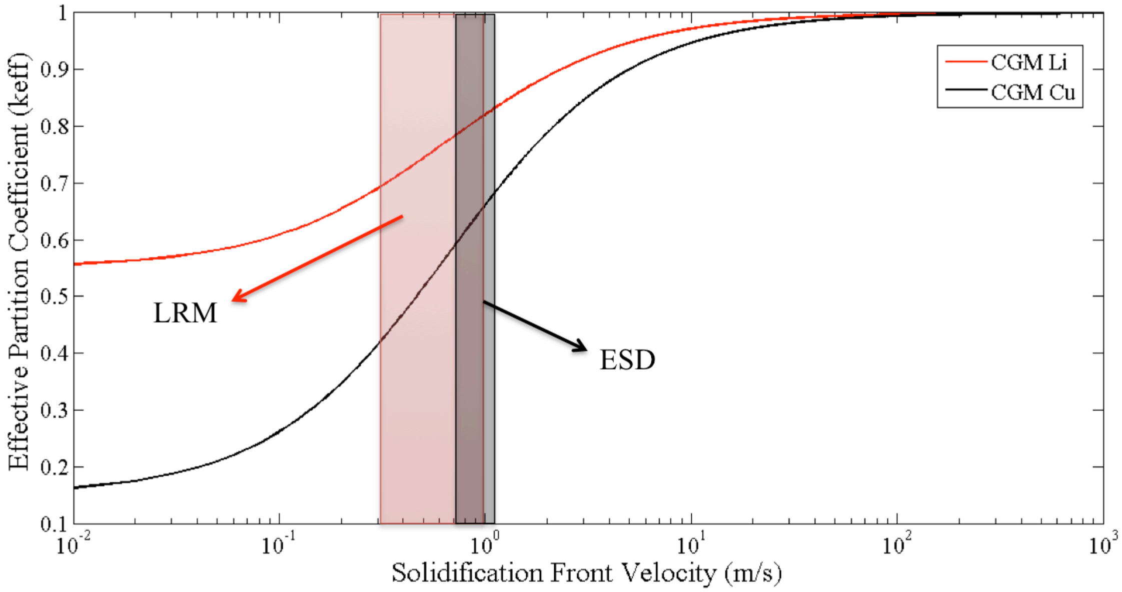

Figure 8-7- The range of effective partition coefficient values for each RSP technique employed as calculated using the CGM.

It can be noted that the SFV induced by the CSC-MIG process (~1-4x10^{-3}m/s) is not significant enough to induce a deviation from equilibrium partitioning. In fact the SFV realized during CSC-MIG solidification is not high enough to allow for the CSC-MIG process to be properly classified as RSP. Both the LRM and ESD processes however display significant deviations from equilibrium partitioning during solidification. This was then supported by the chemical profiling data, which displayed relatively homogeneous distributions of the solute in the lowest heat-input LRM sample as well as the ESD sample. Depth profile analysis of the solute distribution within the CSC-MIG samples, as performed by TOF-SIMS analysis, revealed a reasonably homogeneous distribution of Li and Cu throughout the growth direction. However lateral distribution analysis revealed areas of enriched copper content. This was supported by the EDS analysis performed, which revealed the presence of a copper rich phase in the inter-cellular region. This was postulated to be the T_2 (Al_6CuLi_3) phase, as predicted by ternary solidification path analysis. The chemical profiling of the LRM samples displayed a decrease in solute segregation with a decrease in laser energy (heat-input). It was determined that the low energy LRM trials with a heat-input of ~1.5J/mm resulted in minimal lithium segregation, as the depth profile was similar to that of the parent "control" material. As with the CSC-MIG samples, the inter-cellular material was determined to be copper rich in the LRM samples that displayed a cellular structure. This is indicative of lateral segregation occurring to stabilize the cellular morphology as discussed by Bolling and Hunt [11]. Similarly the ESD solidified material display minimal solute enrichment along the solidification direct, as measured via TOF-SIMS depth profiling, however the inter-cellular material was determined to be copper rich via EDS and APT analysis. Furthermore the ATP analysis revealed the presence of lithium clusters decorating the cellular morphology. These lithium clusters were determined to be stoichiometric Al_3Li (δ'). It was therefore determined through the application of a time dependent nucleation model for phase suppression during RSP developed by Shao and Tsakiropoulos [12] that the cellular morphology formed initially during solidification, and then the Al_3Li phase heterogeneously nucleated upon the cell walls. This is similar to what Cassada et al. have reported for the T_1 precipitate during the aging of Al-Li alloys without a cold-working process prior to aging [13]. Lieblich and Torralba reported a similar heterogeneous coarsening of Al_3Li upon a cellular structure formed during the RSP of an Al-Li-Ti alloy [14]. As it was postulated that the formation of a featureless microstructure, such as that formed within the low pulse energy LRM samples, would reduce or remove the occurrence of heterogeneous nucleation, resulting in the full recovery of hardening potential of the deposited material, the aging response to natural and artificial ageing was investigated.

It was revealed that the CSC-MIG solidified material displayed a low hardness in the naturally aged (T1) and artificially aged (T5) conditions. Wet-chemical analysis of the deposited material revealed that significant burn-out had occurred during CSC-MIG deposition, and resulted in the loss of ~11% lithium from the deposited material. As the lithium plays an important role in the strengthening precipitates of the AA219 alloy, δ' (Al_3Li) and T_1 (Al_2CuLi), a reduction of lithium would result in a reduction of the strengthening precipitates during ageing. Furthermore, CSC-MIG solidified material display a large volume fraction of a inter-cellular ternary eutectic phase. As the ternary eutectic phase would then essentially tie-up the solute required to form the strengthening precipitates, the fraction of precipitates and ultimately the hardness was reduced.

Atomic absorption analysis revealed that the ESD solidified material also displayed a small amount of lithium burn-out. As a result the T1 and T5 hardness was slightly lower than that of the T3 and T8' base-metal (BM). It was noted that the hardness difference between the ESD solidified and the T8' BM was greater than that of the ESD material in the T1 condition and the T3 BM. It was believed that this was due to the lack of a cold-working process prior to ageing.

Finally it was determined that the T1 hardness of the LRM material was very comparable to that of the T3 BM. This is of interest as it has been previously shown by Ringer et al. that the cold-working of an Al-Cu-Li alloy was essential to impart a natural aging response [15]. It was postulated that the natural aging response induced within the LRM material was the result of the reduced grain size due to RSP. It has been shown by Schechtman et al. that a fine substructure can promote precipitate nucleation in an rapidly solidified Al-Mn alloy, by serving as a diffusion pathway within the microstructure [16].

It is postulated that a similar phenomenon is occurring within the LRM solidified material, resulting in an increased precipitate density with respect to the T3 BM. The T5 hardness of the LRM solidified material was determined to reach ~122HV, or 81% of the hardness of the BM in the T8' condition. Again the hardness discrepancy between the LRM material and BM is believed to be due to the lack of a cold working process.

It is therefore concluded that the LRM process is capable of producing SFF components of AA2199, that can be naturally aged to achieve adequate hardness without the application of a solutionizing treatment or a cold-working process. This implies that the LRM-SFF process would be ideal for remote site fabrication of components such as that required for the SFF of a lunar base, as proposed recently by the European Space Agency [17].

8.1 References

[1] Aziz MJ. Model for solute redistribution during rapid solidification. Journal of Applied Physics 1982;53:1158.
[2] Boettinger WJ, Coriell SR, Sekerka RF. Mechanisms of microsegregation-free solidification. Materials Science and Engineering 1984;65:27.
[3] Rioja R, Liu J. The Evolution of Al-Li Base Products for Aerospace and Space Applications. Metallurgical and Materials Transactions A 2012:1.
[4] Rioja RJ. Fabrication methods to manufacture isotropic Al-Li alloys and products for space and aerospace applications. Materials Science and Engineering: A 1998;257:100.
[5] Spaepen F, Turnbull D. Crystallization Processes. In: Poate JM, Mayer JW, editors. Laser Annealing of Semiconductors. Academic Press Inc., 1982.
[6] Cahn JW, Hillig WB, Sears GW. The molecular mechanism of solidification. Acta Metallurgica 1964;12:1421.
[7] Flood SC, Hunt JD. Columnar and equiaxed growth: II. Equiaxed growth ahead of a columnar front. Journal of Crystal Growth 1987;82:552.
[8] Trivedi R, Kurz W. Dendritic growth. International Materials Reviews 1994;39:49.
[9] Shingu P, Ozaki R. Solidification rate in rapid conduction cooling. MTA 1975;6:33.
[10] Boettinger W, Shechtman D, Schaefer R, Biancaniello F. The Effect of Rapid Solidification Velocity on the Microstructure of Ag-Cu Alloys. Metallurgical and Materials Transactions A 1984;15:55.
[11] Bolling GF, Tiller WA. Growth from the Melt. Part II. Cellular Interface Morphology. Journal of Applied Physics 1960;31:2040.
[12] Shao G, Tsakiropoulos P. Prediction of phase selection in rapid solidification using time dependent nucleation theory. Acta Metallurgica Materialia 1994;42:2937.

[13] Cassada WA, Shiflet GJ, Starke EA. The effect of plastic deformation on Al2CuLi (T 1) precipitation. MTA 1991;22:299.

[14] Lieblich M, Torralba M. Cellular microstructure and heterogeneous coarsening of δ′ in rapidly solidified Al-Li-Ti alloys. Journal of Materials Science 1991;26:4361.

[15] Ringer S, Muddle B, Polmear I. Effects of cold work on precipitation in Al-Cu-Mg-(Ag) and Al-Cu-Li-(Mg-Ag) alloys. Metallurgical and Materials Transactions A 1995;26:1659.

[16] Shechtman D, Schaefer RJ, Biancaniello FS. Precipitation in rapidly solidified Al-Mn alloys. MTA 1984;15:1987.

[17] ESA. Building a lunar base with 3D printing. vol. 2013. http://www.esa.int: Eurpoean Space Agency, 2013.

9 Conclusions

This section contains a summary of the conclusions presented in previous chapters as displayed:

Conclusions from Chapter 4:

1) The low heat-input of the CSC-MIG process combined with the high thermal conductivity of the aluminum alloy workpiece resulted in a high cooling-rate during deposition on the order of 840 - 3500 °C/s being realized. The solidification time was determined to range between 2-5ms depending on the position within the weldment.

2) A fine (4.3 ±1 μm) cellular structure was formed within the deposited material. Through comparison with the KGT model for microstructural development during solidification the SFV of the CSC-MIG process was estimated to be ~$2\text{-}4.5\times10^{-4}$m/s.

3) Chemical analysis via EDS and TOF-SIMS revealed lateral segregation of copper to the cell walls, and a similar segregation profile to that predicted by the Clyne-Kurz model. TOF-SIMS revealed a homogeneous lateral lithium distribution, however depth profiling displayed some extent of lithium enrichment at the surface of the deposited material. This is believed to have occurred due to the high diffusivity of lithium within aluminium during solidification.

Conclusions from Chapter 5:

4) The low heat-input induced within the base metal during LRM with laser pulse energies ranging from 0.5 – 0.25 J per pulse resulted in the formation of a fine cellular solidification structure, with cell widths ranging from 350 – 250 nm. The lowest pulse energy employed (0.125J per pulse) resulted in a low heat-input of ~1.5J/mm and produced a featureless solidified morphology.

5) The KGT model estimated the SFV realized during solidification was between 3 cm/s and 1m/s.

6) The CGM for solute trapping predicted a deviation from equilibrium partitioning during solidification for all pulse energy levels employed due to the high SFV values. This non-equilibrium partitioning was then measured through the application of XPS depth profiling, where it was revealed that an increase in pulse energy resulted in an increase in surface enrichment of solute (lithium). The lowest pulse energy investigated in this study (0.125J) revealed minimal surface enrichment of lithium after solidification, therefore implying significant solute trapping occurring.

7) Lattice parameter measurements of the RSP material revealed that the samples re-melted with a pulse energy of 0.125J displayed a reduction in lattice parameter to 4.0399 Å, with respect to the starting material (4.0485 Å) as well as that of pure aluminum. This supports the hypothesis of solute trapping occurring during solidification, as both lithium and copper have been shown to reduce the lattice parameter of aluminum when trapped in SSSS.

Conclusions from Chapter 6:

8) Microstructural analysis of the ESD solidified material displayed the transformation of a planar morphology to that of very fine copper rich cells, ranging from 30-60nm in width.

9) The KGT model predicted an interface stability threshold SFV of ~1m/s, above which the interface will remain planar, and below which a cellular morphology will form. This transitional SFV therefore supports the argument of solute

trapping occurring, as the CGM model predicts significant deviations from equilibrium partitioning for both lithium and copper at velocities on the order of 1m/s. Furthermore, the KGT model accurately predicts the cellular morphology subsequent to interfacial breakdown. The model predicted a cellular radius of approximately ~20nm (or ~40nm wide cells), which is in direct correlation with the microstructural analysis of the rapidly solidified material.

10) TOF-SIMS mapping techniques revealed a homogeneous distribution of lithium within the RSP material, while TOF-SIMS depth profiling revealed some surface segregation of copper. Therefore supporting the hypothesis that the ESD process is capable of producing a SFV in excess of 1m/s and therefore able to induce solute-trapping behavior during solidification.

11) APT analysis revealed that lithium was not present within the cell walls, however globular Al_3Li was found to be present upon the copper rich cell walls. A time dependent nucleation theory predicted that the metastable Al_3Li phase was not formed during solidification, but instead precipitated out of solid solution during a natural aging process.

<u>Conclusions from Chapter 7:</u>

12) It was determined that the CSC-MIG deposited material displayed a low hardness in the T1 condition and the T5 condition. This was determined to be due to the loss of lithium due to burn-out within the arc during deposition, as well as the result of the formation of a large volume fraction of a ternary eutectic phase.

13) The ESD deposited material displayed a small amount of lithium burn-out, and therefore the T1 hardness suffered slightly. The T5 hardness of the ESD material however obtained a hardness of ~99HV, which is significantly less than the

~150HV of the T8' BM. It was determined that this was due tot the lack of a cold-working process prior to aging.

14) The T1 hardness of the LRM material is similar to the T3 BM. It is therefore concluded that the LRM process is capable of producing SFF components of AA2199, which can achieve adequate hardness via a natural aging process, without requiring cold-working. Finally the LRM solidified material in the T5 condition was determined to be capable of aging to 81% of the hardness (~122HV) of the BM in the T8' condition, without the application of a cold working process.

Global Conclusions:

15) The effect of the solute-trapping phenomenon on the solute distribution within a rapidly solidified Al-Cu-Li alloy was measured for the first time.

16) The relationship between the size of a cellular microstructure and the solidification front velocity, as predicted by the KGT model was validated for an Al-Li-Cu alloy.

17) The age-hardening response of rapidly solidified Al-Cu-Li alloy was reported, and it was determined that laser re-melting is capable of inducing a significant natural aging response within the deposited material.

10 Contributions to original knowledge

1) The effect of laser pulse energy on the solidification morphology and solute distribution was reported, and the conditions required to perform featureless solidification in which minimal microsegregation occurs during solidification were determined.

2) The solidification behavior of the Electrospark deposition process was studied and the solidification front velocity was estimated to be on the order of 1m/s, correcting the erroneous values previously reported in literature based on constitutional super-cooling theory.

3) The role of lithium within the cellular microstructure was determined for the first time via the application of atom probe tomography.

4) It was determined that laser re-melting is a feasible method of performing solid freeform fabrication of Al-Li-Cu components. It was determined that no lithium burn-out was measured during deposition and the high solidification front velocity is capable of minimizing the extent of solute segregation occurring solidification, resulting in a chemically homogeneous component, displaying significant hardening response.

11 Appendix – List of variables used within models

Adams and Rosenthal's Heat-Flow Equations

Variable	Value	Units
Temperature (T)	Calculated	K
Initial Temperature (T_0)	298	K
Workpiece Thermal Conductivity (k)	229	W/(m*K)
Workpiece thickness (g)	Varies	m
Heat-Input (Q)	Calculated	No units
Travel Speed (V)	Varies	m/s
Radial Position (R)	Calculated	m
Position Along Weld Direction (x)	Varies	m
Workpiece Thermal Diffusivity (α)	9.3205E-5	m^2/s

Continuous Growth Model Variables

Variable	Value	Units
Solidification Front Velocity (v)	Ranged from 0.01 to 1000	m/s
Diffusive Speed of Cu in Al (v_D)	6.7	m/s
Diffusive Speed of Li in Al (v_D)	24.6	m/s
Equil. Partition Coeff of Cu in Al	0.15	No units
Equil. Partition Coeff of Li in Al	0.55	No units

Kurz-Giovanol-Trivedi Model Variables

Variable	Value	Units
Gibbs Thompson Coefficient (Γ)	1.53×10^{-7}	K*m
Péclet Number (P)	Calculated	No Units
Liquid Inter-Diffusion Coeff. (D)	2.0×10^{-9}	m^2/s
Slope of liquidus (m)	-3.4015	K/wt%
Solute Concentration (C_0)	Calculated	No units
Partition Coeff of Cu in Al (k_{eq})	0.15	No units
Partition Coeff of Li in Al (k_{eq})	0.55	No units
Mean Temperature Gradient (G)	Calculated	K/m
Concentration Gradient (G_c)	Calculated	%/m

Clyne-Kurz Model

Variable	Value	Units
Partition Coeff of Cu in Al (k_{eq})	0.15	No units
Partition Coeff of Li in Al (k_{eq})	0.55	No units

Fraction Solid (f_s)	Varies	No units
Diffusivity of Cu in Al (D_s)	$2.0\text{x}10^{-9}$	m^2/s
Diffusivity of Li in Al (D_s)	$2.5\text{x}10^{-9}$	cm^2/s
Solidification Time (t_f)	Calculated	s
Dendrite Arm Spacing	Measured	m

Time Dependent Nucleation Theory Model Variables

Variable	Value	Units
Ideal Gas Constant (R)	8.314	J/(K*mol)
Wetting Angle (θ)	40	deg
Atomic Jump Distance (a)	$5\text{x}10^{-10}$	m
Molar Weight of Al (W_m)	Calculated	g
Molar Weight of Al_3Li (W_m)	Calculated	g
Avagadro's Number (N_0)	6.022E23	No units
Density of Al (ρ)	2.7	g/cm^3
Density of Al_3Li (ρ)	Calculated	g/cm^3
Alloy Concentration ($x_{L,eff}$)	Varies	%/m
Liquidus Temperature (T_L)	Calculated (FactSage)	K
Ideal Glass Transition Temp (T_g)	973	K
Boltzman Constant (k)	1.38065E-23	$m^2kg\ s^{-2}K^{-1}$
Temperature (T)	Varied	K